10-4-2018 10:00 AM

High Resolution Ion Beam Investigations of the Mechanisms of Titanium Anodization

Mitchell A. Brocklebank
The University of Western Ontario

Supervisor
Dr. Lyudmila Goncharova
The University of Western Ontario

Graduate Program in Physics
A thesis submitted in partial fulfillment of the requirements for the degree in Doctor of Philosophy

Recommended Citation

Brocklebank, Mitchell A., "High Resolution Ion Beam Investigations of the Mechanisms of Titanium Anodization" (2018). *Electronic Thesis and Dissertation Repository*. 5768.
https://ir.lib.uwo.ca/etd/5768

Abstract

The unique behaviour of thin films and their surfaces and interfaces, significantly impact material and device properties. Probing these structures with ion beams (IB) provides quantitative composition and thicknesses measurements. In this dissertation, the IB techniques of medium energy ion scattering (MEIS), nuclear reaction profiling (NRP) and Rutherford backscattering spectrometry (RBS) are used to analyze energy losses in ultra-thin films, as well as elucidate the mechanisms of anodic film growth.

Accurate stopping cross sections of protons, ε, in the medium energy range (50-170 keV) often show deviations from Bragg's rule. Here, ε_{Ti}, ε_{Si}, and ε_{TiO2}, were derived from MEIS spectra. Thickness and composition of Ti, Si, and TiO_2 films were determined using RBS, MEIS, and X-ray photoelectron spectroscopy. ε_{TiO2} are systematically lower (≈14%) and the stopping maximum occurs at higher energies, compared to SRIM2013. Our experimental ε_{Ti} and ε_{TiO2} values allowed estimates of $\varepsilon_{O,}$ which better predict the stopping maximum of previously reported ε_{SrTiO3}. This suggests that the effect of different electronic enviroment on the SCSs of O should not be neglected when applied to metal oxides.

Depth-profiling with MEIS and NRP, and $^{16}O/^{18}O$ isotopic labeling, can elucidate anodization growth models. Thin Ti films on Si(001) were exposed to $H_2{}^{18}O$, and anodized in $D_2{}^{16}O$ potentostatically. Anodization at 0 - 10 V results in a bi-layer structure: $Ti^{16}O_2/Ti^{18}O_2/Ti$. The $Ti^{16}O_2$ region is on the oxide surface and the $Ti^{18}O_2$ region at the oxide/metal interface (composed of the original ^{18}O atoms). The O depth profiles are consistent with the point defect model (PDM), in which anodic oxide growth is due to ionic transport via the continual generation and annihilation of point defects in the oxide.

A new *in situ* electrochemical cell was designed, constructed, and used to collect RBS data under potentiostatic control. Features of Ti anodization were observed by *in situ* RBS, for Ti thin films sputter-deposited onto 100 nm thick SiN windows. The evolution of the elemental depth profiles for Ti and O spectra were consistent with the PDM, while Cl incorporation, likely happens during the formation of oxide monolayers from Ti^{4+} precipitation. Compositional differences between *in situ* and *ex situ* measurements are emphasized.

Keywords

Medium energy ion scattering, nuclear reaction profiling, stopping cross section, protons, Bragg's rule, anodization, titanium, titanium dioxide, isotopic labelling, *in situ*, *ex situ*, electrochemical cell, Rutherford backscattering, point defect model, high field model.

Co-Authorship Statement

The content of the investigation presented in Chapter 3 is partially based on experimental data of the stopping cross sections for elemental Ti and Si in the relevant energy range that had been collected by Dr. Sergey Dedyulin when he was a Ph.D. student at Western University, under the supervision of Dr. Lyudmila Goncharova. Mitchell Brocklebank was able to reproduce the procedure used and acquire additional data related to the stopping cross sections that were still outstanding. He is also responsible for the creation of the TiO_2 samples by molecular beam epitaxy (MBE), and data analysis, and writing of the manuscript. Dr. Sergey Dedyulin and Dr. Lyudmila Goncharova were instrumental in providing feedback on the manuscript and are co-authors.

For the content of Chapter 4, Mitchell Brocklebank was the primary author responsible for a majority of the experimental work, data analysis, and manuscript writing. The samples were produced by sputtering at AECL, and Dr. James Noel preformed electrochemical anodization in $D_2{}^{16}O$. Mark Biesinger (Surface Science Western) performed X-ray photoemission spectroscopy. Dr. Lyudmila Goncharova again was vital in bringing her expertise in ion beam analysis related to experimental work and manuscript writing. Dr. Noel and Dr. Goncharova are both are co-authors of the manuscript.

For the content of Chapter 5 Mitchell Brocklebank designed the electrochemical cell, and preformed the experiments, data analysis, and wrote the manuscript. Dr. Tim Goldhawk at the Western Nanofabrication Facility preformed depositions of Ti onto the SiN windows. Dr. James Noel and Dr. Lyudmila Goncharova aiding in experimental design and feedback to the manuscript.

Acknowledgements

Foremost among those I would like to thank is my supervisor Dr. Lyudmila Goncharova, without whom I would not know a single facet of ion beam analysis. It is in virtue of her patience and faith in my abilities that I have progressed as a scientist at all and this document should be a testament to that.

I would like to thank Jack Hendriks for his mastery of all things related to the Tandetron Accelerator Facility. A vast majority of the data presented in this work was predicated on a well-functioning accelerator, which he ensured was the case and as a direct consequence of his operation and upkeep of the equipment, that I was able to acquire any data. Additionally, I want to thank him for his help in integrating the *in situ* cell electronics into the current vacuum system.

I would like to thank Brian Dalrymple from the Western Physics and Astronomy Machine Shop for his construction of the electrochemical cell and the constant last minute modifications that were required in the course of these investigations.

I would like to thank Ontario Graduate Scholarship (OGS) program for the funding they provided for the last two years off my time at Western.

Lastly, I would like to thank my beloved friends and family who make life worth living. Especially my father who always fostered my curiosity while growing up and who’s finical support has been invaluable and also my exceedingly patient and loving girlfriend Victoria Richards.

Table of Contents

List of Figures

List of Tables

List of Abbreviations

AES	Auger electron spectroscopy
AD	areal density
amu	atomic mass unit
AZ	Andersen-Ziegler
CE	counter electrode
DLC	diamond-like carbon
FTIR	Fourier transform infrared spectroscopy
HFM	high-field model
IBA	ion beam analysis
MCA	multi-channel analyzer
MEIS	medium energy ion scattering
MBE	molecular beam epitaxy
NACE	National association of corrosion engineers
NIST	National Institute of Standards and Technology
NR	neutron reflectometry
NRA	nuclear reaction analysis
NRP	nuclear reaction profiling
PE	polyethylene
PBR	Pilling-Bedworth ratio
PDM	point defect model
PIXE	particle induced X-ray emission

PSTAR	proton stopping tables and ranges
PTFE	polytetrafluoroethylene
RE	reference electrode
RBS	Rutherford backscattering spectrometry
SCS	stopping cross section
SHE	standard hydrogen electrode
SIMS	secondary ion mass-spectrometry
SIMNRA	SIMulation for Nuclear Reaction Analysis
SRIM	the Stopping Range of Ions in Matter
STM	scanning tunneling microscope
STO	strontium titanate ($SrTiO_3$)
TEA	toroidal electrostatic analyser
UHV	ultra-high vacuum
WE	working electrode
XRD	X-ray diffraction
XPS	X-ray photoelectron spectroscopy

Chapter 1: Introduction

Metal corrosion is a ubiquitous phenomenon and its direct consequences entail a severe global economic impact. The association of corrosion engineers, NACE International, estimates the annual global cost of corrosion to be US $2.5 trillion, impacting nearly every sector, especially the oil, gas, and water industries [1], and their associated pipeline infrastructure. The economic impact of corrosion is so large because so much of modern technology is based on the use of reactive metals that exhibit high affinity for oxygen [2]. Metals such as Ti are of special interest since they spontaneously form oxides when exposed to oxygen rich environments, that are thermodynamically stable and highly insoluble, and hence provide excellent corrosion resistance in most corrosive media [3].

Given how wide reaching the impact of corrosion is, it is imperative to develop the best possible corrosion-resistant films, formed on metals, to mitigate or completely ward off its effects. Anodization is the simplest and most efficient method of forming porous and thick oxide films, that function as corrosion resistant coatings, on certain metals (Al, Ta, Ti, Nb, Zr, Hf, and W), and their alloys [4]. As such, a growth model that accurately describes the fundamental mechanisms of anodization, specifically at the level of individual atomic and molecular species, and their transport mechanisms (diffusion, migration, etc.), is a necessary precondition if one is to exert full control over the anodization process and completely determine the properties of the resultant anodic films.

Anodization is the electrochemical growth of a solid oxide film on a metal substrate, achieved by the biasing the metal anodically in an electrochemical cell and is represented schematically for Ti in Figure 1.1. Given the direction of the bias, electrons from the anode metal, flow to the cathode, through the external circuit, which results in ionization of metal atoms at the anode surface [4]. The oxidation occurs when these metal cations react with O-containing anions in the liquid electrolyte and this results in the formation of a solid oxide film on the anode metal. Likewise, the electrons being forced from the external circuit to the cathode result in a reduction reaction given in Figure 1.1. The most elementary description of Ti oxidation during anodization can be expressed as:

$$Ti^{4+} + 2O^{2-} \rightarrow TiO_2 \tag{1.1}$$

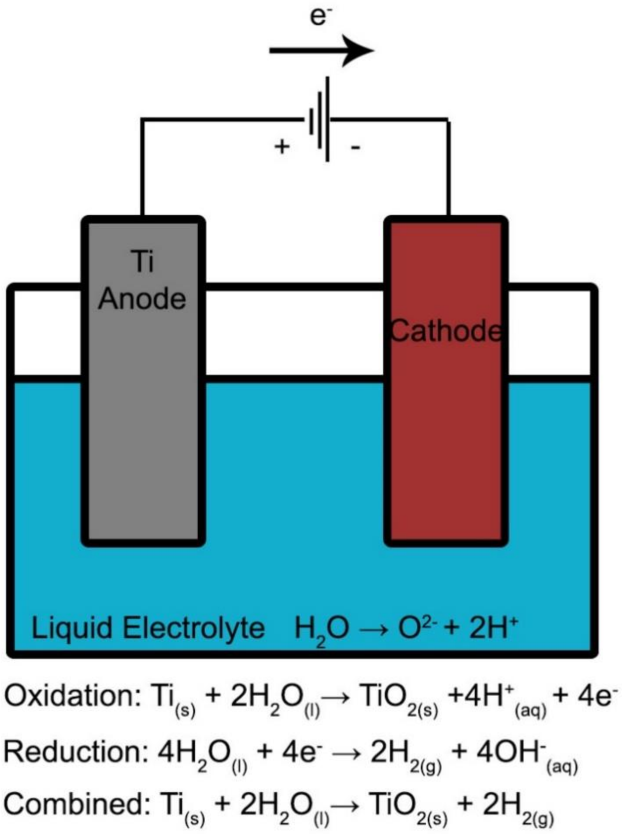

Figure 1.1: A schematic representation of the anodization of Ti metal in an electrochemical cell. The oxidation and reduction reactions for the anode and cathode are given. The source of the O anions is the liquid electrolyte (mostly H_2O).

Once the initial oxide monolayer has formed, further growth necessitates that metal cations which are present at the metal/oxide interface, react with O anions, which are present at the oxide/electrolyte interface. Ultimately the growth of the oxide is dependent on ionic transport (Ti^{4+} and/or O^{2-}) though the pre-existing oxide film, driven by the presence of large electric fields, on the order of 10^7 to 10^9 V/m [4], where they react with the opposite species according to Equation 1.1 to form new oxide.

Even today, there still remains some uncertainty as to which mathematical models best fundamentally describes anodization. There is however, a wide consensus that the rate of anodization is limited by the mass-transport of ionic species through the pre-existing oxide film [4]. Consequently two competing models have been developed that purport to describe anodic oxide growth based on such ionic mass-transport: the high-field model (HFM) and the point defect model (PDM) [4].

It is the objective of the present work to provide insight into the anodization processes of Ti metal by utilizing ion-beam based, high-resolution depth profiling techniques, which can quantify the composition of the anodic oxide films that form on Ti electrodes. In conjunction with an appropriate isotopic labeling procedure, such *ex situ* measurements can provide insight into the mass-transport of ionic species through Ti electrodes, and ultimately allow us deduce which model (HFM vs PDM) best describes Ti anodization.

In the current chapter, details of the PDM (Chapter 1.1.1) and HFM (Chapter 1.1.2) will be presented. This discussion culminates in a description of an isotopic labeling procedure, utilizing ^{16}O and ^{18}O (Chapter 1.1.3), according to which, each theory (HFM vs. PDM) predicts unique O depth profiles through the anodic oxide Ti films. By using depth profiling methods, medium energy ion scattering (MEIS) and nuclear reaction profiling (NRP), in combination with isotopic labeling, we are able to measure O profiles and compare the experimental O depth profiles with the predictions of the HFM and PDM. Experimental details associated with ion beam analysis (IBA) and supplemental techniques are presented in detail in Chapter 2.

The principle high-resolution techniques used to depth profile these films involve the interactions of ion beams of protons (H^+) in the medium energy range (50 – 200 keV). This medium-energy range is where the energy loss of H^+, as they penetrate through a target medium, is maximized, and presents a unique set of interpretive challenges. An introduction to the field of energy losses for H^+ in this energy range will be outlined in Chapter 1.2 and forms the basis of the investigation to determine accurate energy loss values of H^+ in Si, Ti and TiO_2 (the topic of Chapter 3). Having good estimates of the energy loss is necessary for converting measured ion energy loss into a corresponding depth scale (i.e. grants depth sensitivity).

Chapter 4 presents, the isotopic labelling procedure employed during Ti anodization, and the MEIS and NRP depth profiling data (which rely on good estimates of the energy loss of H^+ in Ti and TiO_2). From the O depth profiles, deductions about whether the PDM or the HFM better predict the experimental results are made.

However, transfer of anodic oxides from ambient conditions to the ultra-high vacuum (UHV), required by the ion-beam techniques, can result in compositional changes to the films and complicate experimental interpretations. To circumvent this, Chapter 5 describes the design and use of an electrochemical cell that contains a liquid electrolyte and allows *in situ* Rutherford backscattering spectrometry (RBS) to be performed during potentiostatic polarization and observe real time changes in the Ti electrodes as reflected in a series of RBS acquisitions.

1.1 Theories of anodization

1.1.1 The point defect model (PDM)

The Point Defect Model (PDM) has been in development for over 35 years [5] and describes the atomic scale growth and breakdown of passive films that form on reactive metals in contact with corrosive environments [6]. The first generation model (PDM-I) was developed in the late 1970's under the assumption that an initial passive oxide film, called the "barrier-layer" (i.e. a pre-existing oxide, sulfide, or hydride), is highly point defective, e.g. with a high concentration of cation and anion vacancies. The basis of film growth in the PDM is that under an applied electric field, there is a continual generation and consumption of cationic and anionic point defects. As depicted in Figure 1.2, anion vacancies are continuously generated at the metal/barrier layer and consumed at the barrier layer/electrolyte interfaces, and the cation vacancies are generated and consumed at the opposite interfaces, relative to the anions [7].

In Figure 1.2, at the metal/barrier layer interface, an O atom in then oxide's oxygen sublattice will react with the metal atom (in the metal substrate) to form oxide via. Equation 1.1, and simultaneously generate an O vacancy in the oxygen sublattice of the oxide. These vacancies are represented by dashed lines in Figure 1.2. This vacancy will be filled by an O atom directly adjacent to it, which again creates another vacancy even deeper into the oxide. This process continues until the vacancy is transported to the oxide/electrolyte interface where it is consumed, when an O anion from the electrolyte fills it.

Likewise, when a cation from the metal sublattice of the oxide, at the barrier layer/electrolyte interface, is ejected into the electrolyte, it reacts with O anions in the solution to form an oxide region called the "precipitated outer layer", and simultaneously creates a metal vacancy in the oxide. The cation vacancy flux proceeds in the direction opposite to the anions vacancy flux, driven by the repeated filling of the metal vacancy with metal atoms adjacent to it, until it reaches the metal/barrier layer interface where it is finally consumed by a metal atom from the metal substrate. The ionic current through the film is a consequence of a sum of these two vacancy fluxes and the oxide film grows at the metal/barrier layer and outer-layer/electrolyte interfaces simultaneously.

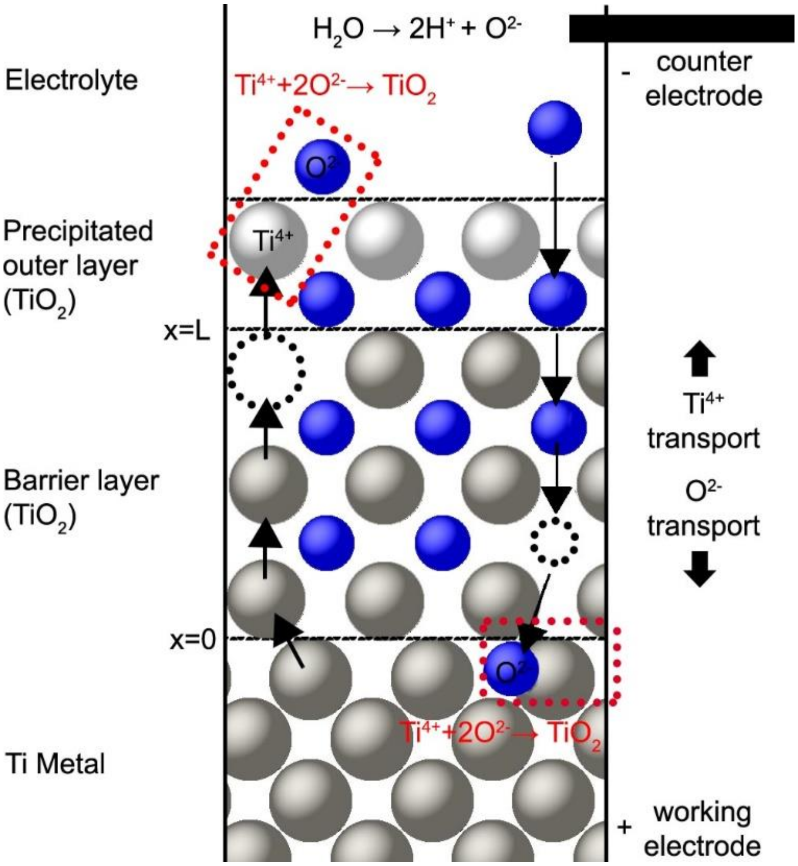

Figure 1.2: A schematic representation of the PDM. The grey spheres represent Ti atoms and the blue spheres represent O atoms, while the dashed spheres represent the respective vacancy in the oxide. The series of arrows depicts the successive movement of the ionic species, which results from repeated fillings of the vacancy and its subsequent consumption at the appropriate interface.

The barrier layer grows into the metal while the outer layer forms by precipitation of the Ti cations.

There were experimental observations that the PDM-I did not predict [5]: the existence of steady states and their passive current density, the resultant steady state film thickness as a linear function of anodization voltage after a fixed time, and it did not predict the growth kinetics such as inverse logarithmic growth laws that where seen in the literature [6]. The PDM-II was introduced to overcome these shortfalls. In addition to oxygen and metal vacancies, PDM-II also incorporated metal interstitials and included a reaction describing the dissolution of the barrier layer at the oxide/electrolyte interface, which resulted in predictions of steady-states film thickness and current density [6].

Important to the current work is that the PDM-II predicted the existence of a so called “bi-layer structure”, where the oxide that resulted from anodization was separated into two distinct regions: i) the barrier layer that grows directly into the metal which occurs without the involvement of species in the solution, and ii) the outer layer that forms by cation hydrolysis.

According to MacDonald, the “PDM-II has proved to be highly successful … and the authors know of no case where the model has been at odds with experiment” [5]. PDM-III is currently in development and was offered as an extension of PDM-II to instances where the outer layer of the bi-layer structure is so resistive that it determines interfacial impedance and thus controls the passive current density and the corrosion rate [6].

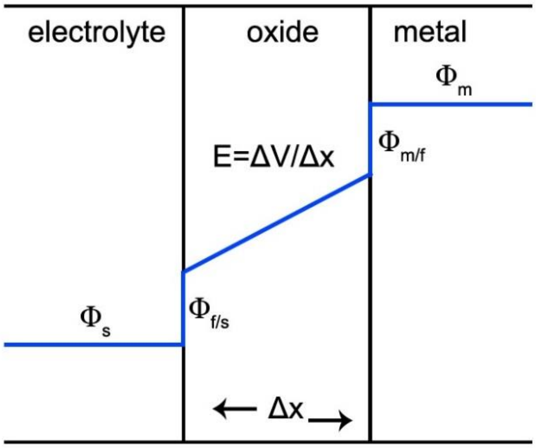

Figure 1.3: A schematic showing the drop in potential across the metal/oxide, $\Phi_{m/f}$, oxide/electrolyte, $\Phi_{f/s}$, interfaces. The potential across the solution is Φs and across the metal Φ_m. The electric field through the film is constant with respect to the spatial dimension *x*.

Figure 1.3 depicts a fundamental assumption of the PDM, that the magnitude of the electric field, *E*, is constant throughout the oxide and independent of applied voltage. The voltage independence is due to buffering by Esaki tunneling which is tunneling between electronic bands and inter-band states [2, 8, 9]. As the magnitude of the electric field through the film increases, the tunneling distance for electrons from the valance to conduction bands decreases which results in a greater amount of tunneling. According to MacDonald, this produces a “separation of charge that opposes the field essentially buffers the field at an upper, voltage independent value” [7]. The upper limit of the field strength is $E < 5$ MV/cm [5]. The PDM can be classified as a low-field approach given that the effective field through the film is low enough so that the Nerst-Einstein and generalized Fick’s law describe the current density in terms of vacancy transport [4]:

$$i = -zD\frac{dC}{dx} - zF\mu C\frac{d\Phi}{dx} \tag{1.2}$$

where *F* is Faraday's constant, *D* is the electrochemical diffusivity of the defect, μ is the electrochemical mobility, *Z* is the charge of the defect, and *C* is the defect concentration. The term on the left of Equation 1.2 describes diffusion due to a concentration gradient and the term on the right represents low-field migration.

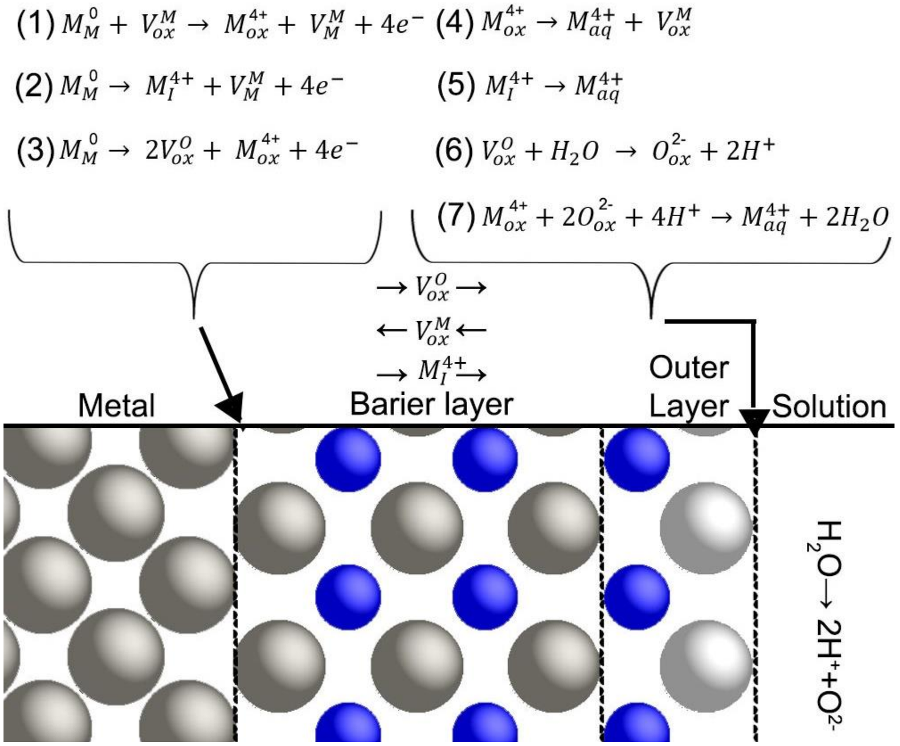

Figure 1.4: A summary of the relevant reactions (1) – (7), occurring at the respective interfaces, as postulated by the PDM, assuming an oxide stoichiometry of MO_2 and the assumption that no change of oxidation state is experienced when cations are ejected into solution. M_M^0 is a metal atom in the metal substrate, V_{ox}^O is an oxygen vacancy in the oxygen sublattice of the oxide, V_{ox}^M is a metal vacancy in metal sublattice, M_{ox}^{4+} is a metal ion in oxide's metal sublattice, O_{ox}^{2-} oxygen ion in oxide's oxygen sublattice, V_M^M is a vacancy in the metal substrate, M_I^{4+} is cation interstitial, and M_{aq}^{4+} is a cation in the solution. Adapted from [10]

As shown in Figure 1.4, there are seven reactions that underlie the PDM-II and describe the defect generation and consumption that bring about the growth of the oxide film [5]. Reaction (1) represents the consumption of cation vacancies and reaction (4) represents their generation. Together they describe the transport of cation vacancies across the barrier layer. Likewise, reactions (2) and (5) represent the generation and consumption of metal interstitials and together the transport of metal interstitials across the barrier layer. Reaction (6) represent the consumption of oxygen vacancies which have been produced by reaction (3) at the metal/barrier layer interface by oxygen injection from electrolyte.

All reactions in Figure 1.4 are either lattice conservative or non-conservative. Lattice-conservative reactions will maintain the position of the interfaces (from a laboratory references frame) and the non-conservative reactions will result in movement of the boundaries. Reactions (1), (2), (4), (5) and (6) are lattice conservative processes because they do not result in dimensional change to the film. Reactions (3) that describes film formation and (7) that describes film destruction, are not lattice conservative.

Reactions (1) and (4) (or (2) and (5)) can be combined to give an equation for metal dissolution that does not factor the barrier layer:

$$M_M \rightarrow M_{aq}^{4+} + V_M^M + 4e^- \tag{1.3}$$

Combining (3) and (6) eliminates the oxygen vacancies, and gives an equation for the growth of the barrier layer:

$$M_M + 2H_2O \rightarrow \left(2O_{ox}{}^{2-} + M_{ox}{}^{4+}\right) + 4H^+ + 4e^- \tag{1.4}$$

According to Equation 1.3 and Equation 1.4, the generation of oxygen vacancies via reaction (3) at the metal/barrier layer and their consumption by reaction (6) at the barrier layer/electrolyte interface, is solely responsible for the growth of the barrier layer into the metal. Thus, the prediction is that any species in the metal (e.g. impurities) will be present in the barrier layer but importantly, will not contain any species from the electrolyte (except for O). This is contrasted with the precipitated outer layer that forms by hydrolysis of cations transported through the barrier layer with their reaction with anions in the electrolyte (H_2O, HS^-, etc.) and tends to commonly form a oxide, oxyhydride, or hydroxide or some kind of mixture of the species [7]. This is what is meant by the anodic oxides exhibiting a bi-layer structure.

The thickness of the barrier layer might be a small fraction of the thickness of the oxide film. According to Macdonald most studies reported to date [6] fail to take this distinction into account. For example if sputtering was used in conjunction with XPS, the relatively thin barrier layer might be sputtered away in a very short time if a realistic sputter rate is used, making the possibly distinct composition of the barrier layer go unnoticed and interpreting the multi-layered structures as a single layer. Non-destructive techniques capable of quantitative high resolution depth profiling of these anodic films that are capable of overcoming this pitfall will be presented in Chapter 2.

1.1.2 The High Field Model (HFM)

The high field model (HFM) describes the oxide formation kinetics as dependent on the migration of ions mediated by a very strong electric field, 10^7 V cm^{-1} (10 V nm^{-1}), through the oxide film [11]. Günthershultze and Betz in 1934 described the kinetics of oxide growth in terms of ionic current density being an exponential function of the electric field within the film [12]. Verwey expanded upon this in 1938, and included the concept of jump distances between lattice sites and the required activation energy for movement between these sites [13]. Cabrera and Mott further elaborated on the formalism by the inclusion of the frequency of atomic vibrations [14]. A more detailed derivation of the ionic current density (Equation 1.5), is presented in Appendix A1 and should be consulted if mathematical elaboration of the following ideas is desired.

According to the HFM, the movement of ions occurs via a thermally activated, field-supported, hopping mechanism between two consecutive planes of atoms, located at x and $x+a$, that contain an areal density of charge carriers, n_x and n_{x+a} respectively (before the hop). Although our material might not necessarily be crystalline, according to Vanhumbeek and Proost, the “conclusions remain valid in the case of amorphous films as well” [4]. Charges carriers can “jump” from one plane to another provided they overcome an activation barrier of energy W. In Figure 1.5a, the potential energy of the activation barrier (W) between two planes of atoms is shown to be symmetric before the field is applied which implies the flux of charge carriers between plans is equal. After the electric field, E, is applied, the activation barrier is asymmetric between W_{left} and W_{right}. F is the Faraday constant (9.65×10^4 C mol^{-1}), Z is the change of the charge carrier, a is the length of the jump between adjacent positions, and α is a coefficient that describes the symmetry of the activation barrier.

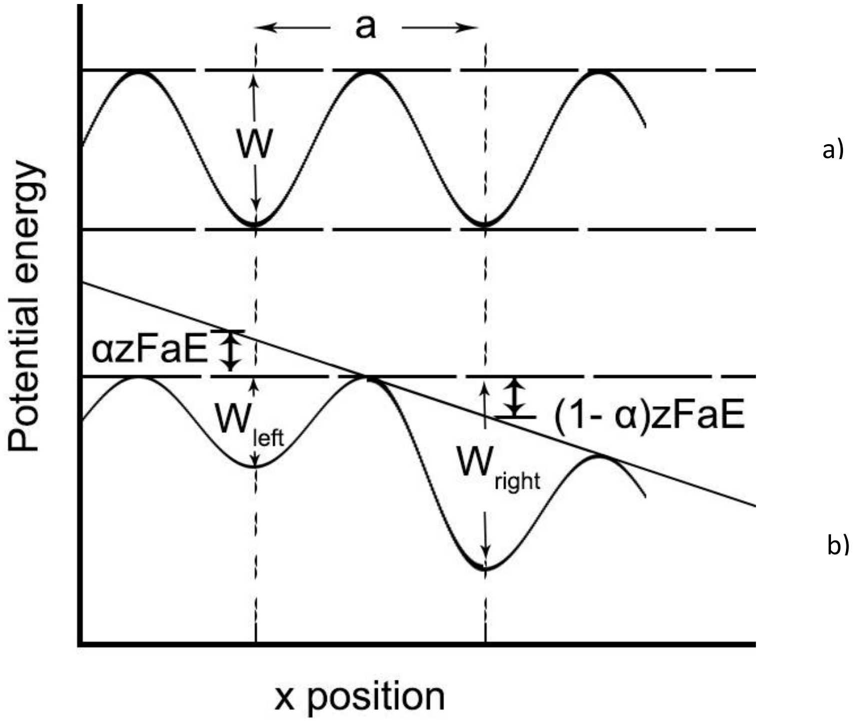

Figure 1.5: A schematic of the potential energy barrier that underlies the HFM. The potential energy, *W*, that must be overcome in the first instance before the application of the electric field. After the E field is applied in b), the flux of charge carriers in the direction of the electric field will be far greater than in the other direction. α is a coefficient that describes the symmetry of the activation battier after a voltage is applied.

If an electric field is applied, the activation barrier is lower for the jump in the direction of the field and simultaneously increased in the opposite direction and this asymmetry is depicted in Figure 1.5b. The strength of the electric field is assumed to render diffusion negligible in comparison to migration, so $dc/dx \approx 0$. The migration in the direction opposite to the field is assumed to be negligible given the differences between activation barriers in each direction.

Ultimately, according to the HFM, the ionic current density associated with the migration of a given ionic spices has an exponential dependence on the electric field though the film:

$$i = i_0 e^{\beta E} \tag{1.5}$$

where the field factor β, and primary ionic current i_0, are constants for a given set of experimental conditions. Appendix A1 should be consulted to gain a better understanding of their physical meaning.

The derivation of Equation 1.5 makes no *a priori* assumptions about the position of the activation barrier, nor the specific type of charge carrier involved, and only gives a relationship between current density and applied electric field. Hence it provides no insight as to where the rate-limiting step is located. Verwey [13] suggested it was the field driven migration of charge carriers through the bulk of the film via migration. Mott and Cabrera [14] suggest it is the injection of cations into the oxide, across an activation barrier at the metal/oxide interface. In terms of charge carriers, Günthershultze and Betz [12] used cations and anions in their description, Mott and Cabrera and Verwey [11] described only the contribution of metal cation interstitial, while Fehlner and Mott [4] postulated anion migration only.

It is well established that for most so called valve metals (Ta, Al, Nb, Ti, etc.), both cations and anions contribute to oxide growth [4]. When both cationic and anionic species are considered the total ionic current density is thus:

$$i = i_{0,a} e^{\beta_a E} + i_{0,c} e^{\beta_c E} \tag{1.6}$$

Figure 1.6 gives a depiction of the HFM at the molecular level. Oppositely charged ions experience field–driven migration from their respective interface, down the potential gradient, through the existing oxide, and react with their respective counter ions at the opposite interface to form new oxide according to Equation 1.1. According to the HFM, there is no interaction between the existing oxide and the mobile ionic species. Note, there is oxide growth at both interfaces, as in the PDM as well.

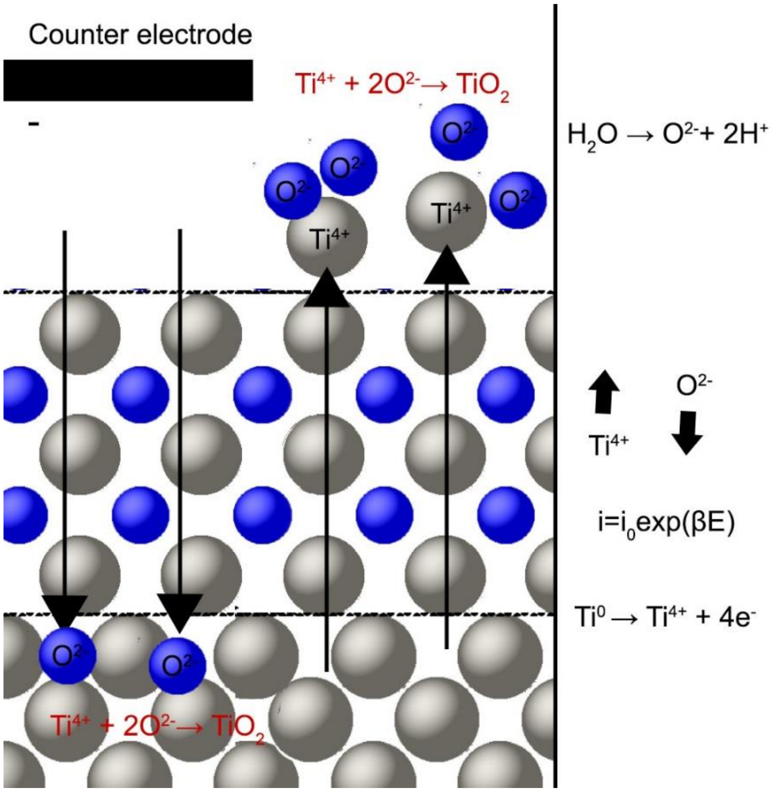

Figure 1.6: A schematic representation of the HFM's description of ion transport. The largest potential drop between anode and cathode occurs within the existing oxide and this drives cation and anion transport and thus oxide growth.

1.1.3 Comparisons between anodic oxide growth models

Most of the available literature regarding the anodization of Ti is in the domain of electrochemistry, where electrical measurements are taken and inferences about the electrode structure are made, but rarely is the electrode's composition quantified directly in terms of the elemental depth distributions. Even rarer still are the electrodes composition discussed in terms of the predictions of the PDM vs the HFM. Sometimes techniques like Auger electron spectroscopy (AES), secondary ion mass spectrometry (SIMS), and XPS are used to characterize the anodic films but often it has not been appreciated that each theory predicts different oxide phases. For example in the PDM, the precipitated outer layer might be $10^2 – 10^3$ times larger than the barrier layer [7]. A couple of studies that quantify the Ti electrode structure will be discussed, one of which directly makes comparisons to the growth model predictions.

Khalil and Leach used Rn^{222} atoms as Kirkendall markers to elucidate the mobilities of the ions involved [15]. They put a small concentration of radioactive Rn^{222} just below the surface of the Ti metal to act as a marker layer. They then measured the energy spectrum off the α emitted at 5.486 MeV. Then they anodized the Ti samples and re-measured the energy of the emitted α as it now passed through some thickness of newly grown oxide, causing the α to lose energy inelastically as it exists the film. With known estimates of the energy loss of α in $TiO_{2,}$ they could measure the oxide thickness now present in front of the markers. There are three theoretical possibilities when it comes to oxide growth according to both the PDM and HFM: i) only cations are mobile, ii) only anions are mobile, iii) both ionic species are mobile (with possibly different mobilities). If only cations are mobile, the markers once at the metal/oxide interface would be buried under the full thickness of the oxide film. If only anions are mobile, the markers would be in the same position, as oxide growth would proceed from the metal surface inwards. If both had mobility there would be an oxide growth in both positions, whose thickness corresponds to the relative ion mobility. Khalil and Leach concluded that the markers were buried under 35% of the total oxide grown, which corresponds to the amount that was formed due to Ti mobility, while and 65% of the oxide grew below the markers which implied it was due to O mobility. Both the PDM and HFM can be seen to be consistent with this result, as both predict oxide growth at both of these interfaces due to the relative flux of ionic species.

Tun et al. studied the effect of Ti anodization in aqueous NaCl, with a pre-existing air-grown oxide using *in-situ* neutron reflectometry (NR) [16]. After anodization, the resultant oxide could be divided into two distinct regions; an inner region with the same thickness and composition of the original air-grown oxide and an outer one containing significant amount of H, which probably exists since the solution contains OH^- ions which are incorporated into the oxide. This bi-layer structure lead the authors to suggest that the underlying growth mechanism that they preferred was the PDM. However, the authors suggest that it could be possible that while OH^- is being attracted to the cathode, it could be striped of the H^+ by the large potentials in film (according to the HFM), while the oxygen passes through the oxide and reacts with Ti. They suggest that, this could result in the inner oxide region that is free of H and an outer oxide region containing H. They note this is very unlikely since the thickness of the H-free region being exactly the same as the air-grown oxide would have occurred simply by chance in the context of the HFM, while it is necessary in the context of the PDM.

In this thesis, we developed an isotopic labelling procedure to overcome the ambiguities of those studies. In the past, the use of O isotopic labeling was used as a tool to evaluate transport and reaction mechanisms of high temperature oxidation of metals and Si [17-19]. Inspired by these approaches, this isotopic labeling used in this work was designed to ensure that the predictions of the HFM and the PDM made regarding anodic film structure, would be unique. By depth profiling the oxide films and comparing the resultant O depth profiles with the predictions of the two growth models, one could directly determine which one better predicts the experimental results.

Firstly, magnetron sputtering of Ti onto Si(001) substrates is performed. Then the Ti films are exposed to $H_2{}^{18}O$ to form passive oxides, without exposure to ambient conditions. These $Ti^{18}O_2$/Ti/Si(001) films are subsequently anodized at voltages from 0-10 V in $D_2{}^{16}O$. By depth profiling these films, the relative concertation of each O isotope as a function of depth can give insight into which growth model predicts such a structure. Figure 1.7 shows the O depth profiles predicted by the PDM and HFM. Quantification of the films is done by analysis of the backscattering ion energy distribution, described in Chapter 2. The schematic of the ion yield vs. energy in Figure 1.7 simply indicates that the backscattering spectra for each of the growth models will have ^{16}O and ^{18}O features that directly relate to the areal density of these isotopes as functions of depth through the films.

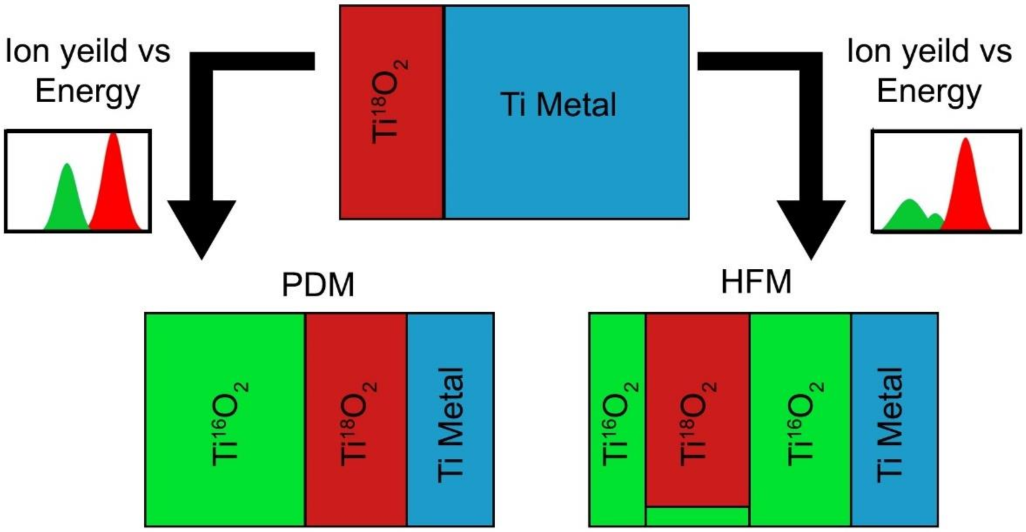

Figure 1.7: The predicted structure of the two stage oxidation procedure. On the left is the PDM prediction of the bi-layer structure. On the right is the prediction made by the HFM.

Since the original passive oxide that forms after exposure to $D_2{}^{18}O$ is $Ti^{18}O_2$, according to the PDM, it will be ^{18}O ions that move across the metal/oxide interface to react with the Ti metal substrate, resulting in a vacancy being created, that will be filled by ^{18}O ions immediately behind it. The vacancy migrates to the oxide/electrolyte interface and will eventually be consumed by a ^{16}O from the solution ($H_2{}^{16}O$). The process of cation vacancy generation and consumption happens in the opposite direction and begins when Ti ions are ejected into the electrolyte where they react with ^{16}O anions. The end result is that the barrier layer grows directly into the metal and adjacent to this, is an outer layer forms by precipitation of Ti cations in solution. As shown in Figure 1.7, the PDM predicts a bi-layer structure: $Ti^{16}O_2/Ti^{18}O_2/Ti/Si(001)$. Importantly, the concept of the original oxide is not coherent for the PDM, as the ^{18}O atoms that comprised the initial passive film, after anodization, will represent the extent of the corrosion front (i.e. the deepest point of Ti oxidation) and are always located adjacent to the metal and their initial movement past the metal/oxide interface is how the oxygen vacancies are generated in the first place. The Ti atoms in the original oxide were transported during anodization to the oxide/electrolyte interface where they are ejected and oxidized by the solution to form the precipitated outer layer that in this case would be entirely ^{16}O.

In the HFM, the concept of the original oxide is coherent, since from a simplified point of view, the original oxide is a passive medium that ions propagate through. According to the HFM, the original $Ti^{18}O_2$ region will be situated between two newly grown, $Ti^{16}O_2$ regions. Assuming that both Ti and O ions are mobile, Ti ions move from the metal/oxide interface, through the $Ti^{18}O_2$, to be ejected into the electrolyte where they from new $Ti^{16}O_2$ layer. Simultaneously, ^{16}O ions from the electrolyte are transported in the opposite direction, through the $Ti^{18}O_2$ to reach the metal where they react to from a second region of $Ti^{16}O_2$. The result is a $Ti^{16}O_2/Ti^{18}O_2/Ti^{16}O_2/Ti/Si(001)$ structure which is also depicted in Figure 1.7. The thickness of the two new $Ti^{16}O_2$ oxide layers need not be the same length, but will rather reflect the relative mobilities of each species that resulted in that growth. In fact, the thickness of the oxide due to O should be 65 % and oxide growth due to Ti should be 35%. In Figure 1.7, a small concertation of ^{16}O might be observed through the extent of the $Ti^{18}O_2$ given that the ions must be transported through this region.

1.2 Ion matter interactions and energy loss

Any incident ion that penetrates a solid target will experience a series of interactions with atomic nuclei and electrons. This process results in energy loss of the incident ions, dE/dx, with values on the order of a few hundred eV/nm [20]. The factors most consequential to energy loss are: the incident energy E_0, incident atomic number Z_1, and atomic number of the target Z_2 [21]. A precise estimate of dE/dx, is vital to ion beam analysis (IBA), as the conversion between an measured energy loss and an ions depth in the sample, is how these techniques obtain their depth scales [22]. This is excluding effects related to the sample crystallinity and crystal lattice orientation, which are discussed in the next chapter.

Importantly, the collisions with nuclei and electrons, the distance traveled between collisions, and the energy lost in each collision are all stochastic. The cumulative effect of this ΔE_i summed over all incident ions is known as energy straggling, which can lead to a spreading out of a once monoenergetic beam and degrading depth resolution [20].

1.2.1 Mechanisms of ion energy loss

There are two main ways in which energy loss occurs for an incident ion: (1) nuclear collisions in which the ion transfers energy as translational motion to a target nuclei, and (2) electronic collisions in which the ion excites or ejects atomic electrons [22]. The total energy loss can be expressed as a summation of two independent components:

$$\frac{dE}{dx} = \frac{dE_n}{dx} + \frac{dE_e}{dx} \qquad (1.7)$$

where the subscripts, *n* and *e*, denote nuclear and electronic energy loss respectively. The energy loss is often called ion stopping.

The backscattering techniques described in Chapter 2 exploit nuclear collisions that involves large discrete energy transfers and significant angular deflection of the ion's trajectory and this process even produces lattice disorder by displacing atoms in the target. The resultant deflection of the ion may be utilized, most notably by Rutherford backscattering spectrometry (RBS), by positioning a detector at the angle of deflection to measured backscattered ion energy. For electronic stopping, projectile energy is lost from target electronic excitations, typically 1-10 eV per collision, this process does not induce lattice disorder or significant deflection of the projectile trajectory. Nuclear stopping is more significant at lower E_0 ($E_0 < 40$ keV/amu) and high Z_1. Electronic stopping predominates at high E_0 ($E_0 > 40$ keV/amu) and low Z_1, due to the much higher probability of projectile-electron collisions. The species of incident ion (Z_2) is also a factor.

The stopping cross section for element A is defined as:

$$\varepsilon_A = \frac{1}{N}\frac{dE}{dx} \qquad (1.8)$$

where *N* is the atomic density. This is a measure of the energy loss per scattering center and typically has units of eVcm^2/atom [20]. It is often called stopping power in the literature. The stopping cross sections for protons in Ti and Si and He ions in Ti are plotted in Figure 1.8.

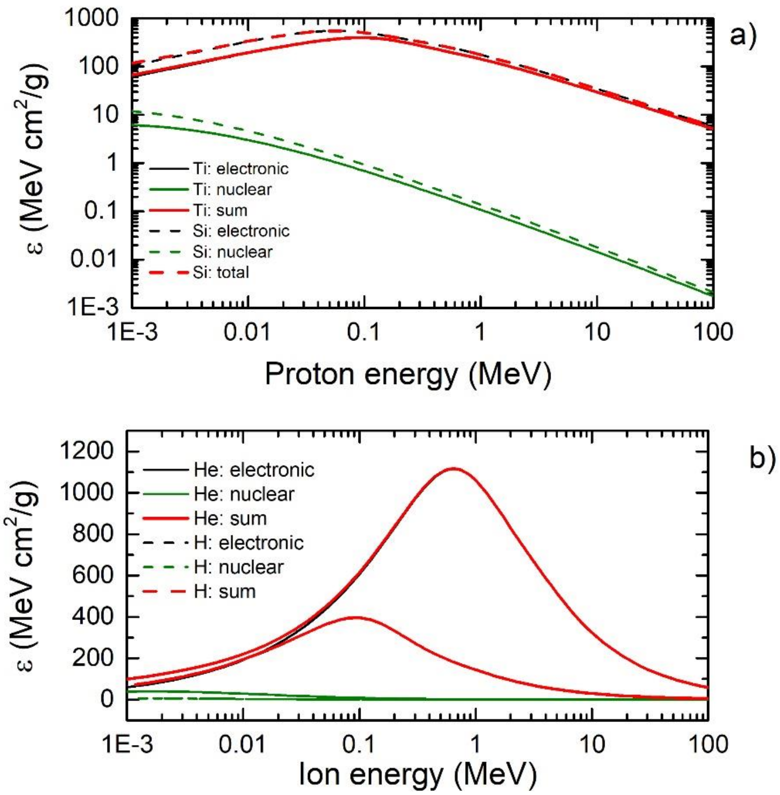

Figure 1.8: a) The stopping powers for protons in Ti and Si over a range of energies 0.001-100 MeV, including separate nuclear and electronic contributions, as well as their summation. For the entire energy range, the electronic stopping dominates and to a good approximation represents the entire stopping, b) the stopping powers for protons and alpha particles in Ti for energies 0.001-100 MeV illustrating the Z_i dependence.

Figure 1.8 illustrates the dependence of the energy loss on the incident energy, target atom, and incident ion. The nuclear stopping of protons begins to become significant below 10 keV but even at this energy, nuclear stopping only accounts for 1-2 %. It is apparent, that most IBA applications will involve energy loss dominated by electronic stopping and to an accurate approximation, only that energy loss need be considered. That is true of the regime relevant to the present work, namely the high energy (E > 400 keV/amu) and medium energy (40 keV/amu < E< 400 keV/amu) ranges.

Ion stopping is proportional to energy, which means it is proportional to the square of the ion velocity (recalling that $E \propto v^2$), and may be discussed in terms of either. Often it is advantageous to have a rough idea of the proportionalities and scaling involved in the regimes of energy loss. At ion velocities much lower than the Bohr velocity of the atomic electrons ($v_0 = 2.18\times10^8$ cm/s) the ion will retain its electrons and tends to be neutralized by electron capture [20]. At these energies, elastic collisions with the target nuclei dominate energy loss. Increasing the ion velocity will decrease the nuclear stopping by $1/E_0$, after which electronic stopping will begin to dominate [21].

In the velocity range $0.1v_0$ to $Z_1^{2/3}v_0$, the electronic stopping is proportional to v (or $E^{1/2}$). With increasing velocity, the charge state of the ion increases until it becomes fully ionized at $v > Z_1^{2/3}v_0$ and the ion can be viewed as a point charge. When the ion velocity greatly exceeds that of the orbital elections, the interaction between the atom and ion can be treated as small sudden external perturbation, which is described by Bohr's theory of stopping and treats the interaction is as a purely Coulombic potential [22]. In the high energy regime the stopping cross section are $\propto (Z_1/v)^2$ and decrease with increasing velocity since the point charge spends less time in the location of the target. The electronic energy loss at these velocities can be expressed as [23]:

$$\varepsilon_e = \frac{Z_2 {Z_1}^2}{v^2}\left(\frac{4\pi e^4}{m_e}\right) ln\left(\frac{2m_e v^2}{I}\right) \tag{1.9}$$

where e is the electronic charge, m_e is mass of electron, and I is the mean excitation potential. The mean ionization potential, I, is theoretically give as:

$$ln\, I = \sum_n f_n lnE_n \tag{1.10}$$

where E_n and f_n are the possible energy translations and corresponding oscillator strengths for a target atom respectively. This is intractable to calculate but can be estimated using an empirically derived formula (Bloch's rule):

$$I = I_0 Z_2 \tag{1.11}$$

where I_0 = 10 eV and Z_2 is the atomic number of the stopping atoms. For example, for O (Z=8), I = 80 eV.

In the low energy regime (E < 30 keV/amu) the Lindhard-Scharff model can be used to calculate the electronic energy loss:

$$\varepsilon_e = \frac{8\pi e^2 a_0}{v_0} \frac{{Z_1}^{7/6} Z_2}{\left(Z_1^{2/3} + Z_2^{2/3}\right)^{3/2}} v \tag{1.12}$$

Given that the theory for low energy formulation is often inaccurate and that for intermediate energies there is no equivalent theory that describes the electronic energy loss, means that one must rely on semi-empirical equations that are fit to large amounts of existing stopping cross section data. Andersen and Ziegler (AZ) give a semiemperical way to estimate the stopping cross sections for protons ε_H [eVcm^2/10^{15}atoms], ε_H:

$$\varepsilon_H = \frac{S_{Low} S_{High}}{S_{Low} + S_{High}} \tag{1.13}$$

$$S_{Low} = A_1 E^{0.45} \tag{1.14}$$

$$S_{High} = \frac{A_2}{E} ln\left(1 + \frac{A_3}{E} + A_4 E\right) \tag{1.15}$$

$$A_4 = \frac{4m}{IM_1} \tag{1.16}$$

where $A_1 - A_4$ are element specific fitting constants [24]. Equation 1.13 agrees with Equation 1.12 in the low energy limit and with Equation 1.9 in the high energy limit. Explanation of how the above set of equations was generated is given below.

In the high energy regime, the rate of energy loss is given by the Bethe stopping power formula [25], which is Equation 1.9 modified to include shell corrections (C/Z_2) and relativistic terms ($\beta=v/c$):

$$\varepsilon_e = \frac{Z_2 {Z_1}^2}{v^2}\left(\frac{4\pi e^4}{m_e}\right)\left[ln\left(\frac{2m_e v^2}{I}\right) + ln\left(\frac{1}{1-\beta^2}\right) - \beta^2 - \frac{C}{Z_2}\right] \tag{1.17}$$

In the high energy regime, pre-existing experimental stopping cross section data for E>400 kev/amu was considered. The energy loss depends on particle velocity but not mass, so the data relating to protons, deuterons, and tritons was aggregated together. For I-values, Andersen and Ziegler again relied on available experimental data. By inverting Equation 1.17 and using experimental I-values, the shell-corrections were calculated (C/Z_2) for every data point of every element in the energy regime. With the additional assumption that C/Z_2 varies smoothly with Z_2, the set of all shell-corrections for 27 elements where fitted by a power series:

$$\frac{C}{Z_2} = a_0 + a_1 lnE + a_2(lnE)^2 + a_3(lnE)^3 + a_4(lnE)^4 \tag{1.18}$$

Shell corrections for other elements where there was no experimental data available were done with a linear interpolation of Z_2 to which a 2nd power series was fit. Using Equation 1.18, the corrected Bethe stopping cross sections were calculated with Equation 1.17 and fit with Equation 1.15, S_{High}. In the low energy region there were 24 elements with sufficient data to allow for their fitting procedure. The experimental stopping powers, for the 24 elements in the low energy region, were fitted to Equation 1.14, S_{Low}.

Andersen and Ziegler estimate the accuracy of the fit to be 5% at 500 keV, which decreases with lower energy to 10% around 10 keV, for elements in which a lot of data exists, but conclude that for elements which had to be interpolated it could be as high as 20%. This approach has been refined over the past decades by incorporation of a larger set of empirical data [26, 27].

For a target that contains more than a single element, the stopping cross section of that compound is estimated by a sum of the stopping cross sections weighed by their concentration. Bragg's rule gives the stopping cross section of an A_mB_n target:

$$\varepsilon_{\mathrm{AmBn}} = m\varepsilon_A + n\varepsilon_B \tag{1.19}$$

where ε_A and ε_B are the stopping cross section of the respective element. Bragg's rule and the experimental implications for multi-element targets will be discussed further in Chapter 3.

1.2.2 Experimental approaches for evaluating stopping cross sections

There are two primary approaches to measuring the scattering cross section of an ion in a particular medium using the physics of ion-solid interactions that was detailed in previous sections: transmission and backscattering experiments.

A transmission experiment is depicted in Figure 1.9, in which ions of energy E_0 pass through a target of thickness Δx and loose energy ΔE, and that energy loss is measured at a detector, $E_0 - \Delta E$. The stopping cross section of the incident ion in that medium is calculated to be $(1/N)(\Delta E/\Delta x)$, from Equation 1.7.

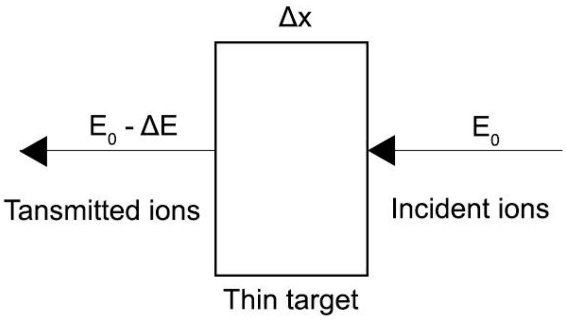

Figure 1.9: A schematic representation of a transmission experiment using incident ions of E_0. Ions pass through a thin film with thickness Δx and lose energy ΔE. Transmitted ions have their energy analyzed and $\Delta E/\Delta x$ can be calculated. Adapted from [22].

A backscattering experiment is depicted in Figure 1.10 where ions with energy E_0 are incident on a film of thickness Δx deposited on a substrate. This experiment results in an energy distribution of backscattered ions, in which the width of the spectral feature (ΔE) corresponding to the film, is directly proportional to the physical thickness of the film and to the stopping cross section of the film. If the Δx and ΔE are well known, the stopping cross section can be calculated from Equation 1.9.

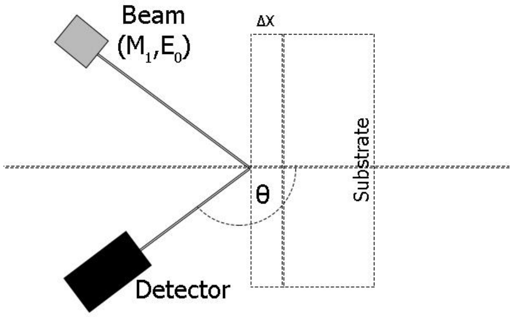

Figure 1.10: A schematic of a backscattering experiment used to measure stopping cross section of a film of thickness *Δx* on a substrate. The width of the spectra features (*ΔE)* in a backscattering spectra are directly proportional to the physical thickness of the film and to the stopping cross section of the film.

Both experimental approaches suffer from the same experimental complications and uncertainties associated with them. For example, Andersen and Ziegler [24] discuss the reasons for which the data on elemental stopping cross sections that they analyse in the low energy region has a general level of scatter of at least ± 10%. Subtle pitfalls exist for energy loss measurements, especially for low energy studies. For low energy measurements, very thin targets are required, which can often be difficult to create without introducing pinholes. This was especially true for data acquired with older equipment, which did not have the energy-resolution to show the existence of pinholes, which lowered the stopping cross sections [24]. Additionally, the “target texture” is important as well; some polycrystalline materials do not have their crystallites aligned randomly and channeling effects, where incident ions are steered through the crystal lattice resulting in fewer collisions, might exist that lowers the measured energy loss. The purity of a target may also be a source of uncertainty, especially for oxidized earth alkali and rare earth metals.

Even if the elemental concentration is known, deviations from Bragg’s rule might exist for compounds. Substantial deviations from Equation 1.19 for experimentally determined stopping cross sections due to modification of electronic density in compounds are referred to as chemical effects [6]. If the stopping cross sections used where derived from a phase different to that in the present phase, then this might lead violations of Bragg's rule, referred to as physical effects [28]. For example the difference in stopping powers between a solid and gaseous target. Such deviations from Bragg's rule are most significant near stopping power maximum, which for protons this is about 100 keV for many materials. Comprehensive reviews of Bragg's rule have been carried out, as it applies to organic compounds [28-30], oxides [31-33] and other compounds [34].

Available experimental stopping cross sections for protons in Si and Ti for the medium energy range are depicted in Figure 1.11. The stopping cross sections for Si and Ti are also estimated with two semiempirical formulations from SRIM [27] and the database PSTAR [35]. At stopping power maximum ε_{Ti} is limited to two data sets and as such, it is hard to judge its accuracy or the quality of the semiemperical fits. More data is necessary to reach any conclusions about where stopping power maximum occurs and its value. This is true despite the good agreement between SRIM and ε_{Ti} values greater or less than stopping power maximum. Conversely, there is a large amount of data for ε_{Si} but there is significant variation between studies. This can be as large as 20% despite the reported percent error for these studies being reported to be from 0.25% - 8%.

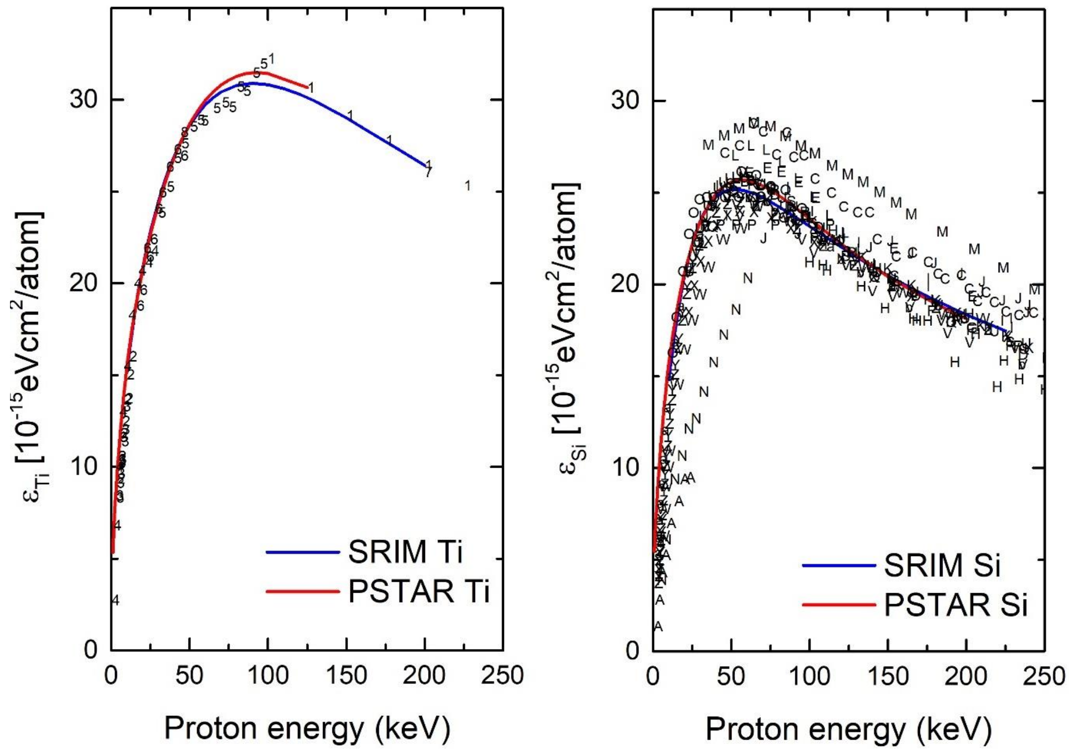

Figure 1.11: Available literature values for the stopping cross sections of 0-250 keV protons in Ti and Si. Data from: A[36], C[37], D&E[38], F[39], G[39], H[40], I[41], J-L[42], M[43], N[44], O[45], P[46], Q-S[47], U[48], V[49], W[50], X[51], Y&Z[52], a[53], b[54],1[39], 2-6[55], 7[56].

Available experimental data for specific elements can be limited but the situation is often more constrained when one considers compounds. In general, there less data available for compounds at stopping power maximum. For example, Figure 1.12 depicts all available literature data for protons in any energy range for a TiO_2 target. The two available data sets are far past stopping power maximum, where deviations from Bragg's rule are most likely to occur.

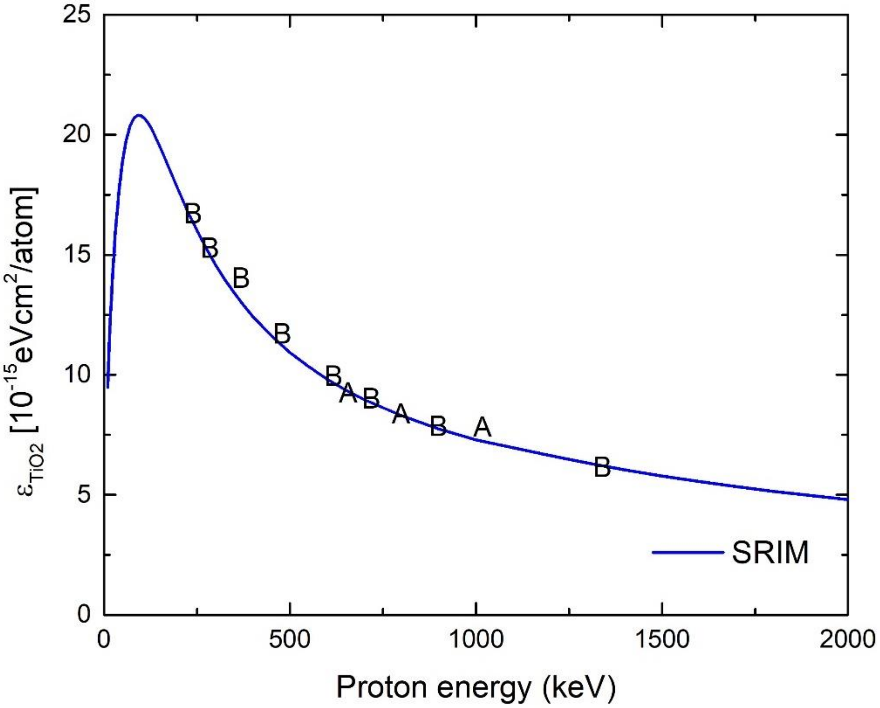

Figure 1.12: Available literature values for the scattering cross section for TiO_2 as well as SRIM values. No data exists at the stopping power maximum where deviations from Bragg's rule would be most apparent. A [57], B [58].

Given that a depth scale in ion beam analysis is obtained by a product of the measured energy loss through a target and the stopping cross section of that target, good estimates of ion stopping are necessary to accurately depth profile films using IBA. The underlying physics and use of energy loss in IBA techniques will be given in detail in Chapter 2. Chapter 3 provides a detailed account of how to accurately measure stopping cross sections for elemental and compound ultra-thin films, specifically Ti and TiO_2.

Chapter 4 utilizes IBA techniques to preform high resolution depth profiling in conjunction with an isotopic labeling procedure outlined in this chapter to elucidate the anodization mechanisms of Ti anodization, which requires good estimates of stopping power of protons in Ti and TiO_2. Chapter 5 introduces an electrochemical cell that was designed to perform *in situ* IBA, in an attempt to avoid compositional changes that can occur in anodic oxide films when moved from ambient to UHV conditions. Chapter 6 summarizes the major conclusions of the present work and provides future directions such research can proceed in.

1.3 References

1. E. Bowman, *International measures of prevention, application, and economics of corrosion technologies study*. 2016, NACE International
2. D.D. Macdonald, *Passivity–the key to our metals-based civilization.* Pure Appl. Chem, 1999. **71**: p. 951.
3. J. Lausma, et al., *Chemical composition and morphology of titanium surface oxides.* Mater Res. Soc. Symp. Proc. , 1986. **55**: p. 351.
4. J.F. Vanhumbeeck and J. Proost, *Current understanding of Ti anodization: functional, morphological, chemical and mechainical aspects.* Corrosion Reciews, 2009. **27**: p. 204.
5. D. D. Macdonald and G.R. Engelhardt, *The Point Defect Model for Bi-Layer Passive Films* ECS Transactions, 2010. **28**: p. 123.
6. D.D. Macdonald, *Some Personal Adventures in Passivity—a Review of the Point Defect Model for Film Growth.* Russian Journal of Electrochemistry, 2012. **48**: p. 235.
7. D.D. MacDonald, *The history of the Point Defect Model for the passive state: A breif review of film growth aspects.* Electrochimica Acta, 2011. **56**: p. 1761.
8. C.Y. Chao, L. F. Lin, and D.D. Macdonald, *A Point Defect Model for Anodic Passive Films - (I) Film Growth Kinetics.* J. Electrochem. Soc., 1981. **128**: p. 1187.
9. D.D. Macdonald, *The Point Defect Model for the Passive State.* 1992. **139**: p. 3434.
10. D.D. Macdonald, *Passivity: enabler of our metals based civilisation.* Corrosion Engineering, Science and Technology 2014. **49**: p. 143.
11. M.M. Lohrengel, *Thin anodic oxide layers on aluminium and other valve metals: high field regime* Materials Science and Egineering 1993. **11**: p. 243.
12. A. Gfintherschulze and H. Betz, *Die Bewegung der Ionengitter von Isolatoren bei extremen elektrischen Feldstärken.* Z. Phys., 1934. **92**: p. 367.
13. E.J.W. Verwey, *Eectrolytic conduction of a solid insulator at high fields The formation of the anodic oxide film on aluminium.* Physica, 1935. **2**: p. 1059.
14. N. Cabrera and N.F. Mott, *Theory of the Oxidation of Metals.* Rep. Prog. Physics 1948. **12**: p. 120.
15. N. Khalil and J.S.L. Leach, *He anodic oxidation of valve metals-i. determination of ionic transport numbers by a-spectrometry* Electrochimica Acta, 1986. **31**: p. 1279.
16. Z. Tun, J. J. Noël, and D.W. Shoesmith, *Electrochemical Modification of the Passive Oxide Layer on a Ti Film Observed by In Situ Neutron Reflectometry*. Journal of The Electrochemical Society, 1999. **146**: p. 130.

17. T. Akermark, *The Use of Oxygen Isotopic Labeling to Understand Oxidation Mechanisms.* Oxidation of Metals, 1998. **50**: p. 167.
18. H. C. Lu and T. Gustafsson, *An isotopic labeling study of the growth of thin oxide films on Si(100).* Applied Physics Letters, 1995. **67**: p. 1742.
19. S.N. Basu and J.W. Halloran, *Tracer isotope distribution in growing oxide scales.* Oxidation of Metals, 1987. **27**(3): p. 143.
20. M. Nastasi, J.W. Mayer, and Y. Wang, *Ion Beam Analysis fundamentals and applications*. 2014: Taylor & Francis Group.
21. Y. Wang and M. Nastasi, *Handbook of modern Ion beam materials analysis* 2009: Materials Reserch Scoiety.
22. W.K. Chu, J.W. Mayer, and M.A. Nicolet, *Backscattering Spectrometry*. 1978: Academic Press Inc.
23. M. Nastasi and J.W. Mayer, *Ion Implantation and Synthesis of Materials*. 2006, Berline Springer.
24. J.Z. H. Andersen, *Hydrogen. Stopping powers and ranges in all elements*. 1977, Toronto, Canada: Pergamon Press, Inc.
25. P. Sigmund, *Particle penetration and radiation effects*. 2008, New York: Springer.
26. J.F. Ziegler, *Stopping of energetic light ions in elemental matter.* J. Appl. Phys. , 1999. **85**: p. 1249.
27. J.F. Ziegler, *SRIM-2003.* Nucl. Instrum. Meth. Phys. Res. Sect. B 2004. **219**: p. 1027.
28. D. Thwaites, *Review of stopping powers in organic material.* Nucl. Instrum. Meth. Phys. Res. Sect. B, 1987. **27**: p. 293.
29. J. Oddershede and J. Sabin, *Bragg rule additivity of bond stopping cross sections.* Nucl. Instrum. Meth. Phys. Res. Sect. B 1989. **42**: p. 7.
30. D. Powers, *Influence of Molecular Structure on Stopping power of Chemical Species for He+ Ions from a Low-Energy Particle Accelerator.* Acc. Chem. Res. , 1980. **12**: p. 433.
31. C. Pascual-Izarra, et al., *Stopping power of SiO2 for 0.2-0.3 MeV He ions.* Nucl. Instrum. Meth. Phys. Res. Sect. B, 2002: p. 209.
32. Y. Hoshino, et al., *Correction of Ziegler's stopping powers of Al, Si and their oxides for MeV He ions.* Nuc. Inst. & Meth. Phys. B, 2000. **171**: p. 409.
33. W. N. Lennard, H. Xia, and J.K. Kim, *Revisiting the stopping powers of Si and SiO2 for 4He ions: 0.5-2.0 MeV.* Nucl. Instrum. Meth. Phys. Res. Sect. B, 2004. **215**: p. 297.
34. D. Thwaites, *Bragg's rule of stopping power additivity: A compilation and summary of result.* Radiat. Res., 1983. **95**: p. 495.
35. M.J. Berger, et al., *Stopping-Power and Range Tables for Electrons, Protons, and Helium Ions.* Rep. NISTIR 1992. **4992**: p. 43.
36. E.P. Arkhipov and Y.V. Gott, Sov.Phys.-JETP. **29**: p. 615.
37. A. Carnera, et al., *Channeled and random proton stopping power in the 30-1000 keV energy range.* Phys.Rev. B, 1978. **17**: p. 3492.
38. E. Kührt, K. Lenkeit, and F. Täubner, *Measurements of the stopping power of 40 to 300 keV protons in silicon.* Phys.Status Solidi A, 1981. **66**: p. 131.
39. D.C.Santry and R.D.Werner, *Stopping power measurements of C, Al, Si, Ti, Ni, Ag, Au and mylar using radioactive alpha sources.* Nuc. Inst. & Meth. Phys. B, 1981. **1**: p. 14.
40. F. Cembali and F. Zignani, *Determination of random and aligned stopping powers for 80–300 keV protons in silicon by back-scattering measurements.* Radiat.Eff., 2006. **31**: p. 169.

41. P. Gehrmann, K. Lenkeit, and R. Stolle, *Measurements of Proton Channeling Energy Losses in Silicon in the Intermediate Energy Region.* Phys.Status Solidi B, 1985. **131**: p. 519.
42. J.D. Pearce and R.R. Hart, *Stopping power measurements in the 20–150-keV region using thick target backscattering: 1H and 4He on carbon, silicon, and gold.* J.Appl.Phys., 1981. **52**: p. 5056.
43. P. Mertens and T. Krist, *Electronic stopping cross sections for 30–300 keV protons in materials with 23 ⩽ Z2 ⩽ 30.* Nucl.Instrum.Methods Phys.Res., 1982. **194**: p. 57.
44. H. Grahmann and S. Kalbitzer, *Nuclear and electronic stopping powers of low energy ions with Z ⩽ 10 in silicon.* Nucl.Instrum.Methods Phys.Res., 1976. **132**: p. 119.
45. E. Ligeon and A. Guivarc'h, *Hydrogen implantation in silicon between 1.5 and 60 kev.* Radiat.Eff., 1976. **27**: p. 129.
46. C. Foster, et al., *Random stopping power for protons in silicon.* Radiat.Eff., 1972. **16**: p. 139.
47. P. Mertens and P. Bauer, *Reference stopping cross sections for 30–600 keV protons in silicon.* Nucl.Instrum.Methods Phys.Res. B, 1988. **33**: p. 133.
48. C. Eppacher. 1995, Univ. of Linz: Austria.
49. A. Ikeda, et al., *mpact-parameter dependent stopping powers for MeV He ions in Si crystal.* Nucl.Instrum.Methods Phys. Res. B, 1996. **153**: p. 10.
50. M. Fama, et al., *Energy loss and angular dispersion of 2–200 keV protons in amorphous silicon.* Nucl. Instrum. Methods Phys.Res. B, 2002. **91**: p. 193.
51. D.Niemann, G.Konac, and S.Kalbitzer, *Stopping power measurements of 1H, 4He and 14N in Si in the energy range of 0.02–1 MeV/amu.* Nucl.Instrum.Methods Phys.Res. B, 1996. **118**: p. 11.
52. G.Konac, et al., *Energy loss and straggling of H and He ions of keV energies in Sib and C* Nucl.Instr.Methods Phys. Res. B, 1998. **136**: p. 159.
53. G. Hobler, K.K. Bourdelle, and T. Akatsu, *Random and channeling stopping power of H in Si below 100 keV.* Nuc. Inst. & Meth. Phys. B, 2006. **242**: p. 617.
54. M.Abdesselam, et al., *Irradiation damage induced on polyethylene terephtalate by 1.6MeV deuteron ions.* Nucl. Instrum. Methods Phys. Res. B, 2008. **266**: p. 3899.
55. J.H.Ormrod, *Electronic stopping cross sections of deutrons in titanium.* Nucl.Instrum.Methods Phys.Res., 1971. **95**: p. 49.
56. N. Sakamoto, H. Ogawa, and H. Tsuchida, *Stopping powers of Ti for protons from 0.2 to 13.5 MeV: Correction for the actual path length due to multiple scattering.* Nucl. Instrum.Methods Phys.Res. B, 2000. **164**: p. 250.
57. L. Zhang, *Kinetics of passive film growth and the segregation of alloying elements in passive systems*. 1995, The Pennsylvania State University.
58. S.P. Limandri, et al., *Stopping cross sections of TiO_2 for H and He ions.* Eur. Phys. J. D 2014. **68**: p. 194.

Chapter 2: Experimental methods

Modern technology is to a very large degree a direct consequence of innovations in materials science. A material's properties, their function, and performance is completely dependent on their structure and composition. Further complications arise when one considers that surface layers, interfaces, and thin-films have their own unique properties that differ from the behaviour of the bulk material. Such structures can be created with a variety of common techniques: molecular beam epitaxy, physical and chemical vapour deposition, ion implantation, sol-gel coatings, etc.[1]. The techniques of ion beam analysis (IBA) offer a quick, non-destructive, and quantitative way to characterize these systems. The basis of many IBA techniques is Rutherford Backscattering Spectrometry (RBS), which utilizes the interaction between ion beams, typically in the 0.5 - 4 MeV range [2], and target condensed media.

2.1 Rutherford backscattering spectrometry

Figure 2.1 depicts a typical RBS experiment where a monoenergetic incident ion beam is collimated and directed towards the target. A small fraction (0.01 %) of the incident ions are backscattered from the target to a detector, due to repulsive Coulombic interactions between the ions and the target nuclei. The angle of the incident ion beam relative to the target surface, the incident beam energy (E_0), ion species (Z_1), and detector geometry relative to the incident angle (θ) are experimental parameters that will be held constant. For a given set of experimental parameters, each backscattered ion will have its energy recorded, and an analysis of the resulting energy distribution of backscattered ions can provide useful quantitative information about the target composition such as elemental depth profiles and will be described in the following sections.

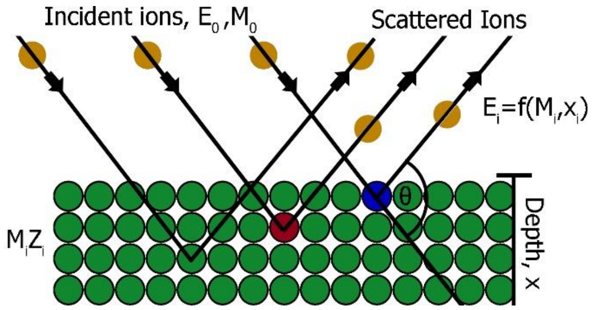

Figure 2.1: Schematic of a RBS experiment in which incident ions with known mass M_0 and energy E_0 are backscattered off a variety of target nuclei of charge Z_i and mass M_i, each located at a depth x_i, to a detector at angle θ relative to the direction of the incident beam.

A brief note on experimental implementation is required to facilitate understanding of how RBS spectra are generated and how to interpret spectral features. The typical RBS detector is a silicon surface barrier detector [3] and the backscattered ions that impinge upon it will generate an analog signal proportional to the detected ion's energy. The signal is then processed by a multichannel analyzer (MCA) which operates in pulse-height analysis mode and records the number of pulses based on amplitude (i.e. the energy of the backscattered ions). By discretizing the possible amplitudes, each increment is numbered and referred to as a channel. Each channel number that can be converted using a linear function into a backscattered ion energy. The net effect is that RBS spectra depict the number of counts as a function of channel number. A relationship to convert the channel number to the energy of a detected particle must be used. Such a relationship must be determined experimentally, typically through the use of a calibration standard.

RBS allows accurate stoichiometric determination via the identification of atomic masses and elemental areal density as a function of depth [4]. The relevant physical parameters governing the process of ion-matter interaction must be taken into consideration to extracted information about elemental depth distributions and other quantitative parameters. The kinematic factor (Chapter 2.1.1) provides mass sensitivity, the scattering cross section (Chapter 2.1.2) is the probability of a backscattering event and linearly proportional to backscattering yield (or intensity), and stopping cross section (Chapter 2.1.3) is the energy loss of the ion as it penetrates through a particular medium and provides depth information. Statistical fluctuations in energy loss of the ions moving through matter, known as energy straggling, will set limitations on ultimate mass and depth resolutions of this technique [5].

2.1.1 Kinematic factor

Consider a collision between an incident ion and target atom, as depicted in Figure 2.2. The mass of the incident ion will be M_1 and the mass of a target atom to be M_2 (stationary in the laboratory reference frame). The interaction between them can be modeled as a classical two-body collision [2]. The collision is assumed to be elastic, in which energy is conserved, based on the assumptions that the incident ion energy is much greater than the binding energy (~10 eV for chemical bonds) in the target medium and that nuclear reactions and nuclear resonances are absent, i.e. ruling out inelastic collisions [5]. For inelastic collisions, the energy lost may not be present in the post-collision kinematics [1].

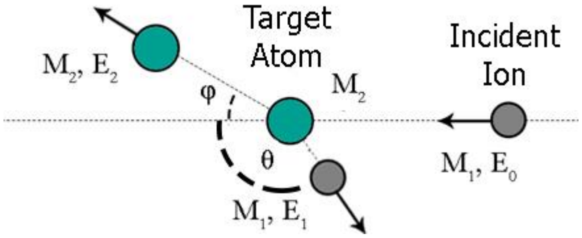

Figure 2.2: Schematic of a scattering event in laboratory reference frame, between incident ion M_1 with energy E_0 and target atom M_2, initially at rest. After the collision, the recoiled atom M_2 departs at an angle φ with energy E_2 and M_1 is backscattered at angle θ relative to the incident direction and with energy E_1. Adapted from [5]

Under these conditions, the conservation of kinetic energy and conservation of parallel and perpendicular momentum can be solved to determine the energies of the particles, E_1 and E_2, after collision. Taking the ratio of the scattered ion energy, E_1, and its initial energy prior to collision, E_0, results in Equation 2.1 [1]:

$$K = \frac{E_1}{E_0} = \left[\frac{\sqrt{(M_2^2 - M_1^2 sin^2\theta)} + M_1 cos\theta}{M_1 + M_2}\right]^2 \tag{2.1}$$

where K is known as the kinematic factor and depends only on the masses of the particles and the scattering angle, θ. For the condition that $M_1 < M_2$, all values of $0 \geq \theta \geq \pi$ are possible. When $M_1 = M_2$, K is zero for $\theta > 90^0$ which implies that an incident ion interacting with a target of equal mass will not result in backscattering and will only be scattered in the forward direction.

In a typical RBS set up, the scattering angle, θ, is typically fixed by detector position, while the ion mass, M_1, and its incident energy, E_0, are selected for and are known. If the energy of the backscattered ions, E_1, is measured it is a simple matter to determine the mass of the target, M_2, through Equation 2.1. This illustrates how RBS derives its mass sensitivity and in turn allows one to identify the elements present in the sample material. Each element (or isotope) has a specific mass and the different masses backscatter ions at different energies, based on their respective kinematic factors, as illustrated in Figure 2.3. Separation between backscattering signals from different elements can be maximized at higher θ.

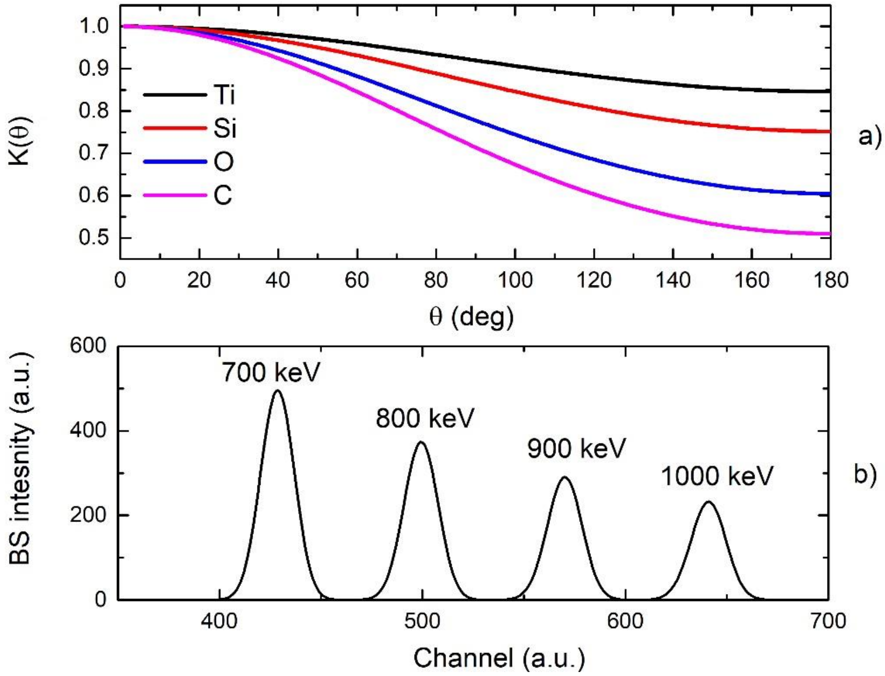

Figure 2.3: a) The kinematic factor, *K*, as a function of scattering angle, θ, for Ti, Si, O, and C for an He^+ beam, b) The effect of different E_0 on *K* in the resultant RBS spectra for the same (100 atom/cm^2) Ti target, using a He^+ beam at 0^0 incidence, and $\theta = 170^0$. The FWHM of the Ti spectra is due to the E^{-2}, dependence on the backscattering intensity (see Chapter 2.1.2).

K defines the “high-energy edge” of each element, i.e. the highest energy or channel number at which the element will be detected. The different peak intensities are explained by the cross sectional dependence on E_0, which is explained in the following section. If the masses of different elements in a target differ greatly, so too will their kinematic factors and their differentiation and identification is easy, as heavier elements will always have higher kinematic factors than lighter elements. A small *ΔM* may present challenges as the difference between their kinematic factors could be quite small and lead to an overlap in their peaks. Modifying the scattering angle however, can result in a greater difference in kinematic factors and greater separation in scattered ion energy. For fixed masses M_1 and M_2, the greatest change in K is when θ is close to 180° or fully backscattered back in the direction of the beam. In practice the detector is placed at 160-170^0 so it does not block the incident beam.

2.1.2 Scattering cross section

The kinematic factor offers no insight into the frequency that a backscattering even will occur. The differential cross section can be interpreted as the probability of scattering an incident projectile into some angler range between θ and $\theta+d\theta$. The differential cross section has units of barns (1 barn = 10^{-24} cm^2), making it an analogue of geometrical cross-sectional area.

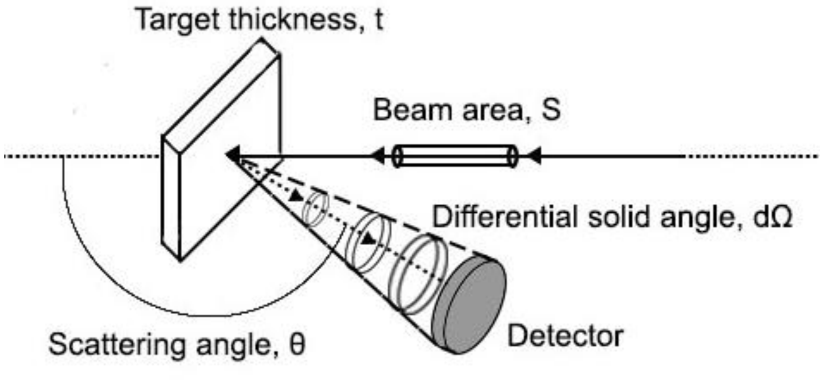

Figure 2.4: Schematic of a backscattering experiment to illustrate the differential cross scattering cross section. Only ions scattered within the solid angle $d\Omega$ spanned by the detector are measured. Adapted from [4].

Figure 2.4 shows a beam of incident ions impinging on a thin uniform target. Given some detector at θ relative the direction of the incident beam, which counts each ion scattered in the differential solid angle of $d\Omega$. Take Q to be the total number of particles that have hit the target, the differential scattering cross section $d\sigma/d\Omega$ is defined as [5].

$$\frac{d\sigma}{d\Omega} = \frac{1}{Nt}\frac{1}{Q}\frac{dQ}{d\Omega} \tag{2.2}$$

where N is the volume density of atoms in the target, t is the thickness of the target, and Nt is the areal density (atoms/cm^2). The assumption of the target being thin is required so that the energy loss through the target are negligible, i.e. the energy of the incident ions is the same at any depth in the target. Each nucleus of an atom in the target will expose an area of $d\sigma/d\Omega$ to the incident beam. Implicit in this is that the area is very small and that the atoms are randomly distributed so that the individual $d\sigma/d\Omega$ do not overlap [5].

If the area under the beam is A, then there are $A(Nt)$ atoms that contribute a total cross sectional area of $A(Nt)(d\sigma/d\Omega)$. The ratio of this to the area A can be interpreted as the probability that a scattering event will occur. Equation 2.2 follows from setting $(Nt)(d\sigma/d\Omega)$ equal to $(1//d\Omega)(dQ/Q)$, which is itself the probability that the scattering will be recorded by the detector. Thus, the cross section is defined as a value per unit of solid angle, which is why it is called differential scattering cross section.

For elastic collisions, the differential cross section is calculated by the conservation of energy and momentum, with the additional assumption of the Coulombic force mediating the interaction during the collision between incident and target particles. This interaction is valid as long as the distance of closest approach is taken to be larger than the nuclear dimensions but small relative to the Bohr radius ($a_0 = \hbar/m_e e = .53\,\mathring{A}$) [5]. Under these assumptions, Rutherford's formula for the differential cross section with respect to the center-of-mass coordinates is:

$$\frac{d\sigma}{d\Omega} = \left(\frac{Z_1 Z_2 e^2}{4E_0 sin^2(\theta)}\right)^2 \tag{2.3}$$

where Z_1 is the atomic number of the incident ions, Z_2 the atomic number of the target atom, e is the electronic charge and E_0 the energy before scattering.

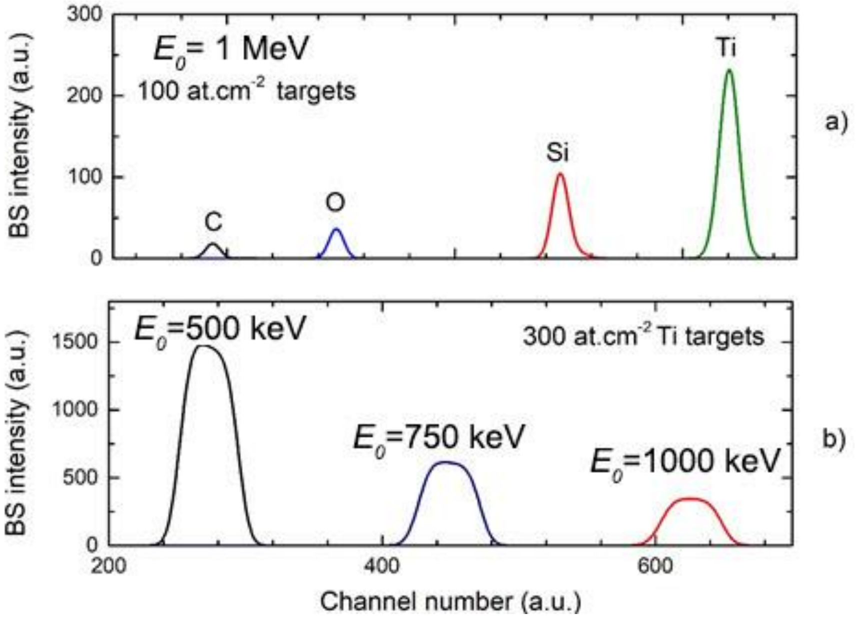

Figure 2.5: a) Illustrating the Z_2^2 dependence of the scattering cross section on the RBS spectra yield, using a 1 MeV He$^+$ ion beam at 0^0 incidence and $\theta = 170^0$ impinging on Ti, Si, O and C targets with the same elemental areal density (100 atoms/cm^2), b) Illustrating the E_o^{-2} dependence of the scattering cross section on the RBS yield with the using the same geometry as above but with the same Ti target (300 atoms/cm^2).

Given the Z_2^2 dependence, heavier atoms are much more efficient at scattering than lighter atoms and so RBS is much more sensitive to higher Z_2 targets. From Equation 2.3, the backscattering yield is proportional to Z_1^2 and thus lighter ion beams will result in lower intensity. The cross section is inversely proportional to $E_{0,}^2$ so the yield rises rapidly with decreasing energy. The cross section is axially symmetric with respect to the axis of the incident beam and a function of θ only. Lastly, the scattering intensity will fall rapidly as θ is decreased, given the inverse fourth power of $\sin\theta$.

The order of magnitude for the differential cross section is typically given by the first factor on the right hand side of Equation 2.6, besides this factor, the differential cross section depends on the scattering angle θ and the ratio M_1/M_2. In this instances given a combination of masses, the differential cross section is minimized at $\theta = 180^\circ$.

It is possible to consider the total number of backscattering events falling into a solid angle Ω, as opposed to a differential solid angle, $d\Omega$. However, in practice the detector angle Ω can be small (10^{-2} sr or less for typical silicon surface barrier detector) and if θ is well defined, it is convenient to introduce an average differential scattering cross section:

$$\sigma = \frac{1}{\Omega}\int\left(\frac{d\sigma}{d\Omega}\right)d\Omega \tag{2.4}$$

which in the limit of $\Omega \rightarrow 0$ becomes $\sigma \rightarrow d\sigma/d\Omega$. It is often referred to as scattering cross section in the literature.

For a backscattering experiment, the scattering yield of an individual element can be expressed as a function of cross section [6],[2]:

$$Y = \sigma \times \Delta\Omega \times Q \times N\Delta t \tag{2.5}$$

If the number of incident ions, Q, and total number of detected ions, Y, are counted while σ and $\Delta\Omega$ are both known, the elemental areal density, $N\Delta t$, can be calculated from Equation 2.6. However, the detector solid angle $\Delta\Omega$, cannot be accurately measured. This is partly because the active region of a detector is difficult to assess. In such cases, the product of $Q\Delta\Omega$ can be measured by use of a standard, with a well-defined areal density. Taking the ratio of scattering yields gives:

$$N\Delta t = \frac{\left(\frac{d\sigma}{d\Omega}\right)_s}{\left(\frac{d\sigma}{d\Omega}\right)} \frac{Y}{Y_s} (N\Delta t)_s \tag{2.6}$$

where Y_s is the yield of the standard with well defined $(d\sigma/d\Omega)_S$ and $(N\Delta t)_s$.

Derivation of the Rutherford cross sections assume that the interaction between particles is Coulombic. This implies that at sufficiently large particle energies they penetrate into the orbitals of the atomic electrons and that the scattering is strictly due to the electric repulsion of two nuclei Z_1 and Z_2. Experiments show that there are departures from this at high and low energies [1]. At low energies, there is the screening of the nuclear charge by the electron orbitals surrounding both nuclei, while the high energy departures are caused by short-range nuclear forces. The real cross section is expressed in terms of the product of the Rutherford cross section, σ_R, and a correction factor, F:

$$\sigma = F\sigma_R \tag{2.7}$$

For the low energy effect, the distance of closest approach, d, must be smaller than the K-shell electron radius. The K-shell radius is estimated as a_0/Z_2, where a_0 is the Bohr radius. Thus the lower energy limit must be [1]:

$$E > \frac{Z_1 {Z_2}^2 e^2}{a_0} \tag{2.8}$$

It has been empirically determined that the correction factor in these instances can be expressed as

$$F = \frac{\sigma}{\sigma_R} = 1 - \frac{0.049\, Z_1 Z_2^{4/3}}{E} \tag{2.9}$$

As such, it depends on the ion and target but typical values range from $0.85 \leq F \leq 1$[7].

2.1.3 Stopping cross section

Upon penetrating a solid target, an energetic ion will typically undergo a series of collisions with nucleus and electrons of the target and energy will be lost at a rate *dE/dx*, typically at a few hundred of eV/nm [1]. The details of the process have already been discussed in detail in Chapter 1.2. Recall that stopping cross section is defined as:

$$\varepsilon = -\frac{dE}{dx}\frac{1}{N} \tag{2.10}$$

where N is atomic density and the units of ε are eV/(atoms/cm^2).

If the stopping cross section is well defined, the energy after an ion traverses a depth of x into a target is given as:

$$E(x) = E_0 - N\int_0^z \varepsilon(E)dx \tag{2.11}$$

According to which, changes in energy before and after a backscattering event depend on the depth that the ion has to traverse before the backscattering and again the distance the backscattered ion must traverse to reach the detector.

Conversely, if the energy at a given depth, *E(x)*, is well defined, one can convert to the corresponding depth that the ion has traveled with:

$$x = \frac{1}{N}\int_{E(x)}^{E_0} \frac{1}{\varepsilon} dE \tag{2.12}$$

Appendix A2 has a detailed description of a numerical calculation and associated python code, which divides a thin film of known thickness and composition into *n* sublayers of equal width, Δx, and uses Equation 2.11 to calculate the energy at the surface of each sublayer. By doing this, the energy loss through each layer can be calculated, ΔE_i , and by summing the energy loss over all sublayers, the total energy loss experienced by an ion as it traverses the extent for the film. Ultimately this procedure be applied iteratively, by comparing the calculated energy loss, to a measured experimental energy loss through the same film, to estimate stopping cross sections. The details of how this is used in practice are presented in Chapter 3, which will measure the energy loss and thickness from IBA spectra, and derive experimental stopping cross sections.

2.1.4 Sample RBS spectra

To summarize the three central properties important to RBS, the effect of kinematic factor, scattering cross section, and stopping cross section are considered in Figure 2.6, which depicts an RBS spectra (yield vs channel number) of a film of element A and thickness Δx on substrate of element B. Incident ions with energy E_0 will backscatter at the surface and their energy will be $K_A E_0$ at the detector given the film only contains element A, where K_A is the kinematic factor of A. The shape if the A feature in the RBS spectra is slightly asymmetric and the intensity rises towards the low energy edge. This is due to the energy dependence, E^{-2}, of the scattering cross section on the backscattering yield. The ions traveling through film A will lose energy due to the stopping cross section ε_A and so the further into A the ions travel, the higher the scattering cross sections and the higher the intensity. The width (ΔE) of the feature is linearly proportional to the thickness of the film itself and thicker films produce wider RBS peaks. Given the Z_2^2 dependence of the scattering cross section, the intensity due to element B is lower than that from A, i.e. elements of higher atomic number give higher yields in RBS than those lower atomic number. If there was no film on substrate B, ions backscattering off the surface of it would have energy $K_B E_0$ where K_B is the kinematic factor of element B. However, the ions that penetrate the entire Δx of A will lose $\varepsilon_A \Delta x$ and upon backscattering will have energy $K_B(E_0 - \varepsilon_A \Delta x)$.

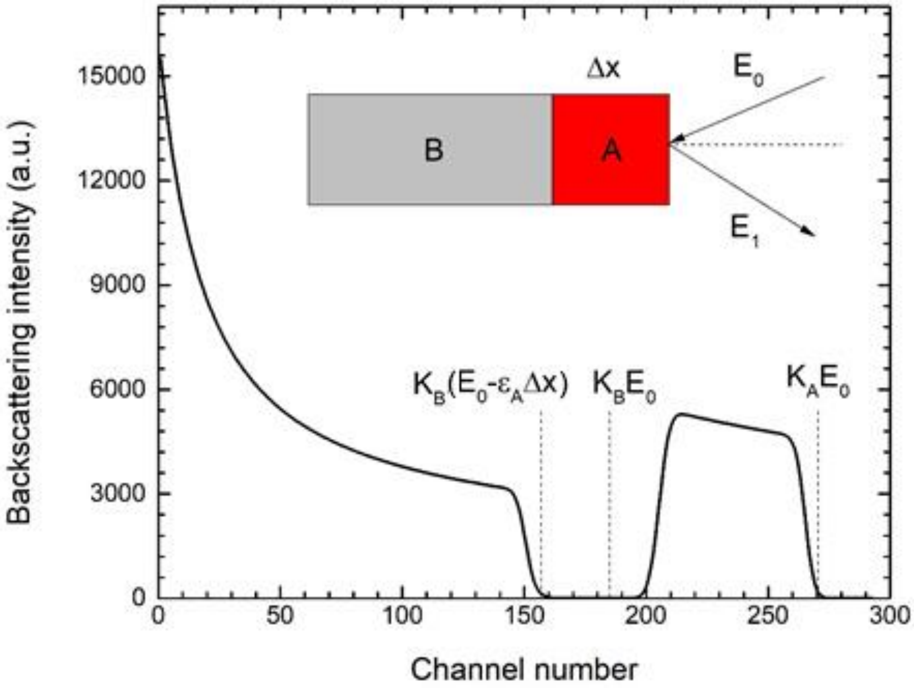

Figure 2.6: An example of an RBS spectra of a film of element A and thickness Δx on substrate of element B. There is a linear relationship between channel number and detected ion energy. Heavier atoms situated at higher energies or channels as determined by their respective kinematic factors.

2.2 Medium energy ion scattering

The principles of medium energy ion scattering (MEIS) are almost identical to that of RBS. The energies involved in MEIS are typically in the range on 50-200 keV. The medium ion energy range is where the electronic energy loss is maximized and therefore the stopping cross sections are maximized for H^+. This implies that the relative energy loses, ΔE, are larger in MEIS compared to RBS, even given the same depth, Δx. Also, recalling the E^{-2} dependence, at these energies the scattering cross sections are significantly larger than typical RBS, which can allow for the detection smaller concentrations of elements. Lastly, given the energy losses involved, incident ions cannot penetrate as deeply into the target as at higher energies, all of which makes this a much more surface sensitive technique useful for determining the composition of ultra-thin films and interfaces.

However, there are a few significant differences which differentiate MEIS from RBS: the use of lower energy incident ions, and the use of a higher resolution toroidal electrostatic analyzer (TEA), with a position sensitive detector, rather than a solid state Si barrier detector. Nonetheless, both involve the interaction between incident ions and the condensed media, which they penetrate. Thus, ions travel through the target and loose energy in the same processes as outlined in Chapter 2.1.3 and upon backscattering, the same kinematic factor in Chapter 2.1.1 applies. However, given the lower energies involved in this technique, the screening corrections to the Rutherford scattering cross sections may be required as described in 2.1.2.

Using a TEA allows one to collect energy spectra (yield vs. energy) over a range of scattering angles, θ, simultaneously at higher resolution ($\Delta E/E < 10^{-3}$). The detector can also be rotated to be aligned in a crystallographic direction of a crystalline substrate. If one considers a sample consisting of some amorphous film on top of a crystal substrate such as Si, it is possible to align the incident ion beam in the same direction as a major crystallographic axis of the crystal substrate, a process known as channeling. This greatly reduces the backscattering yield due to the substrate, which had the potential for obscuring elements lighter than Si. Additionally, the detector can be moved to a position corresponding to a different crystallographic direction. Backscattered ions from the substrate which would have reached the detector are now blocked by the atoms in the crystal’s lattice. This is known as blocking. Channeling and blocking together, are known in IBA, as double alignment geometry.

2.2.1 Channeling and blocking

In many instances the targets of backscattering analysis are amorphous or composed of randomly oriented polycrystalline material. However, there are unique aspects of particle-matter interactions to consider when an energetic ion is incident on the long-range order associated with a crystal. These are known collectively as channeling effects and they arise due to the “steering” of energetic ions by rows and planes of atoms in a coordinated series of small-angle collisions [5]. Channeling effects can substantially reduce the backscattering yield depending on the orientation of the single-crystal target with respect to the axis of the incident beam. The typical applications of channeling in MEIS are to determine the location of impurity atoms in lattice sites, quantifying the degree of lattice disorder, the composition, and thickness of amorphous surface layers and other phenomena reviewed in reference [1].

In Figure 2.7, the MEIS spectrum from channeling geometry where an incident ion beam is aligned with a major crystallographic direction, is compared to a spectrum taken in a random direction. This leads to significant reduction in backscattering intensity corresponding to the Si substrate, by more than two orders of magnitude. The reduction in yield occurs due to the way in which the outermost surface Si atoms shadow the underlying Si atoms.

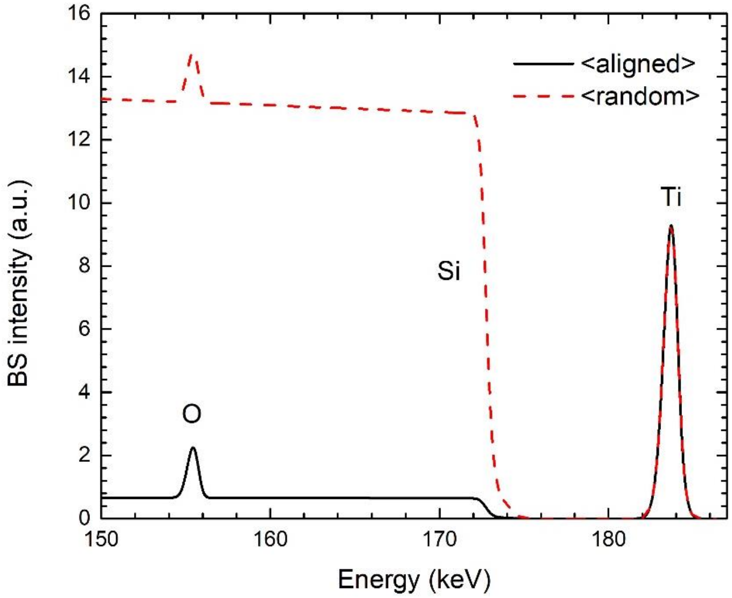

Figure 2.7: The effects of ion channeling on an MEIS spectra for a beam aligned with a direction of crystal symmetry (solid line) and a random direction (dashed line). The spectra represents a TiO_2 film on a Si(100) substrate.

In Figure 2.8a, incident ions after hitting an atom, can be thought of casting a “shadow”. This shadow represents the small-angle deflections of the ions in Coulomb potential due to the nuclear charge [7]. For an unscreened Coulomb potential, the corresponding shadow cone radius is:

$$R_c = 2\sqrt{Z_1 Z_2 e^2 l / E} \tag{2.13}$$

where l is the distance from the atom that was involved in casting the shadow. This simple expression for R_c is derived from the impulse approximation for the bare coulomb interaction.

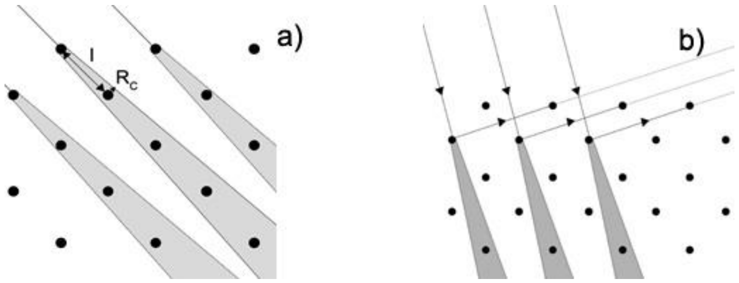

Figure 2.8: The formation of a shadow cone: a) the radius of the cone cast over a neighboring atom, distance *l* away from the surface atom is R_C, b) the effect of simultaneous shadowing and blocking for a (001) surface of an fcc crystal. Adapted from [7].

When backscattering is performed on a single crystal, one can align the incident beam with a major crystal direction. This is depicted in Figure 2.8a which shows an ideal static lattice where only the surface atoms are hit my the incident ions, since the atoms at greater depths are in the shadow cone cast by the surface atoms. In non-ideal circumstances, thermal motion leads to imperfect shadow cones, but the thermal vibrational period (~10^{-12} – 10^{13} s) is longer than the ion transit time through the surface region (~10^{-15} s), so that the crystal atoms can be considered fixed in their thermally displaced locations during the passage of the ion [8]. If the imperfect shadow cones have resulted in an incident ion reaching atoms beneath the surface layer, the backscattered ion, may be blocked from reaching the surface, by another atom, on its trajectory out. In Figure 2.8b the combination of shadowing and blocking is shown for the (001) surface of an fcc crystal.

Many studies routinely implement combinations of channeling and IBA in an effort to characterize lattice disorder or thin-films on crystalline substrates. Recent (2018) examples include: structural damage and channeling effects of c-Si modified by medium-heavy ions [9], lattice stress in ion-implanted compound semiconductors [10], ion irradiation induced intermixing of Fe_3O_4 films on MgO (001) [11], etc.

2.2.2 Sample MEIS spectra

The toroidal electrostatic analyzer (TEA) allows for the simultaneous acquisition of multiple energy spectra over a range of different scattering angles, θ. A 3D MEIS spectra of $Ti^{16}O_2$/ $Ti^{16}O_2$/Ti/Si(001) is shown in Figure 2.9. The colors show the intensity of the backscattering yield as a function of E and θ. Rather than a unique energy assigned to each element, the functional dependence of the kinematic factor, K, on θ, is apparent. As a result, there are elemental "edges" that highlight this dependence and in Figure 2.9 these edges are labeled. The backscattering yield from the Si substrate was minimized by aligning the incident 200 keV H beam with a major Si(001) crystallographic direction, however the Si on the surface is still visible due to the first few monolayers of the Si substrate. The vertical line at $\theta = 135^0$ corresponds to a further reduction is Si intensity due to alignment of the TEA with a <101> blocking direction of the Si substrate. Taking the 2D energy spectra at $\theta = 135^0$ results in Figure 2.10. The horizontal line in Figure 2.9 was chosen to illustrate how the Si scattering yield depends on θ as well and results in Figure 2.11.

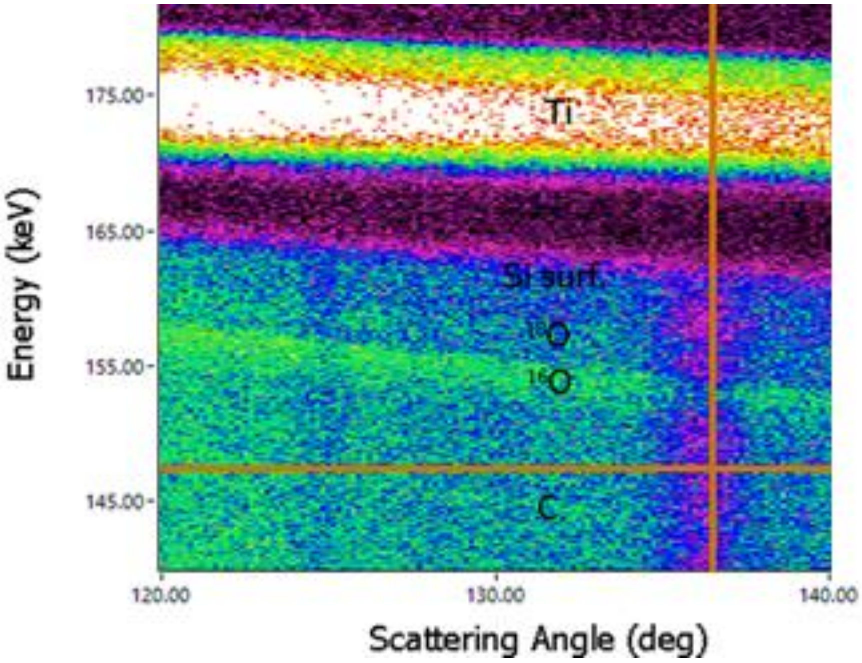

Figure 2.9: MEIS spectra for 200 keV H^+ at an incident angle of 45^0 on a Ti film deposited on Si(001), exposed to $D_2{}^{18}O$, and anodized in $H_2{}^{16}O$ at 1.5 V. The resultant structure is $Ti^{16}O_2$/ $Ti^{18}O_2$/Ti/Si(001). The vertical line at $\theta = 135^0$ corresponds to channeling minima of the Si(001) substrate results in Figure 2.10.The horizontal line was chosen to show how the Si scattering yield depends on θ and results in Figure 2.11.

Figure 2.10 depicts a more typical backscattering energy spectra integrated over a $\pm 1^0$ angular window to improve signal to noise ratio. The O and C peaks are visible despite their lower scattering cross section compared to Si, which would only be possible by reducing the Si signal with channeling. In addition, the cross sectional energy dependence on energy, i.e. E^{-2}, is favourable in this energy range. MEIS is even more sensitive to low-Z elements given the lower energies of the technique.

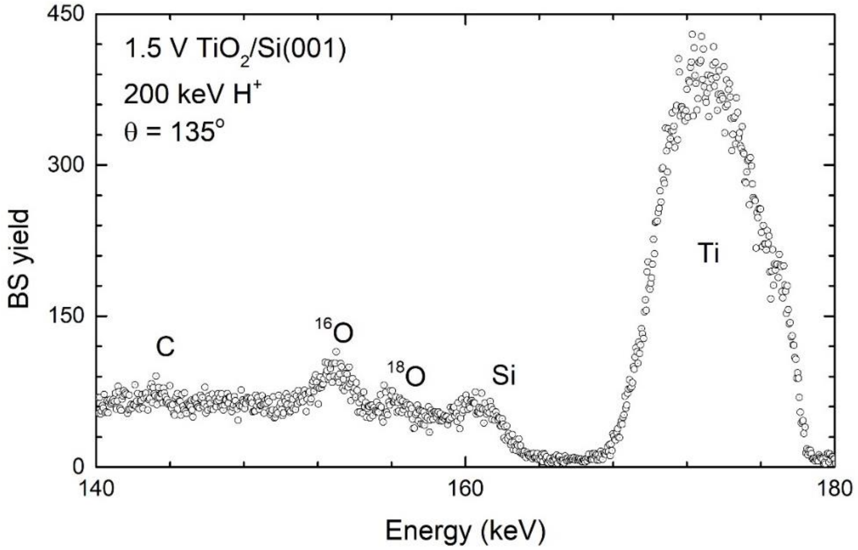

Figure 2.10: A 2D MEIS backscattering spectra at scattering angle of θ = 135^0 for the 3D spectra in Figure 2.2. Positions of the O, Si, C, and Ti peaks are noted.

Figure 2.11 shows an example of the angular yield data taken near the backscattered energy of 147 keV. The shift of the blocking dip for Si from the expected 135° at ideal alignment to <101> scattering direction is due to experimental offset in the sample manipulator position.

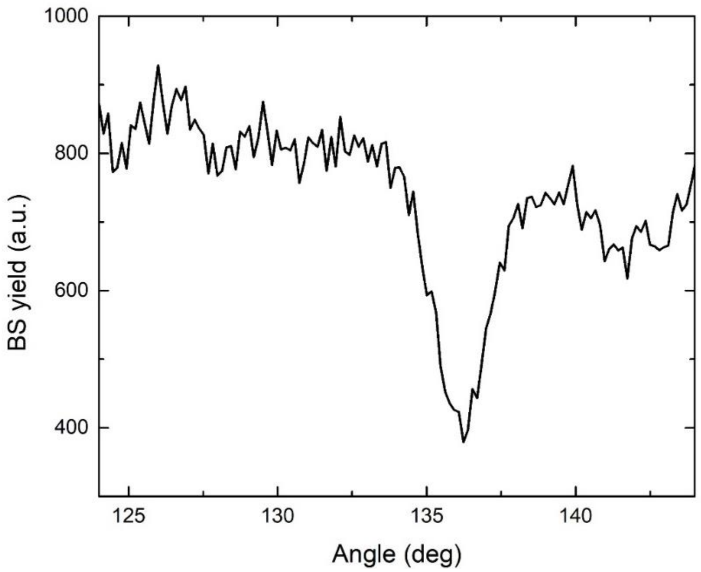

Figure 2.11: 2D spectra, for a single energy, showing the scattering intensity as a function of θ for the target in Figure 2.12. The drop in intensity from the Si signal is apparent around θ = 135^0 which corresponds to a channeling minima along <101> direction and thus a reduction by a factor of two in the Si scattering yield.

2.3 RBS and MEIS instrumentation

The accelerator used to produce H^+ and He^+ ions, for MEIS, RBS, and NRP, is the linear tandem ion-beam accelerator (High Voltage Engineering Europa) at the Tandetron Lab in the University of Western Ontario (Figure 2.12) with a maximum terminal voltage of 1.7 MV.

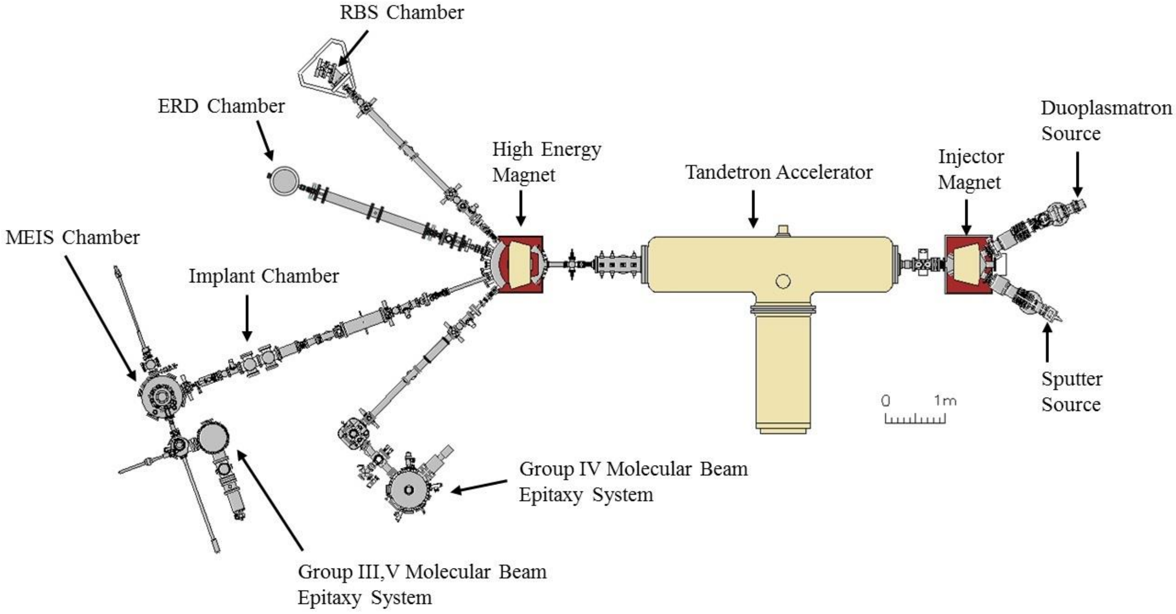

Figure 2.12: 1.7 MeV high-current Tandem accelerator (Tandetron Lab, Western University). Downloaded from [http://www.isw.physics.uwo.ca/facilities/index.shtml] July 28th, 2018.

The He ion beam is formed, in a duoplasmatron source that ionizes He gas, followed by acceleration of the ions in two stages. First, He^+ ions pass through sodium vapour which result in He^- ions. The injected He^- ions are accelerated due to applied electrostatic field created by the high positive voltage applied to the terminal in the middle of the accelerating tube. Here the electrons are stripped from the monovalent He^- through charge exchange processes in a nitrogen stripper cell. The He^+ ions are selected and accelerated towards the ground potential, which represents the second stage of acceleration. The H^- ions are initially created by a cesium (Cs) sputter source with titanium hydride target (TiH_2) before undergoing the same two-stage acceleration process outline above for He ions. For energies lower than 160 keV, H^- are not converted to positive ions and undergo only the first acceleration stage.

An electrostatic quadrupole triplet is positioned at the low-energy end of the accelerator and focuses the ion beam. A high energy switching magnet directs the ion beam at full energy to either the MEIS or RBS (NRP) beamline. The He beam is further collimated by adjustable beam slits resulting in a beam spot on the sample with average dimensions of 0.5×0.5 mm^2. The H beam is collimated by beam slits to about 0.5×1.5 mm^2 at the entrance to the MEIS chamber. The ion dose (μC) is measured by a Faraday cup, which periodically (typically 1 s for every 4 s interval) is moved to block the beam and measure the current associated with the ion beam. A high-precision 4-axis manipulator allows for x, y-translations of the samples in the RBS chamber within ± 0.1 mm. The manipulator also allows for rotation in two angular directions with respect to the ion beam direction within $\pm 0.1^0$. Similarly, a high-precision 6-axis goniometer allows samples in the MEIS chamber to be manipulated with respect to the ion beam within 0.1^0 and ± 0.1 mm by x,y,z-translations and polar (R_1), azimuthal (R_2), and tilt (R_3) rotation axis.

As mentioned in a preceding section, the measurement of the backscattered He ion energy distribution is performed with a surface barrier silicon detector (Ortec). The detector is located at a fixed scattering angle of $\theta = 170^0$ with respect to the axis of the incident beam, known as “Cornell” geometry. The energy resolution of the detector is 12 keV with an aperture of 2.0×6.1 mm^2. Simulated RBS energy distributions where processed using SIMNRA 6.06 [12]. Experimental MEIS energy distributions where compared with simulated spectra using MEISwin v.1.0X [13].

The energy distributions of backscattered H^+ ions are recorded by a toroidal electrostatic analyzer (TEA) (High Voltage Engineering Europa) [14]. The TEA is schematically depicted in Figure 2.13 and can rotate around the z-axis of the target sample and simultaneously collects ions over a $\pm 10^0$ range of scattering angles around its bisector. The TEA has two concentric plates biased at a potential V and causees the ions to travel in toroidal trajectories towards the plates. This serves to select for a central pass energy, E_c, of backscattered ions. Ions with too low or too high energy, 0.01949Ec, will fail to reach the exit slit and will not be detected. This can be calculated as $E_c=V/0.06$, where $\pm V$ are the voltages (in kV) applied to the plates of the TEA. For a 95 keV beam, the energy window is 1.85 keV, the applied voltages to the TEA are ± 5.6 keV. The ions that reach the exit slit will then pass through two microchannel plates with a total gain of 10^7. The resultant current is collected by position sensitive change-dividing collector. Given that the highest voltage possible for the TEA is 10 kV, this detector is best suited for the detection of energies from 1-170 keV (lower than the typical RBS range) and is well suited for medium energies found in MEIS.

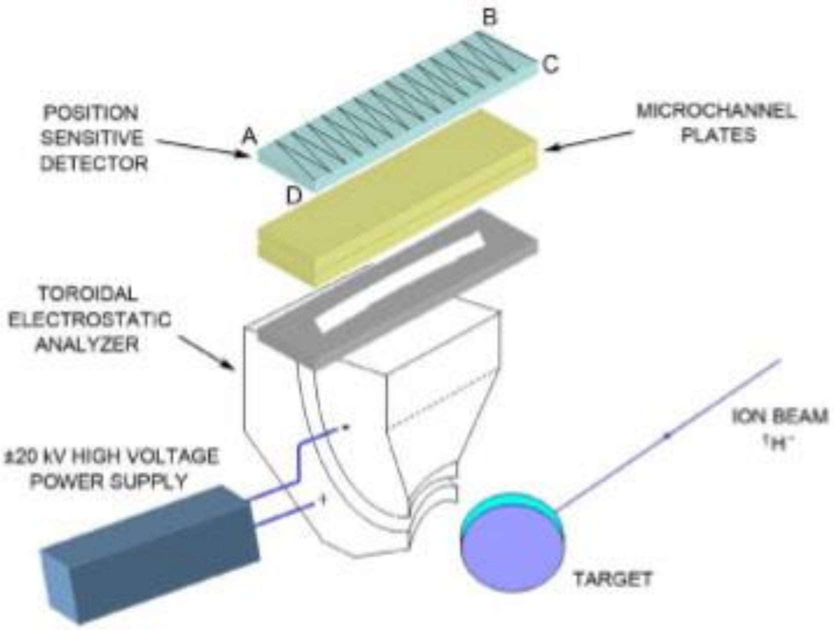

Figure 2.13: A schematic of the toroidal electrostatic analyser as used in MEIS data acquisition [14].

The TEA design is limited to the collection of charged spcies only at the expense of neutrals. The expression that governs the yield of the MEIS spectra is thus:

$$Y = \eta^{\pm}\, \sigma\, \Delta\Omega\, Q\, N\Delta t \tag{2.14}$$

where $\eta^{\pm}$ is the fraction of negative or positive ions produced by backscattering of the incident ions. For medium ion range, the $\eta^{\pm}$ is independent of depth, incident angles, and scattering angles. Use of a silicon barrier detector simultaneously with a TEA allows the ion fraction to be measured [15]. Since the silicon barrier detector measures both neutrals and ions, and the TEA only measures ions, the difference between the yields gives insight into the ion fraction, provided the different solid angles and scattering angles are taken into account. The typical fraction η^{+} for positive ions is in the 0.6 – 0.75 range.

Control of the angular position of the sample and the collection of MEIS spectra are performed with software developed in LabView. Automatic corrections to image distortion and proton charge distribution calculations have been discussed in detail previously [15]. MEIS image resolution is limited by the energy distribution of the incident ion beam, the slits that define the beam, and the resolution of the TEA and is estimated to be 215 eV for 95 keV H^-.

2.4 Nuclear reaction analysis

Previously described ion beam techniques all involve ion-solid interactions that are governed by classical scattering laws. The techniques in this section involve the use of radioactive decay, induced through projectile-nucleus interactions. Only so called “prompt radiation analysis” will be considered, where the radiation is emitted instantaneously from a projectile-nucleus interaction, i.e. within times less than 10^{-12} s [1]. The nuclear reactions described here are non-

Rutherford and the cross sections of which are derived from considerations of the strong nuclear force [4], which governs nuclear fission and fusion. A complete description of the process involves quantum mechanics of the nucleus whose details are beyond the scope of this chapter.

A given incident ion will need to have sufficient energy to overcome the Coulomb barrier to reach the attractive nuclear regime of a nucleus [1]. The energetic barrier to overcome such that the distance of closest approach would have the two nuclei in close proximity as:

$$E_b = \frac{Z_1 Z_2 (m_1 + m_2)}{m_2 (A_1^{1/3} + A_2^{1/3})} \tag{2.15}$$

where $Z_{1,2}$ is the atomic number, $A_{1,2}$ the atomic mass, and m the mass of the nucleus of the incident particle and target nucleus. Given quantum tunneling effects, the incident ion could be in the attractive regime even if $E < E_b$.

A common way to represent nuclear reactions is of the form:

$$a + X = b + Y \tag{2.16}$$

where $(a+X)$ are the reactants and $(b+Y)$ are the products. All reactions require that the sum of the atomic numbers and the sum of the mass numbers of the products and reactants be equal. Another way to express the same reaction is as $X(a,b)Y$. A full description of the nucleus is expressed as ${}^{A}_{Z}X$, where A is interpreted as the number of nucleons and Z is the number of protons. For incident energies commonly found in ion beam analysis (0.1-5 MeV) the Coulomb repulsion is most easily overcome with a low-Z (1,2) ion incident on a low-Z (Z=1-15) target nucleus [6].

Given that RBS is not sensitive to low-Z elements on a heavy substrate, as the scattering cross sections are proportional *to* $Z,^2$ NRA is often seen as a complementary technique to detect and to quantify light elements. Given that the nuclear reaction involved is isotope specific and there is no background signal from other elements (especially high *Z* ones) makes NRA ideal for isotopic tracing studies.

2.4.1 Nuclear cross section

The probability of a reaction between incident ion and target nucleus is approximated as the geometrical cross section of that target nucleus and the incident ion is assumed to be a point mass. Most cross sections are on the order of a 10^{-24} cm^2 = 1 barn. Often the cross sections vary in complicated ways depending on incident particle energy and detection angle and for most reactions there is no analytical form and so there is a complete dependence on published data of measured cross sections in the energy range and angles of interest [6]. Figure 2.14 depicts experimental data for a large range of energetic (0.5 – 1.0 MeV) for the $^{18}O(p,\alpha)^{15}N$ reaction. It highlights the complicated way in which cross section can change as a function of H^+ ion energy. The resonance most relevant to the present work is at 151 keV with a width of Γ ~0.05 keV, and isotropic in the vicinity of the resonance [4]. The energy of the emitted α particles is between 3 – 4 MeV but depends on incident proton energy.

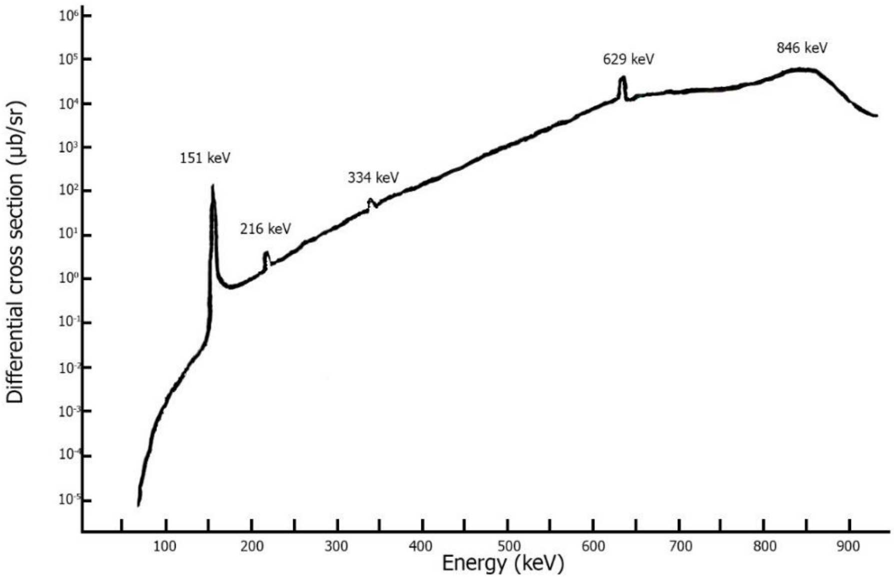

Figure 2.14: The nuclear cross section for $^{18}O(p,\alpha)^{15}N$ as a function of proton energy. Adapted from [16].

2.4.2 Geometry and experimental implementation

The equipment required for NRA is very similar to that of RBS. One requires a particle accelerator, UHV, surface barrier detector, multi-channel analyzer (MCA), scattering chamber, etc. The geometry in NRA is the same as in RBS and can either be in the forwards to backwards direction and is depicted in Figure 2.15.

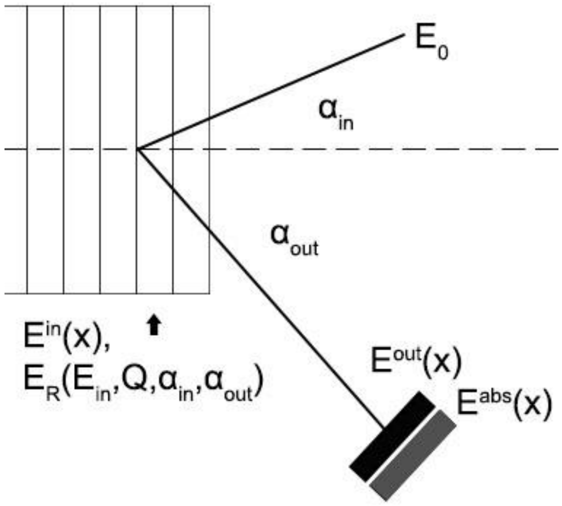

Figure 2.15: Geometry of a typical NRA experiment: α_{in} and α_{out} are the incident and detector angles, E_0 is the incident beam energy, $E_{in}(x)$ is the energy of the ions upon reaching depth *x*, $E_R[E_{in}(x),Q,\alpha_{in},\alpha_{out}]$ is the energy of the reaction product produced at depth *x*, $E_{out}(x)$ is the reaction product produced at depth *x* that have traveled out of the sample and to the absorber, $E_{abs}(x)$ is the energy of the reaction product after it passes through the mylar or aluminum absorber and reaches the detector. Adapted from [4].

The primary difference between RBS and NRA is that the Rutherford cross sections that define backscattering are much larger in RBS and so it is necessary to prevent the detector and electronics from being overloaded with the elastically scattered primary beam [6]. The flux is filtered usually with a pin-hole free mylar or aluminium absorber foil that is placed in front of the detector [4]. The energy of the particles after passing through the foil is thus given by:

$$E_{abs} = E_{out}(x) - \int_{0}^{x_{abs}} S_{abs}(E)dx \tag{2.17}$$

where x_{abs} and $S_{abs}(x)$ are the thickness and stopping power of the absorber foil respectively.

The yield of emitted particles depends on the reaction cross section but as started above there are no simple analytical expressions for it and we must rely on experimental values. If the cross section is known, the measured reaction product yield is proportional to the areal density of nuclei:

$$A = Q_C \Omega \sigma(E_0)(Nt)/cos\alpha_{in} \tag{2.18}$$

where in this context A is the integrated counts in the area of the peak and Q_c is the collected charge, Ω is the solid angle and *(Nt)* is the areal density.

Since it is often difficult in practice to know the exact Ω and $\sigma(E_0)$, the use of a standard (e.g. $Ta_2{}^{18}O_2$) with a well-known areal density of the isotope of interest can allow us to quantify our sample's areal density. By measuring the in integrated intensity for both the sample and taking the ratio we get Equation 2.19:

$$\frac{A}{A_{sd}} = \frac{Nt}{(Nt)_{sd}} \tag{2.19}$$

The depth scale is related to the energy loss of the incident ions as they penetrate the sample prior to the nuclear reaction, by using the stopping powers for the target sample, S_{in}:

$$\Delta x = \Delta E / S_{in} \tag{2.20}$$

The uses of Equation 2.20 will be discussed in the next section in the context of depth profiling.

2.4.3 ^{18}O depth profiling

In this work, the $^{18}O(p,\alpha)^{15}N$ resonance was used to quantify the ^{18}O areal density in ultra-thin films as a function of depth. The reaction is depicted in Figure 2.16 a), where H^+ nuclei are bombarded by H^+ at 151 keV and produce a reaction that results in ^{15}N and the emission of a α particle. This particular resonance is useful because it has a very narrow width (0.05 keV) and slight deviations from that energy in either direction result in the differential cross section falling off by close to three orders of magnitude, leading to a high depth resolution. Thus, as in Figure 2.16 b), if there is ^{18}O on the outermost surface of a sample and it is bombarded with 151 keV H^+, one will get emission that corresponds to the outermost surface only.

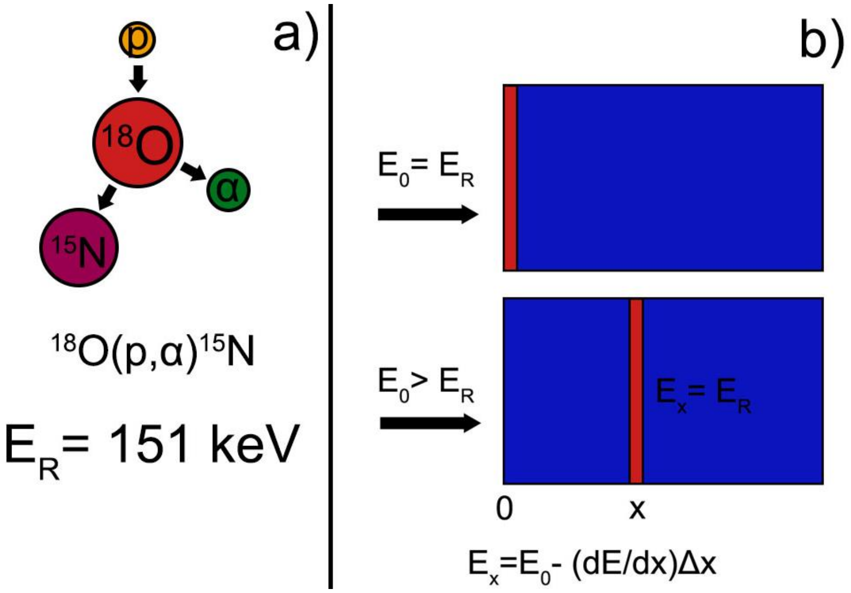

Figure 2.16: a) A schematic representing the $^{18}O(p,\alpha)^{15}N$ reaction used in this work, b) schematic showing how profiling is done with the resonance.

By incrementally increasing the energy of the beam, one will move away from the resonance at the surface and the ions will lose energy as they propagate through the medium, given the stopping powers defined in previous sections. They will continue to lose energy until they reach the 151 keV and provided there is ^{18}O at this depth, α emission will occur from the current depth the ions have penetrated. The integrated α intensity at each energy increment is then related to ^{18}O through the use of a well quantified standard using Equation 2.19 and the energy corresponding to that areal density is converted to a depth scale using Equation 2.20. In Figure 2.17 a), the α distribution for two different depths into an oxide layer on Ti that contains ^{18}O is shown (96 Å vs 53 Å), the difference in integrated intensity is a linear function of the areal density of ^{18}O at that depth (or energy). By incrementing from the resonance energy at the surface of the sample, through the entirety of the sample, the α integrated intensity can be converted to ^{18}O areal density.

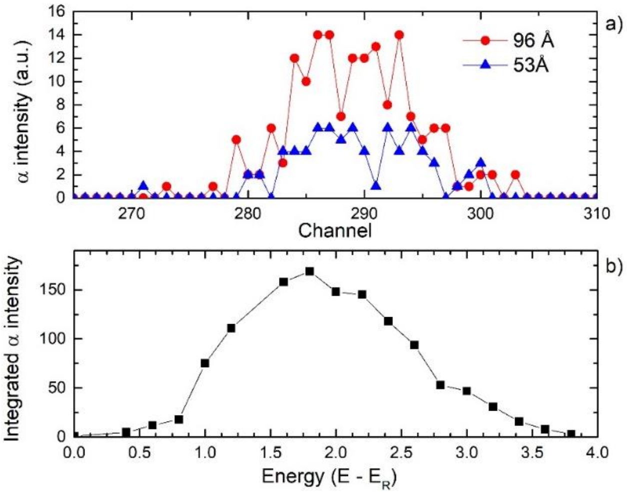

Figure 2.17: a) The measured alpha intensity as for two depths where the difference in integrated intensity is due to different areal densities ^{18}O at these depths. b) The integrated α as a function of energy relative to the resonance energy.

NRA is a mature IBA technique yet it continuities to be widely used, often as a complementary technique to RBS and related techniques. As mentioned earlier, it is especially useful to quantify low-Z elements that most RBS and MEIS are insensitive too, and detect low concentrations of elements, which would have been obscured by signals from the bulk elements, as is common in IBA. Recent examples of NRA being used in the past few years include: the $^{18}O(p,\alpha)^{15}N$ resonance has been used to quantify oxygen oxides [17], a $^{7}Li(p,\alpha)^{4}He$ reaction was used to quantify Li at ppm in geological samples [18], $^{16}O(d,p)^{17}O$, $^{18}O(p,\alpha)^{15}N$, and, $^{2}H(d,p)^{3}H$ reactions help characterize TiO_2 nanopowders [19], the $^{14}N(\alpha,p_0)^{17}O$ resonance being used to depth profile titanium nitride thin films on steel [20], etc.

2.5 X-Ray photoelectron spectroscopy

X-ray photoelectron spectroscopy (XPS) is a technique where a sample is irradiated with mono-energetic X-rays leading to the emission of electrons via ionization of core shell electrons. The electrons are collected and analyzed as a function of their kinetic energy. This allows for determination of the binding energy of each electron. Since the core shell energy is unique to each element, XPS is widely used for its ability to identify and quantify the elemental composition within the first 10 nm or less of any solid surface, with a sensitivity to most elements from Li- U, provided they are in concentration > 0.05 atomic % [8]. He and H are undetectable due to their extremely small photoelectron cross section. The chemical environment of an element leads to shifts in core shell electron binding energy which allows XPS to determine the speciation of the respective elements that compose a sample.

The binding energy of each core shell can be determined by the conservation of energy [21]:

$$E_B = (h\nu) - E_k - \varphi_s \tag{2.21}$$

where $h\nu$ is the energy of the incident photon, E_k is the measured kinetic energy of the photoelectron after emission, and φ_s is the work function of the spectrometer. The process of photoemission occurs as a single step and the photon energy is completely transferred to the photoelectron in the form of kinetic energy, as shown in Figure 2.18.

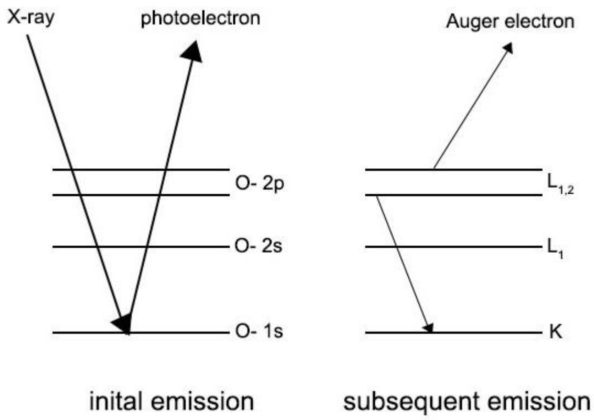

Figure 2.18: The photoelectron process (on the left) with the electronic energy levels are depicted in spectroscopic notation and the subsequent Auger de-excitation process (on right) with energy levels written in X-ray notation. Adapted from [8].

Peaks of the XPS spectra correspond to the binding energies of atomic core levels. The energy of a given electronic state can be completely classified by their given set of quantum numbers [2]: the principle quantum number (n = 1, 2, ...) which defines the energy and spatial distribution of the electron around the nucleus. The shape of the spatial distribution of the electron is determined by the orbital angular momentum quantum number ($l = 0, 1, \ldots, n-1$). The magnetic quantum number ($m_l = -l, -l + 1, \ldots, 0, \ldots, l - 1, l$) defines the orientation of an electron's spatial distribution. From the Pauli Exclusion Principle, each level can only contain two electrons which must have opposite spins, thus the spin quantum number ($m_s = \pm 1/2$) denotes the spin state of a given electron. For example, the difference in E_B can be detected with XPS between an electron with the configuration ($n = 2, l = 1, m_s = ½$) and another with the configuration ($n = 2, l = 1, m_s = -½$). These two levels are called $2p_{1/2}$ and $2p_{3/2}$.

The fine structure of electrons with the same n but nonzero l quantum numbers arises from an effect known as spin orbit coupling [8].. For a given, l, there are two possibilities for j since m_s

= ±1/2. The degeneracy defined as the number of electrons given a particular value of *j*. For a 2p orbital (n = 2, l = 0,1) there can be three values of m_l = (-1,0,1). Working out each possible combination of results of *n*, *l*, and m_l results in six combinations results in $j = |1/2|$ and three combinations that result in j = |3/2|. This is why in Table 2.1, the ratio of the area in an XPS spectra that corresponds to these features is 1/2, i.e. in addition to there being an energy shift between these features, there is also a difference in peak intensity.

Table 2.1: Spin orbit coupling for electronics in p, d, and f orbits.

Orbital	***l***	m_s	$j = l + m_s$	**Area ratio**
p	1	±1/2	3/2, 1/2	1:2
d	2	±1/2	5/2, 3/2	2:3
f	3	±1/2	7/2, 5/2	3:4

Figure 2.19 shows the low-resolution spectrum collected with a monochromatic Al Kα source incident on a 10 nm titanium dioxide film grown via anodization in water of Ti deposited on Si(001) substrate. The takeoff angle of the outgoing electron with respect to the surface is 90^0. The evident spectral lines correspond to photoemission from Ti 2p, Ti 3s, Ti 3p, O 1s, and C 1 energy levels as well as Auger electron emissions resulting from filling the O 1s core hole (K level) and the filling of the Ti 2s core hole (L level).

The binding energy of the photoelectron is highly dependent on the chemical environment it is found in. Differences in oxidation state, i.e. the presence of chemical bonds (in addition to other factors such as placement in lattice site) can lead to what is known as “chemical shifts” in the expected energy. This is evident in Figure 2.19 b) & c) which show the high resolution XPS spectra of the C 1s and O 1s orbitals and how the binding energy is modified depending on the chemical context that these elements are found.

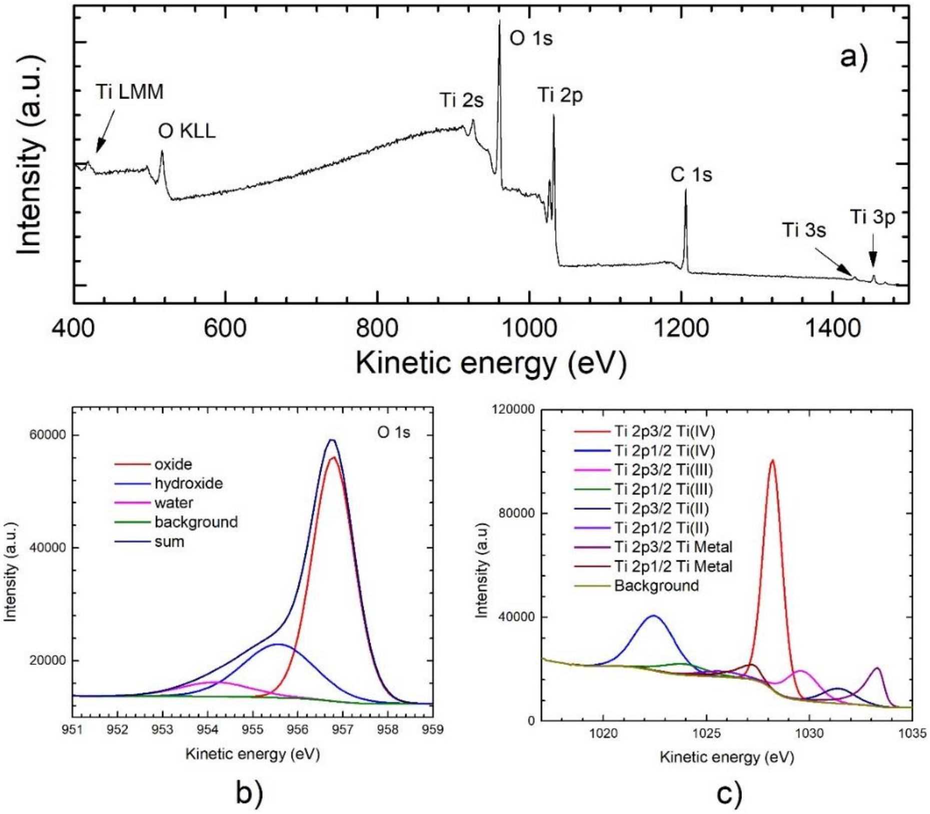

Figure 2.19: a) A low resolution XPS spectra analyzed using a monochromatic Al Kα source, showing spectral features for Ti oxide formed via anodization in water. The Ti LMM and O KLL are designations of Auger electron peaks, the rest of the peaks are due to photoelectron emission, b) and c) Represents the high resolution XPS spectra of the O 1s and Ti 2p features respectively, in more detail, and the effect of chemical environment on the binding energy is apparent. Note that, lower binding energies result in high kinetic energy of photoelectrons.

Figure 2.19c shows the Ti XPS photoemission from 2p electronic states with nonzero angular momentum which results in spin-orbit doublet due to the spin-orbit interactions between unpaired electrons in the atom.

XPS has a very high surface sensitivity due to the short inelastic mean free path, λ of photoelectrons in matter. Photoelectrons interact inelastically with core or valence electrons in the medium, the density of which is essentially universal (at about .25 electrons/ $Å^3$) and as such there is little variation between mediums [22]. Thus, electrons that provide useful information, which make it to the detector with some appreciable kinetic energy must have come from near to the surface. The intensity of photoelectrons attenuates exponentially and 95 % of the intensity comes from the sampling depth defined as 3λ. As seen in Figure 2.19a, the photoelectrons from the sampling depth are responsible for the sharp elemental peaks, while those from greater depths will lead to a bulk intensity that provides little information due to significant inelastic energy loss.

The function of XPS primary use in the context of these investigations is in determination of formal oxidation states and was chosen to complement the ion beam based techniques as outlined in previous sections. RBS, MEIS, and NRA are capable of providing elemental areal density as a function of depth but give no insight into the chemical environment (i.e. bonding) throughout these films.

2.6 Experimental implementation of electrochemistry

In many electrochemical contexts such as anodization, control of the potential at the WE is desired. The two-electrode configuration in Figure 1.1, makes it very difficult in practise, to maintain a constant potential between the CE and WE, since fluctuations in the current with time will can cause drastic is the apparent potential, i.e. Ohm's law may not apply [23].

A potentiostat is a commonly used instrument in electrochemistry, and is used to reliably control the interfacial potential of the WE in the cell, relying on feedback to maintain cell potential even in the presence of changes in impedance during the measurement. As shown in Figure 2.20, this typically involves a three-electrode configuration, and has two functions: to maintain a fixed potential between the WE and the RE, and to measure the current from the WE. The RE should maintain a constant potential over all conditions, while a third electrode called the CE, functions to conduct current into or out of the cell and to balance the current generated at the WE.

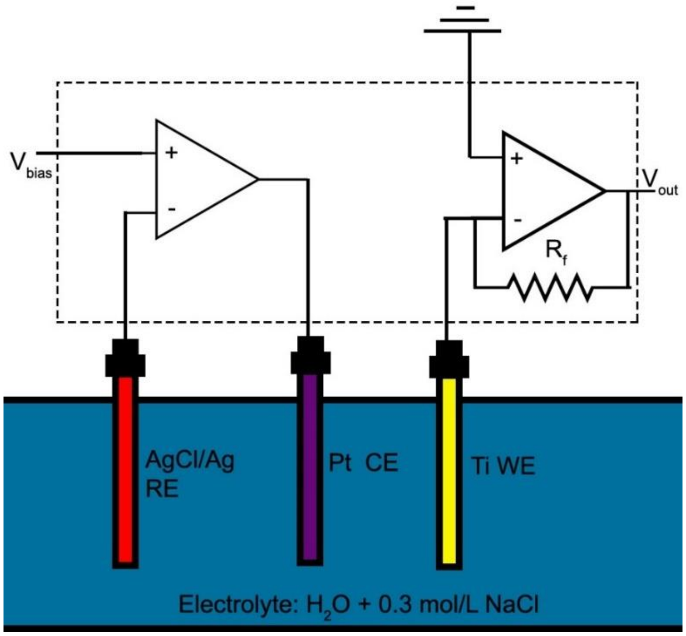

Figure 2.20: A schematic of a basic potentiostat circuit involving three electrodes: a Ti working electrode (WE), Pt counter electrode (CE), and AgCl/Ag reference electrode (RE).

Figure 2.20 shows a basic potentiostat circuit, which contains two operational amplifiers (op amps), with distinct functions. An op amp has two input terminals and one output terminal.

The (-) terminal is called the inverting input and the (+) terminal is known as the noninverting input. The output voltage is determined by the expression [24]:

$$V_0 = A(V_+ - V_-) \tag{2.22}$$

where A is the gain factor, V_+ is the noninverting input voltage, and V_- is the inverting input voltage.

The op amp on the left hand side of Figure 2.20 results in potentiostatic conditions, which is achieved by connecting the inverting input directly from the RE. If the RE produces a voltage that is higher than V_{bias}, according to Equation 2.22, the op amp output voltages will decrease and in turn, will drive less current though the cell, and the electrolyte voltage decrease. If the RE produces a voltage lower than V_{bias}, the op amp output voltage increases which increase the voltage of the electrolyte.

The current to voltage converter circuit is on the right side of Figure 2.20. The resistor R_f is placed in negative feedback loop of the op amp, who's inverting input is connected to the WE, and the non-inverting input connected to ground. A property of op amps is that no current flows into or out of the inputs. So, if current flows from the WE into the op amp, it cannot enter the op amps and rather it has to pass through R_f (according to Kirchhoff's current law). Thus, when current flows through the WE, it induces a voltage drop across R_f (by Ohm's law), which is measured across the resistor. The output voltage V_{out} balances the voltage drop across R_f and therefore V_{out} is exactly proportional to the current, with the proportionally factor being the R_f.

The AgCl/Ag RE is a commonly used for electrochemical measurements, and is the RE shown in Figure 2.20. In the cell it functions as a redox electrode. The equilibrium is between the Ag metal and the AgCl. These two half reactions written together result in:

$$AgCl_{(S)} \rightleftharpoons Ag^{+}_{(aq)} + Cl^{-}_{(aq)} \tag{2.23}$$

The standard electrode potential of the AgCl RE is $E^0 \approx 0.23$ V against the standard hydrogen electrode (SHE) [25].

2.7 Molecular beam epitaxy

Molecular beam epitaxy (MBE) is a versatile technique for growing thin epitaxial structures made from metals, semiconductors, or insulators [26]. MBE is classified as a physical deposition technique, in contrast with chemical deposition (CVD, etc.), where elements are vaporized from polycrystalline or amorphous sources at high local temperatures and are transported through a vacuum reactor toward the substrate without any chemical change. The basis of this technique is the crystallization of thin films via reactions between thermal beams of molecular or atomic species and a substrate surface in UHV ($P < 1.33\times10^{-7}$ Pa (10^{-9} torr) [27]), resulting in a high purity solid. The composition of the epilayer and its doping level depend strongly on the evaporation rates of the sources. The growth rates of the technique are typically 1 μm/h (1 monolayer/s) which is sufficiently slow to facilitate the surface migration of the incident species on the growing surface and as a consequence, the surface of the growing film is very uniform [26].

MBE growth does not occur in thermodynamic equilibrium and so growth proceeds by kinetics of surface processes that occur when the beam reacts with the outermost layer of the substrate crystal. A large number of surface processes are relevant to MBE film growth but the most important are [28]: i) the adsorption of the constituent atoms incident on the substrate surface, ii) surface migration and dissociation of the adsorbed molecules, iii) incorporation of the atoms into the crystal lattice of the substrate or the pre-existing epilayer, iv) thermal desorption of species not incorporated in the crystal lattice.

Consideration of multiple surface processes result in three types of crystal growth that can be distinguished from each other (depicted in Figure 2.21): island growth, layer-by-layer growth, and layer plus island growth [29]. Volmer-Weber or Island growth occurs when small clusters of atoms are nucleated on the substrate surface and then proceed to grow into 3D islands of condensed phase. This occurs when atoms bind to each other more strongly than to the substrate and is commonly associated with growing metals on insulators. In Frank-van der Merwe mode or layer-by layer growth, atoms that bound strongly to the substrate less than each other, condensed to form a complete monolayer on the substrate surface and subsequent layers form on top. This growth mode is associated with semiconductor growth on semiconductors and some metal-metal systems. Lastly, Stranski-Karastanov or layer plus island growth, is an intermediate cases. After the first monolayer is formed, the later layer growth is unfavourable and 3D islands are formed on top.

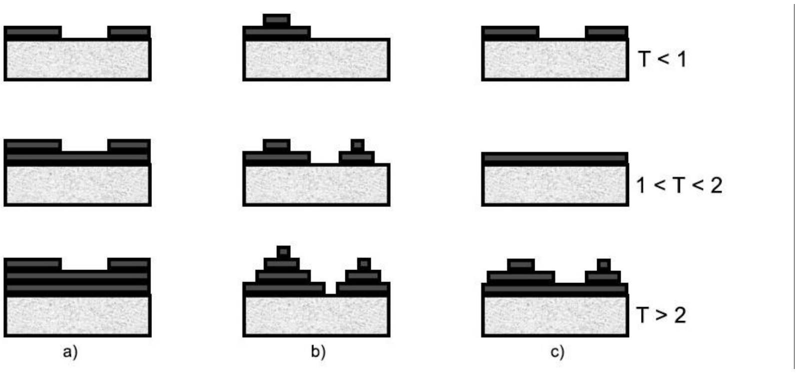

Figure 2.21: Schematic representation of the three growth modes that can result from MBE; a) layer-by-layer, b) island, and c) layer plus island

The MBE system used in the present work utilized electron beam evaporation sources. High purity Ti and Si ingots were heated by a high energy focused electron beam (E ~ 10kV) which results in high purity emission of vapour. An ultra-high vacuum ($P < 10^{-8}$ Torr) is maintained throughout deposition which leads to a reduction in scattering between vaporized species and residual gas atoms and also prevents these gas atoms from reacting with the growing film or film substrate. Evaporated material was collimated using apertures, with a radius of ~ 1.5 cm, towards the substrate as well as a quartz crystal monitor which monitors deposition rates. Shutters can be positioned in front of the aperture to quickly terminate deposition and control film thickness. Room temperature depositions of Ti and Si onto Si(001) substrates were performed, and these films will be discussed further in the following chapter.

2.8 References

1. M. Nastasi, J.W. Mayer, and Y. Wang, *Ion Beam Analysis fundamentals and applications*. 2014: Taylor & Francis Group.
2. J. Vikerman and I. Gilmore, *Surface Analysis The principle Techniques*. 2009: John Wiley and Sons.
3. S. Gotoh and Z. Takagi, *Silicon Surface Barrier Detector* Journal of nuclear science and technology, 1964. **8**: p. 311.

4. J. Tesmer and M. Nastasi, *Handbook of Modern Ion Beam Analysis, 2nd edition*. 1995: Materials Research Society.
5. W.K. Chu, J.W. Mayer, and M.A. Nicolet, *Backscattering Spectrometry*. 1978: Academic Press, Inc.
6. Y. Wang and M. Nastasi, *Handbook of modern Ion beam materials analysis* 2009: Materials Reserch Scoiety.
7. J.F.V.d. Veen, *Ion beam crystallography of surfaces and interfaces.* Surf. Sci. Rep. , 1985. **5**: p. 199.
8. P.V.D. Heide, *X-ray photoelectro spectroscopy an introduction to principles and practices* 2012: John Wiley & Sons.
9. R. Mikšová, et al., *Structural damage and ion-channelling effects in a single-crystal Si layer modified by medium-heavy ions.* Surface and Interface Analysis, 2018. **0**: p. 0.
10. A. Turos, et al., *Ion Beam Modification of ZnO Epilayers: Sequential Processing.* physica status solidi (a), 2017. **0**(0): p. 1700887.
11. M. Krupska, et al., *1 MeV Ar+ and Kr+ ion irradiation induced intermixing in single- and bi-layer Fe3O4 films grown on MgO(001) single crystals.* Surface and Coatings Technology, 2018. **29**: p. 1.
12. M. Mayer, *SIMNRA 6.06*. 1997.
13. T. Nishimura, *MEISwin v. 1.0X* 2015.
14. R. M. Tromp, et al., Review of Scientific Instruments 1991. **62**: p. 2679.
15. J. Kim, et al., *Depth profiling of ultrathin films using medium energy ion scattering.* Curr. Appl. Phys., 2003. **3**: p. 45.
16. H. Lorenz-Wirzba, et al., *The 18O(p, α)15N reaction at stellar energies.* Nuclear Physics A, 1979. **313**: p. 346.
17. S. Kumar, et al., *Oxygen determination in materials by 18O(p,αγ)15N nuclear reaction.* Nuclear Instruments and Methods in Physics Research Section B: Beam Interactions with Materials and Atoms, 2016. **378**: p. 38.
18. N. De La Rosa, et al., *Quantification of lithium at ppm level in geological samples using nuclear reaction analysis.* Journal of Radioanalytical and Nuclear Chemistry, 2018. **317**(1): p. 253.
19. V.B. Vykhodets, et al., *Direct observation of tunable surface structure and reactivity in* TiO_2 *nanopowders.* Surface Science, 2017. **665**: p. 10.
20. M.S. Rihawy, B. Abdallah, and M. Ahmad, *Depth profiling of titanium nitride thin films deposited on stainless steel utilizing combined EBS and NRA techniques.* Nuclear Instruments and Methods in Physics Research Section B: Beam Interactions with Materials and Atoms, 2018. **430**: p. 64.
21. D. Briggs and M.P. Seah, *Practical Surface Analysis 2nd Edition, Vol. 1 Auger and X-ray Photoelectron Spectroscopy*. 1990: John Wiley and Sons.
22. A. Zangwill, *Physics at Surfaces*. 1988: Cambridge University Press.
23. M.D.M. Dryden and A.R. Wheeler, *DStat: A Versatile, Open-Source Potentiostat for Electroanalysis and Integration.* PLOS ONE, 2015. **10**: p. 1.
24. J. Huijsing, *Operational Amplifiers Theory and Design*, ed. Springer. 2011.
25. D.R. White, *Standard potential of the silver-silver chloride electrode and mean activity coefficient of hydrochloric acid in 10 wt% sucrose/water from 0 to 25°C.* Food Chemistry, 1990. **37**: p. 1.

26. M.A. Herman and H. Sitter, *Molecular beam epitaxy fundamentals and current status*. 1996: Springer.
27. L.I. Maissel and R. Glang, *Handbook of Thin Film Technology*. 1970: McGraw Hill.
28. M.A. Herman, *Semiconducting superlattices* 1986: Akademie-Verlag.
29. J.A. Venables, G.D.T. Spiller, and M. Hanbuecken, *A model for the growth shape of crystallites on surfaces.* Rep. Prog. Physics, 1984. **47**: p. 399.

Chapter 3: Stopping cross sections of protons in Ti, TiO_2 and Si using medium energy ion scattering

3.1 Introduction

Understanding the energy loss of ions as they pass through a target medium, is fundamental to the methods of ion beam analysis (IBA). Stopping powers, *S*, and stopping cross sections (SCS), *ε,* are the related quantities which describe this energy loss. They are defined as $S = \frac{\Delta E}{\Delta x}$ and $\varepsilon = \frac{\Delta E}{N\Delta x}$ respectively (with typical units of eV/cm and eVcm^2/10^{15}atoms), where ΔE is ion's energy loss along path-length Δx and *N* is number of atoms per unit volume. Kinetic energy loss of an ion happens through ionization and excitation of the target atom's electrons (electronic energy loss) and through collisions with atomic nuclei (nuclear energy loss) [1]. The latter dominates for low ion energies (E<10 keV/amu), while the former, at higher energies. It is widely accepted [2-4] that incoming ions with E>10 keV/amu are insensitive to the modifications of electronic density due to chemical bonding in chemical compounds. This was first observed by Bragg [5] in 1905 who studied the stopping of alpha particles in a number of compound targets. According to Bragg's rule, for a two-element compound, A_nB_m, the stopping cross section, $\varepsilon(A_nB_m)$, is given by a sum of stopping cross-sections of individual elements taken with stoichiometric coefficients:

$$\varepsilon(A_nB_m) = n\varepsilon(A) + m\varepsilon(B) \tag{3.1}$$

Deviations from this rule were only observed in organic compounds [6-11], in oxides [12-17] and compounds containing at least one element that is a gas in its elemental form [13, 18]. In the latter case, this apparent differences in SCS is called a physical effect. Which is to be contrasted with chemical effects, i.e. deviations from Bragg's rule due to changes in valance electron density, i.e.

---

*The content of this chapter has been published in The European Physical Journal D, 2016,70:248

chemical bonding, in the chemical compound. According to Ziegler [19], physical effects can be incorporated into Bragg's rule if different SCSs are used for the gaseous element when it's a part of the solid compound. Comprehensive reviews of Bragg's rule as it applies to organic and inorganic compounds have been carried out [2, 6, 7, 20]. Experimentally determined SCSs of single elements are extensive [21] compared to the SCSs for compounds, of which relatively few studies have been done.

Recently SCSs of $SrTiO_3$ for 50-170 keV H^+ were measured in our group and deviation of >10% was found in the entire energy region [22]. The question remained as to whether: i) a physical effect is present and the O stopping power has to be modified, ii) a chemical effect is present and Bragg's rule does not apply, or (iii) Sr stopping power is incorrect. In this work, to account for the deviation from Bragg's rule in $SrTiO_3$, we measured SCSs of Si, Ti, and TiO_2 on Si. Our studies indicate that the most probable reason for deviation is a physical effect in the SCS of O used.

IBA relies heavily on the known SCSs of ions for determination of elemental depth profiles and to estimate mass and depth resolution [23]. Potential empirical corrections to commonly used stopping powers, such as the Andersen-Ziegler (AZ) values, will lead to an improvement in quantitative accuracy for any ion beam techniques within the energy range investigated here (50-170 keV).

3.2 Experimental details

Medium energy ion scattering is particularly well suited for the energy loss studies at medium ion energies (50-500 keV), due to the high energy-resolution detectors involved ($\Delta E/E$ <

10^{-2}). However MEIS requires the ultra-thin film target to possess a uniform thickness and composition over a large surface area, to account for a finite ion-beam width. Molecular beam epitaxy (MBE) is a deposition technique that can be used for the creation of such high-quality thin films. MBE growth was done using a UHV chamber (Kurt Lesker) containing two sources, Si (Alfa Aesar, 99.9999% purity) and Ti (Alfa Aesar, 99.999% purity) and evaporated using electron-beam heating. Films of Ti and Si, 10-25 nm thick were deposited on n-Si(100) and diamond-like carbon (DLC) substrates at room temperature. For the Si substrate, the passive oxide layer was removed by etching for 60 s in a HF buffer solution before Ti deposition. TiO_2 films, 9–12 nm thick were fabricated by Ti deposition onto Si(100) and subsequent oxidation in O_2 (Praxair, 99.999% purity) for 30 min at 200°C and 103.4 Torr.

The stoichiometry and lateral uniformity of deposited Si and Ti films were determined with RBS, using 0.5 MeV $^4He^+$ ions at the Western University Tandetron Accelerator Facility. Simulated RBS spectra were calculated using SIMNRA software, v.6.05 [24] with Andersen's corrections to Rutherford cross-sections. Rotating random incidence was used with a sample tilted 5° off the channeling axis and rotated azimuthally during measurements. Hydrogen content in all films was below 0.2% based on elastic recoil detection analysis. The chemical composition of the Ti, Si, and TiO_2 films were analyzed by XPS (Surface Science Western) with monochromatic Al K_α source (Kratos AXIS Ultra Spectrometer). The XPS energy calibration proceeded by assigning the C 1s feature (C-C bond) at 284.6 eV. Simulated photoelectron spectra were calculated using CasaXPS software [25]. No significant amount of other impurities (except for C) was detected by XPS.

MEIS measurements were performed using 55-170 keV H^+ ions in random and double aligned geometries. The latter consists of aligning the incident beam along a major crystallographic direction of the Si(001)-substrate (i.e. channeling) and the detector aligned to a different crystallographic direction, blocking ions scattered from substrate atoms from reaching the detector. Together this greatly reduces the contribution of the substrate signal to the scattering spectra. The details of the experimental apparatus and MEIS image corrections can be found in Kim et al. [26]. A detailed account of the MEIS data acquisition, the iterative procedure involved in determination of SCSs from MEIS spectra, and the relevant equations can be found in Dedyulin et al.[22]. The experimental MEIS spectra were fitted manually using MEISwin v.1.02 software [27].

When determining SCSs of thin films from MEIS spectra, the energy loss of protons, traveling through the entirety of a given film is given by:

$$\Delta E_{\mathrm{Film}} = E_{Sub}^{\mathrm{Film}/Sub} - E_{Sub}^{surf} = E_{Sub}^{\mathrm{Film}/Sub} - \frac{K_{Sub}}{K_{Film}} E_{Film}^{surf} \tag{3.2}$$

where K_{Sub} and K_{Film} are the kinematic factors for the substrate and film respectively. For a TiO_2 film on a Si substrate, the first term in Equation 3.2 is the position of the Si-edge in the MEIS spectrum and the second term represents the position of a Si-edge of a pure, uncovered, Si-substrate. The difference between these energies represents the energy loss through the film. Through their respective kinematic factors, the surface-edge of Si can be equated to the surface-edge of Ti in terms of the incident energy. Therefore, in order to measure the energy loss in the TiO_2 film, one needs to determine two quantities (directly from MEIS spectra): the Ti surface-edge position and the position of the Si substrate edge.

Figure 3.1(a) presents a typical 3D MEIS spectrum showing scattering intensity as a function of angle and energy while Figure 3.1(b) illustrates determination of edge position by taking the derivative of the intensity with respect to energy.

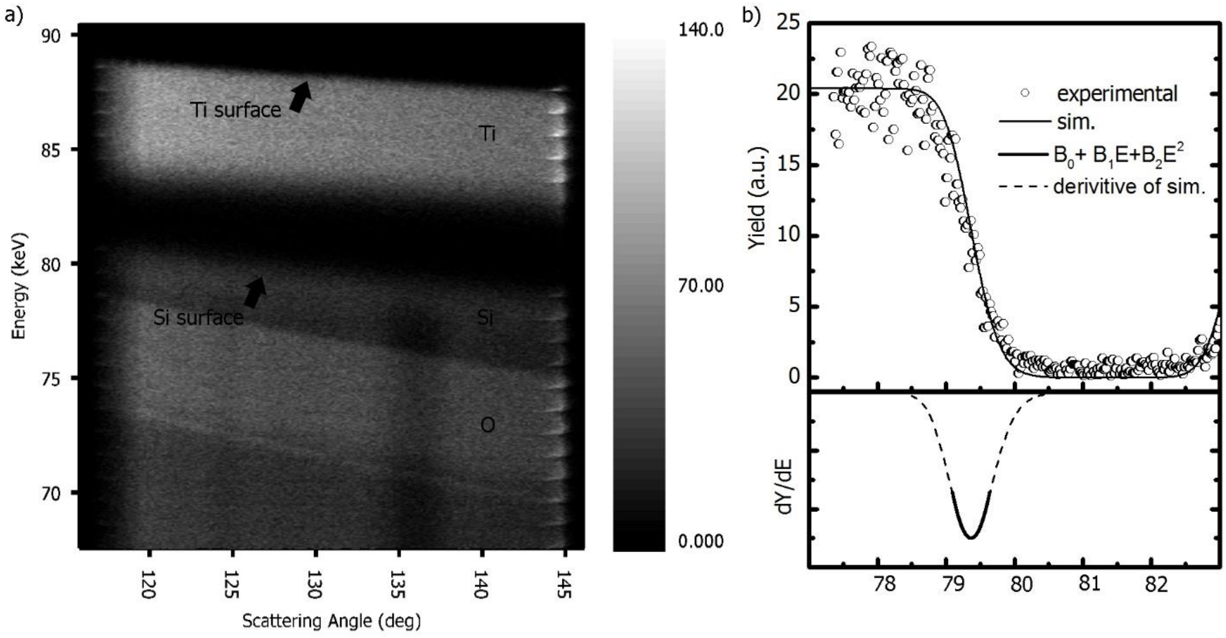

Figure 3.1: (a) A 170 keV -H^+ 3D MEIS spectrum for a 9 nm TiO_2 film. (b) A backscattering energy spectrum at 135^0 summed over a 1^0 interval and fitted using elemental Si and the simulated spectra's derivative, with respect to energy, is also shown and fitted with a quadratic function to determine position of Si edge as used in Equation 3.2.

The procedure for determination of SCS from ΔE is given in detail elsewhere [22]. Based on this procedure, the relevant sources of uncertainty for the experimental SCS are the energy loss through the film, ΔE, and the film thickness, $N\Delta x$. The uncertainty of $N\Delta x$ was obtained by RBS measurements using a Sb implanted sample, the procedure for which is described elsewhere [22] and the uncertainty of the Sb areal density is estimated to be approximately 2.2% as described on page 355 of reference [4]. Our estimates of Ti and Si areal densities rely on Ti and Si peaks in RBS measurements, since oxygen areal densities can be only estimated from RBS with larger uncertainties. The statistical uncertainties on Si and Ti signals were between 1-3%, depending on the thickness and the statistical uncertainty of the Sb signal was 1.4%. Using the statistical uncertainties listed above and the uncertainty of the Sb areal density, and the uncertainty for the RBS scattering angle, the uncertainty for thin-film thickness values, $N\Delta x$, of 4 % was introduced.

Secondly, the uncertainty in ΔE can be estimated using Eqn. 2. We estimated the uncertainty for both Si and Ti edges from various fits of MEIS spectra to be 0.05 keV. Additionally there is an uncertainty associated with the fitting of a quadratic function to the simulated spectra [22]. The experimental data was differentiated and fit with a two-piece asymmetric Gaussian and the edge positions compared to the fitting procedure described above. The difference between the edge positions using the two procedures was 0.04 keV, not a significant source of uncertainty but worth consideration. There will be two additional uncertainties associated with the kinematic factor of substrate and film elements due to uncertainty in the MEIS scattering angle. Using the equation for the kinematic factor, we can calculate the uncertainty of the kinematic factor to be: $\Delta K = \left|\frac{\partial K}{\partial \theta}\right| \Delta\theta$, where $\Delta\theta = 0.1^{o}$ for MEIS. This results in: $K \pm \Delta K = 0.930 \pm 0.001$ for H on Ti and $K \pm \Delta K = 0.880 \pm 0.002$ for H in Si, both at a scattering angle $\theta = 135$ ^{o}. These ΔK lead to the relative uncertainties of 0.2% for H^+ on Ti and 0.3% for H^+ on Si. Total relative uncertainty in ΔE_{Film}, is calculated with uncertainty in edge positions, uncertainty in kinematic factors, and with beam energy spread and is estimated to be 0.7%. The total uncertainty from ΔE and $N\Delta x$ for the SCS is thus estimated to be better than 5%. A summary of all relative uncertainties are given in Table 3.1.

Table 3.1: All the relevant sources of uncertainty that were taking into account when calculating the relative uncertainties for ΔE and NΔx, as explained above.

Quantity	**Description**	**Relative uncertainty (%)**
δA_{Sb}	uncertainty of Sb standard areal density	2.2
$\delta \theta_1$	uncertainty of RBS scattering angle (fixed angle)	0.29
$\delta \theta_2$	uncertainty of MEIS scattering angle (smallest angle used)	0.11
δS	uncertainty in screening correction	0.10
δB_{Ti}	uncertainty in Ti composition	0.10
$\delta \sigma_{Sb}$	statistical uncertainty of Sb signal	1.4
$\delta \sigma_{Ti, Si}$	statistical uncertainty of Ti or Si signal (thinnest sample)	3.2
δK_{Si}	uncertainty in Si kinematic factor	0.26
δK_{Ti}	uncertainty in Ti kinematic factor	0.15
δE_x^y	uncertainty in edge position	0.60
δE_{fit}	uncertainty in fit of edge position	0.48
δE_{max}	energy spread at maximum	0.25

For the MBE grown Ti and Si, we ignored any small compositional variation that might be expected in the oxide layers and deduced the oxide layer thickness from the total O content as measured by RBS and MEIS. We felt an assumption that the small relative contribution of a transitional oxide layer to the total energy loss would introduce negligible uncertainty compared to the uncertainty associated with ΔE and the film thickness, NΔx. For example, by fitting the spectra, we could modify the thickness of the oxide layer showing systematic shift from experimental data. For the thicker oxide layers, the total Ti content was kept constant to reflect transitional oxide layers. Despite dramatic changes to the oxide thickness, the SCS decreased only slightly. For example in Ti, for a 15% increase in oxide thickness, the SCS decreased only by about 3% . The purpose was to convince ourselves that the Nt and ΔE values were the main sources of uncertainty when compared to this assumption we had made to ignore the compositional variation of the oxide layer.

3.3 Results and discussion

The procedure for calculating SCSs from MEIS spectra described above was applied here for Si and Ti mono-elemental ultra-thin films to find the respective SCSs for protons between 50-170 keV. Our experimentally determined SCSs are shown in Figure 3.2 along with the commonly used semi-empirical stopping power curve from SRIM [28] and the PSTAR database [29]. We compare our results to values found in the literature [30-36]. The results for ε_{Si} and ε_{Ti} are self-consistent and show good agreement (±2%) with the values predicted by PSTAR. However, SRIM appears to underestimate the stopping cross section around the maximum for both ε_{Si} and ε_{Ti}. The agreement between the experimental SCSs of Ti and Si and the PSTAR values validates our iterative technique for determination of SCSs from the energy loss measured by MEIS. Given that, we can also conclude the ε_{Ti} (if PSTAR values are used) cannot account for the previously reported [22] deviations of $SrTiO_3$ SCSs in the same energy range.

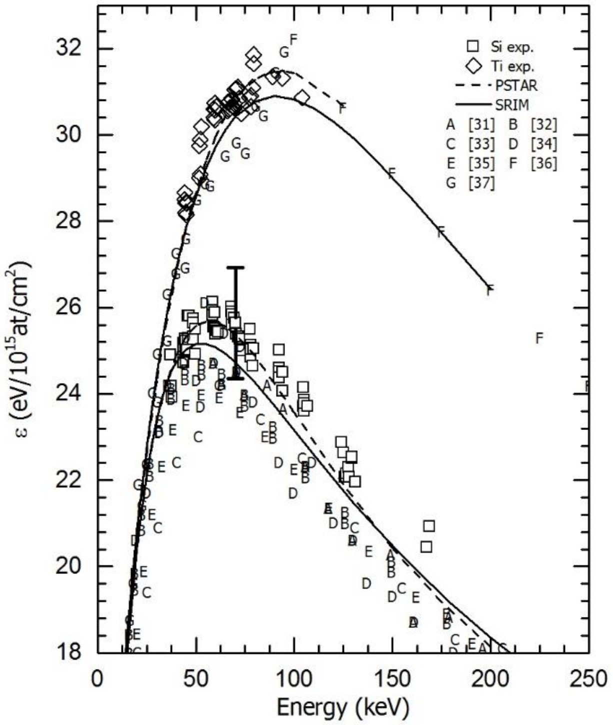

Figure 3.2: Experimentally determined ε_{Ti} and ε_{Si} in comparison with values from with SRIM2003 [28], NIST PSTAR [29] database values, and literature values [30-36]. Experimental uncertainty is shown as error bar for a single value of ε_{Si}.

Compared to Si, published data for the SCSs of Ti for protons in the relevant energy range are limited. However, there have been studies on the stopping of deuteron in Ti which are self-consistent in the energy range of this paper (50-170 keV) [35, 36] and consistent with SRIM-03 and AZ [28] predictions. An important question is whether or not studies of cross sections for deuterons can be compared to the proton stopping cross section. There have been studies comparing the stopping powers (stopping cross sections) for H^+ and D^+ at the same energy in many materials. Shiomi-Tsuda et al. found no systematic difference between the two ions, within estimated uncertainty of 0.35% [37]. This explains the consistency of the deuteron studies with SRIM-2013 and AZ predictions of protons.

XPS analysis performed on the TiO_2 films, confirms that a vast majority (>99%) of titanium is in the Ti^{+4} oxidation state, as shown in Figure 3.3. Discrepancies between experimental data and simulated spectra at around 461 eV and 456 eV can be explained by a contributions from trace amounts of other oxides such as Ti_2O_3, the binding energy of which is, around 456.8 eV and 462.0 eV for the $2p_{3/2}$ and $2p_{1/2}$ peaks respectively [38]. TiO's $2p_{3/2}$ peak is around 454.6 eV and the $2p_{1/2}$ peak is found at 460.2 eV [38]. No evidence of metallic Ti was detected (Ti $2p_{3/2}$ peak at 454.0 eV [37] was below XPS detection limits) in the near surface layer.

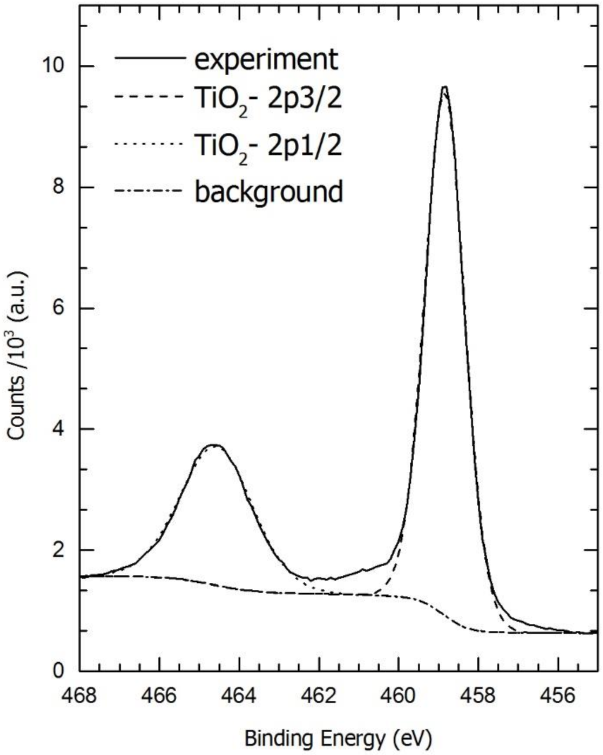

Figure 3.3: Ti 2p XPS results for the 9 nm TiO_2 film. The black solid line represents the experimental measurements. The dashed lines represent the simulated contribution from the $2p_{3/2}$ and $2p_{1/2}$ electronic states, respectively, associated with TiO_2.

Having established the validity of the procedure, with our ε_{Ti} and ε_{Si} values, we then applied it to measure the energy loss of protons in TiO_2 thin-films in the 50-170 keV range. The experimental results for ε_{TiO2} are presented in Figure 3.4, which shows ε_{TiO2} as a function of scattering energy. Multiple data points of the same energy were reported as average values.

The dotted line represents the fitting of the experimental data to an 8-coefficient stopping power curve [4]. From this curve the stopping power maximum is found at 102 keV and determined to be 18.4 $eVcm^2/10^{15}$atoms. The experimentally determined energy losses lie systematically lower than SRIM's prediction. The predicted values appear to be overestimated by SRIM by ≈14%. The experimental data are shifted to higher energies as compared to SRIM which has a stopping power maximum at about 95 keV. The observed discrepancy between the experimental data for TiO_2 and Bragg's rule predictions may be explained by the inaccurate stopping power of O used in the Bragg calculation. ε_O are coming from gaseous state measurements and may not be applicable to the current context, i.e. the physical effects as explained in the introduction. To determine if the deviation is due to a physical effect, the experimentally determined SCSs for Ti and TiO_2 were compared to the $SrTiO_3$ data.

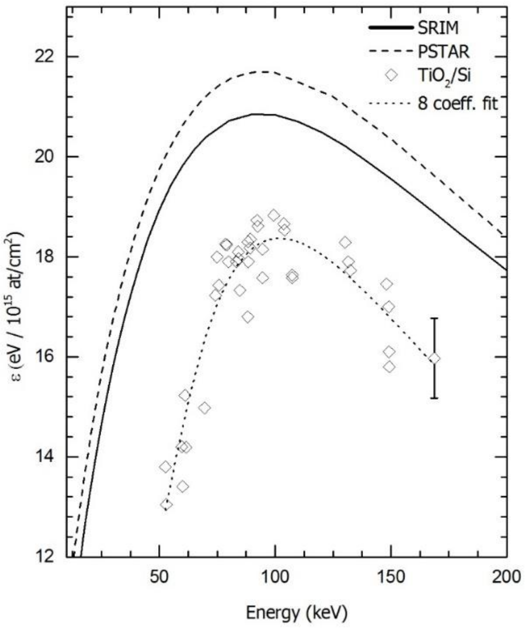

Figure 3.4: Experimental SCS for TiO_2. The experimental data were fit as an 8-coefficient stopping power curve [4]. Comparison of experimental data and Bragg's rule predictions from SRIM2003 [28] and NIST PSTAR database values [29]. Error bars for a single measurement are included for clarity.

Experimental SCS results for TiO_2 are not abundant. Kido and Hioki [39] used nuclear reaction analysis to determine the SCSs of protons in TiO_2 for three energies, 632, 774, and 992 keV, comparing them to semi-empirical AZ values [40]. Silvina et al. [41] measured SCSs for protons in TiO_2 films in the range of 200-1500 keV from RBS spectra and compared them with SRIM2012 values [28]. Both studies found good agreement between their experimental SCSs and the respective application of Bragg's rule and their results appear mutually consistent. However, the energies involved were far above the stopping maximum, where significant deviations from Bragg's rule would be expected, and that are addressed in to the present study.

An important consideration is why there is not a deviation from stopping power maximum for He^+ in TiO_2 in Silvina et al. [41] while such an effect is readily apparent in our data of H^+ in TiO_2 if the effective charge approximation is to hold. Primetzhofer [42] determined the stopping cross sections for H^+ in HfO_2 and found that SRIM overestimates the energy loss over the whole region of investigated velocities and cites a volition of Bragg's law due to chemical effects. Behar et al.[43] provide experimental stopping power data for He^+ in HfO_2, which show good agreement with SRIM at lower energies (up to 400 keV) but for larger energies, most notably at stopping maximum (around 800 keV), it again overestimates the energy loss. The present data is of course limited and as such it is not obvious that the effective charge approximation is valid at stopping maximum.

Our procedure for determining SCSs of thin-films from MEIS spectra was initially applied to $SrTiO_3$ thin-films. Deviations from Bragg's rule, at the stopping maximum, of ≈10% were noted. Our previously reported results for the experimental ε_{STO} values are summarized in Figure 3.5. They were systematically lower than the Bragg's rule calculations, given by SRIM and the interpolated 5- and 8-coefficient fits of collected stopping power data with the stopping power maximum, again being shifted towards higher energy [22].

The experimentally determined ε_{TiO2} values were fitted to an 8-coefficient AZ stopping power curve as seen in Figure 3.4 Under the assumption that Bragg's rule is correct, this stopping power curve was taken together with the stopping power curve for elemental Ti (ε_{Ti}) and for every energy, ε_O was calculated by making use of Bragg's rule in the form of:

$$\varepsilon_O = \frac{3}{2}\left(\varepsilon_{TiO2} - \frac{1}{3}\varepsilon_{Ti}\right). \tag{3.3}$$

A similar procedure is repeated for $SrTiO_3$, where the elemental-SCS values for the constituent elements, in the Bragg's rule calculation, were given by our experimentally determined stopping power curves for Ti and O along with the AZ semi-empirical, interpolated curve for Sr [40]. The stopping power curve for $SrTiO_3$, derived from Bragg's rule using the new ε_O, is presented in Figure 3.5 along with previous experimentally determined SCSs data points.

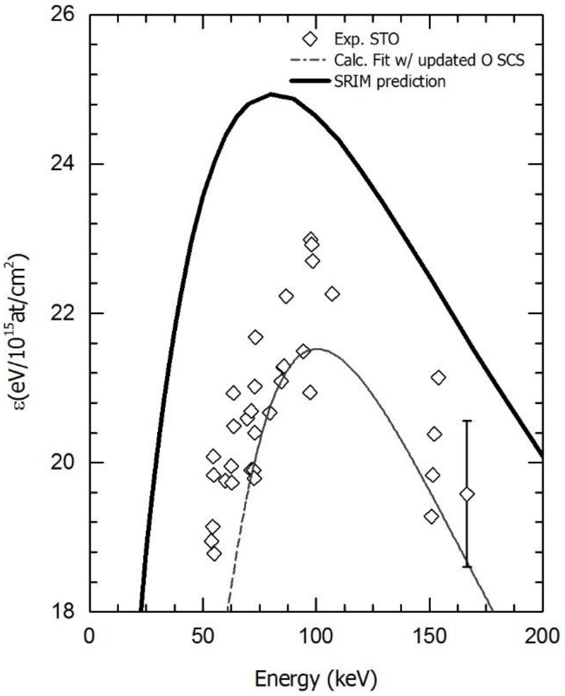

Figure 3.5: Experimental data and Bragg's rule predicted values of ε_{STO} from [22]. Comparison is made to SRIM2003 [28] values and to a stopping power curve representing Bragg's rule, applied using experimentally determined SCSs of O and Ti in addition to AZ 5-coefficient [40] values of Sr. A single experimental data error bar is shown.

The experimentally determined stopping power curve fits the $SrTiO_3$ results better than the SRIM curve. It appears a much better prediction of the energy at which stopping power maximum occurs and its value. This strongly supports the notion that the overestimated SRIM $SrTiO_3$ values were from an oxygen cross section, ε_O that was too large. Both SRIM and our $SrTiO_3$ stopping power curves make use interpolated 5-coefficient AZ curves for Sr and so, differences in the SCSs must be due to ε_{Ti} and ε_O. The agreement we saw in Figure 3.3 between ε_{Ti} and the predicted values from SRIM and PSTAR allow us to rule out ε_{Ti}. This leaves ε_O as being too high in the predicted values which in turn strongly suggests a physical effect responsible for observed deviations in both the stopping power curves of both TiO_2 and $SrTiO_3$.

3.4 Conclusions

Our work provides validation of the method for determining SCSs from MEIS spectra in conjunction with an iterative procedure originally carried out in Dedyulin et al. [22], where $SrTiO_3$ SCSs were systematically lower than SRIM predictions and shifted to lower energies. The SCSs for Ti and Si appear to be accurate for the energy range 50-170 keV within experimental uncertainties and provide strong validation of the method involved. Experimental SCSs for TiO_2 were found to be systematically lower (by ≈14 %.) as compared with SRIM predictions. At the stopping power maximum the data was shifted towards slightly higher energies with a maximum of 18.4 eVcm^2/10^{15}atoms at 99.6 keV. Applications of Bragg's rule allowed us to determine more accurate stopping power curves for O and $SrTiO_3$ in the medium ion energy range (50-170 keV). For O, SRIM predicts a stopping maximum of 17.2 eVcm^2/10^{15}atoms at 100 keV. At the same energy our ε_O value is 12.3 eVcm^2/10^{15} [1] atoms, or about 70% SRIM's value. The experimental $SrTiO_3$ SCSs better predict both the stopping power maximum value and the energy at which it occurs. The findings support the fact that physical effects on the SCSs of O should not be neglected when applied to the commonly used metal oxides such as $SrTiO_3$ and TiO_2.

3.5 References

1. J. Vickerman and I. Gilmore., *Surface Analysis: The principle Techniques*. 2009: John Wiley and Sons.

2. J.F. Ziegler and M. Manoyan, *The stopping of ions in compounds.* Nucl. Instruments Methods Phys. Res. B 1988. **35**: p. 215.
3. W.K. Chu, J.W. Mayer, and M.A. Nicolet, *Backscattering Spectrometry*. 1978: Academic Press Inc.
4. J. Tesmer and M. Nastasi, *Handbook of modern ion beam materials analysis*. 1995: Materials Research Society.
5. W. H. Bragg and R. Kleeman, *On the alpha particles of radium, and their loss of range in passing through various atoms and molecules.* Philosophical Magazine, 1905. **10**: p. 318.
6. D. Powers, *Influence of molecular structure on stopping powers of chemical species for He+ ions from a low energy particle accelerator.* Acc. Chem. Res. , 1980. **13** p. 433.
7. D.I. Thwaites, *Review of stopping powers in organic materials.* Nucl. Instruments Methods Phys. Res. B 1987. **27**: p. 293.
8. R.B. Brown and D. Powers, *Measurements of the molecular stopping cross sections of organic ring compounds.* J. Appl. Phys., 1979. **50**: p. 5099.
9. E. Chau and D. Powers, *Measurement of molecular stopping cross sections of aldehydes and ketones and calculation of the atomic stopping cross section of oxygen in double-bonded and three-membered ring-structure C-H-O compounds.* J. Appl. Phys., 1978. **49**: p. 2611.
10. J. Oddershede and J. Sabin, *Bragg rule additivity of bond stopping cross sections.* Nucl. Instrum. Methods Phys. Res. B, 1989. **42**: p. 7.
11. P. Bourland and D. Powers, *Bragg-Rule Applicability to Stopping Cross Sections of Gases for α Particles of Energy 0.3-2.0 MeV.* Phys. Rev. B, 1971. **3**: p. 3635.
12. D.C. Santry and R.D. Werner, *Energy loss of 4He ions in AI2O3 and SiO2.* Nucl. Instrum. Methods Phys. Res. B, 1986. **14**: p. 169.
13. D. Thwaites, *Bragg's Rule of Stopping Power Additivity: A Compilation and Summary of Results.* Radiat. Res., 1983. **95**: p. 495.
14. Y. Hoshino, et al., *Correction of Ziegler's stopping powers of Al, Si and their oxides for MeV He ions.* Nucl. Instrum. Methods Phys. Res. B, 2000. **171**: p. 409.
15. J.F. Ziegler, W.K. Chu, and J.S.-Y. Feng, *Empirical corrections to the energy loss of 4He ions in oxides.* Appl. Phys. Lett., 1975. **27**: p. 387.
16. W.N. Lennard, H. Xia, and J.K. Kim, *Revisiting the stopping powers of Si and* SiO_2 *for 4He ions: 0.5–2.0 MeV.* Nucl. Instrum. Methods Phys. Res. B, 2004. **215**: p. 297.
17. C. Pascual-Izarra, et al., *Stopping power of SiO sub 2 for 0.2-3.0 MeV He ions.* Nucl. Instrum. Methods Phys. Res. B, 2002. **196**: p. 209.
18. W. Neuwirth, et al., *On the invalidity of Bragg's rule in stopping cross sections of molecules for swift Li ions.* Zeitschrift Fur Phys. A: Atoms Nucl., 1975. **275**: p. 215.
19. J.F. Ziegler, *Stopping of energetic light ions in elemental matter.* J. Appl. Phys., 1999. **85**: p. 1249.
20. D.I. Thwaites, *Current status of physical state effects on stopping power.* Nucl. Instruments Methods Phys. Res. B 1985. **12**: p. 84.
21. H. Paul. *Stopping Power for Light and Heavier Ions*. 2015; Institut fur Experimental physik]. Available from: http://www.exphys.jku.at/stopping/.
22. S.N. Dedyulin, et al., *Energy loss of protons in SrTiO3 studied by medium energy ion scattering.* Nucl. Instruments Methods Phys. Res. B 2012. **288**: p. 60.
23. E. Rauhala, et al., *Status of ion beam data analysis and simulation software.* Nucl. Instrum. Methods Phys.Res. B, 2006. **244**(2): p. 436.

24. M. Mayer, *SIMNRA v. 6.05*. 1997.
25. N. Fairley, *CasaXPS*. 2013.
26. J. Kim, et al., *Depth profiling of ultrathin films using medium energy ion scattering.* Curr. Appl. Phys. , 2003. **3**: p. 75.
27. T. Nishimura, *MEISwin v. 1.0X* 2015.
28. J.F. Ziegler, *SRIM*, *www.srim.org*. 2015.
29. M.J. Berger, et al., NIST Standard Reference Database 124 (2005), http://www.nist.gov/pml/data/star/, 2005.
30. M. Abdesselam, et al., *Stopping of 0.3–1.2 MeV/u protons and alpha particles in Si.* Nucl. Instrum. Methods Phys. Res. B, 2008. **266**: p. 3899.
31. G. Konac, et al., *Energy loss and straggling of H and He ions of keV energies in Si and C* Nucl. Instrum. Methods Phys.Res. B, 1998. **159**: p. 136.
32. M. Fama, et al., *Energy loss and angular dispersion of 2–200 keV protons in amorphous silicon.* Nucl. Instrum. Methods Phys.Res. B, 2002. **91**: p. 193.
33. A. Ikeda, et al., *Stopping powers and energy staggling for 50–300 keV H+ in amorphous Si and Ge films.* Nucl. Instrum. Methods Phys.Res. B, 1996. **115**: p. 34.
34. D. Niemann, G. Konac, and S. Kalbitzer, *Stopping power measurements of 1H, 4He and 14N in Si in the energy range of 0.02–1 MeV/amu.* Nucl. Instrum. Methods Phys. Res. B, 1996. **118**: p. 11.
35. D.C. Santry and R.D. Werner, *Stopping powers of C, Al, Si, Ti, Ni, Ag and Au for deuteron.* Nucl. Instrum. Methods Phys.Res., 1981. **188**: p. 211.
36. J.H. Ormrod, *Electronic stopping cross sections of deutrons in titanium.* Nuclear Instruments and Methods, 1971. **95**(1): p. 49.
37. N. Shiomi-Tsuda, N. Sakamoto, and R. Ishiwari, *Stopping powers of Be, Al, Ti, V, Fe, Co, Ni, Cu, Zn, Mo, Rh, Ag, Sn, Ta, Pt and Au for 13 MeV deuterons.* Nucl. Instrum. Methods Phys.Res. B, 1994. **93**: p. 391.
38. D. Gonbeau, et al., *XPS study of thin films of titanium oxysulfides.* Surf. Sci., 1991. **254**: p. 81.
39. Y. Kido and T. Hioki, *Measurements of energy loss and straggling for fast H+ in metals and their compounds by means of a nuclear resonant reaction.* Phys. Rev., 1983. **8**: p. 2667.
40. H.H. Andersen and J.F. Ziegler, *Hydrogen: Stopping Powers and Ranges in all Elements*. 1977: Pergamon Press, Inc.
41. L. Silvina, et al., *Stopping cross sections of TiO_2 for H and He ions.* Eur. Phys. J. D, 2014. **68**: p. 194.
42. D. Primetzhofer, *Electronic stopping power of hydrogen in a high-k material at the stopping maximum and below*. Nucl. Instr. Meth. B, 2014. **320**: p. 100.
43. M. Behar, et al., *Energy loss of proton, α particle, and electron beams in hafnium dioxide films.* Phys. Rev. A, 2009. **80**: p. 62901.

Chapter 4: Probing anodic TiO_2 growth mechanisms: using medium energy ion scattering and nuclear reaction profiling

4.1. Introduction

Much of modern technology is predicated on the use of reactive metals that exhibit a high affinity for oxygen [1]. Reactive metals such as Ti are of special interest since, when exposed to oxygen rich environments, they spontaneously form oxides that are thermodynamically stable, highly insoluble, and hence provide excellent corrosion resistance in most corrosive media [2]. The low reactivity of the passive oxide with human tissues is why “commercially pure” Ti (ASTP F67) is ubiquitous as dental [3] and biomedical [4] implants.

Anodization is the preferred method to form porous and thick oxide films for such applications [5], however many factors can impact passive oxide stability through modification of its composition and structure in the specific fluidic environment [6]. The oxide films formed can be crystalline or amorphous depending on the anodization potential and electrolyte involved [7]. The processing conditions also determine the specific crystal structure (rutile vs. anatase, etc.), which directly affects the degree of adsorption of oxidizing species from human plasma, as rutile has a more closely packed structure with fewer paths for ion diffusion compared to anatase and as such will better resist corrosion [8]. A complete description of the anodization process, at the level of ionic mass transportation will allow for better manipulation of the processes and enable the development of more effective corrosion-resistant films.

There is a wide consensus that the rate of anodic oxide growth is limited by the mass-transport of ionic species through the existing oxide film [9] and consequently two competing models have been developed that purport to describe anodic oxide growth based on such ionic mass-transport: the high-field model (HFM) [10] and the point defect model (PDM) [11]. Both models are described in Chapter 1 of this thesis, with further mathematical details provided given in Appendix A1.

In the HFM, strong electric fields (~10^{11} V/cm [9]) render diffusion negligible [12] and force the migration of cations from the oxide/metal interface, down the potential gradient, to the electrolyte/oxide interface, where they react with oxygen anions in solution, to form new oxide. Simultaneously, oxygen anions are transported from the electrolyte/oxide interface, to the oxide/metal interface where they react with metallic species, to form new oxide. New oxide growth happens in two locations and the relative contribution of each is a function of the metal and processing conditions [13]. The quantities t_a and t_c are anionic and cationic transport numbers and represent the fraction of newly formed oxide created due to the respective ions and reflect the relative mobility. The sum of the contributions from each ionic species must be: $t_a + t_c = 1$.

The PDM is a "low-field" approach that requires the oxide film to contain a high concentration of point-defects that carry the ionic current, with negligible interaction between them [14],[15]. The anodic oxide film is postulated to have a bi-layer structure; a "barrier-layer" adjacent to the metal surface, and a precipitated outer layer that forms over time between the solution and barrier layer [15]. Anion vacancies are continually created at the oxide/metal interface, when O atoms in the oxide sublattice react with Ti atoms, in the metal substrate. The O vacancy will be filled by O ions immediately adjacent to it and propagate towards the oxide/electrolyte interface. Through subsequent fillings, the vacancy is transported to the oxide/electrolyte interface and where it is consumed by O anions from solution. Cation vacancies are continually created at the electrolyte/oxide interface, when Ti^{4+} ions are ejected into the electrolyte from the metal sublattice, where they react with O anions from solution, which leads to the formation of a precipitated oxide layer [9]. Through successive fillings, cation vacancies are transported to the metal/oxide interface and are consumed when a metal atom in the metal substrate fills the vacancy. Ultimately according to the PDM, the barrier layer's movement into the metal represents the "corrosion front", while the O atoms originally in the barrier-layer remain as part of it, as the precipitated outer layer oxide grows incorporating O from the electrolyte.

4.2 Experimental details

Given that both models of anodization make different predictions regarding the resultant oxide film structure, to distinguish between them it is necessary to develop techniques that enable the precise characterization of the atomic species that have adhered to the electrode during anodization. The approach used here involves an $^{18}O/^{16}O$ isotopic labelling procedure, with two consecutive oxidations. We utilized two complementary depth profiling techniques, ideal for isotopic tracing studies, which can differentiate between the O isotopes: medium energy ion scattering (MEIS) and nuclear reaction profiling (NRP). NRP was chosen as a complementary technique to MEIS, because the nuclear reaction involved is isotope specific and there is no background signal from other elements in the oxide films (including the substrate).

Titanium films with physical thickness of 14.0 ± 0.5 nm were deposited by magnetron sputtering onto a Si (001) 4.5" wafer. The Ti films were exposed to isotopic ^{18}O water immediately after deposition, without exposure to air, to form passive ultra-thin $Ti^{18}O_2$ films. Uniformity of the oxide film composition and thickness (±4%) was confirmed by X-ray reflectometry (XRR) and Rutherford backscattering spectrometry (RBS). The $Ti^{18}O_2$/Ti/Si(001) films were anodized in $D_2{}^{16}O$ water, over a range of voltages, from 0 to 10 V, applied in potentiostatic mode, resulting in

~4–30 nm oxide layers. The crystallinity of the finial films was assessed with X-ray diffraction (XRD) using a Mo Kα source (Nonius Kappa CCD Diffractometer). The chemical composition of the films were analyzed by XPS (Surface Science Western) with X-rays generated from a monochromatic Al Kα source (Kratos AXIS Ultra Spectrometer). The XPS energy calibration proceeded by assigning the C 1s feature (C-C bonds) at the adventitious carbon to a value of 284.6 eV. Simulated photoelectron spectra was evaluated calculated using CasaXPS software [16].

The thickness and composition of the TiO_2 films were measured by MEIS. In order to separate the ^{18}O and ^{16}O isotopes well in energy, MEIS depth profiling was performed using 200 keV H^+ ions in "double-alignment" geometry, at the Western University Tandetron Accelerator Facility. This consists of aligning the incident beam along a major crystallographic direction of the Si(001) substrate (i.e. channeling) and aligning the center of the toroidal electrostatic energy analyser (TEA) to a another crystallographic direction (i.e., blocking). Using this configuration results in a significant reduction in backscattering from the Si substrate in the MEIS spectra, preventing the signal from the Si substrate from obscuring lighter elements (i.e. O isotopes). The details of the experimental apparatus and MEIS image corrections can be found in Kim et al. [17]. The experimental MEIS spectra were fitted using MEISwin v.1.02 software [18]. The backscattering intensity has been summed over a 1^o angular range for improved signal-to-noise ratio.

The areal density of ^{18}O through the oxide films was also measured with NRP via the narrow $^{18}O(p,\alpha)^{15}N$ resonance appearing on the H^+ cross-section curve at 151 keV (with a width Γ~100 eV), using a Si detector. A $Ta_2{}^{18}O_5$ calibration standard was used for ^{18}O quantification. Although there are deuterium induced reactions for ^{16}O, the widths of the resonances where not sufficiently narrow for our depth profiling purposes. There are also safety considerations associated with deuterium-deuterium reactions, which unavoidably occur, emitting ionizing fast neutrons.

Areal densities of hydrogen and deuterium were measured with elastic recoil detection (ERD). Samples were studied using a 2.9 MeV ^{4}He beam in a conventional ERD setup with incident angle of 75°, recoil angle of 30° in IBM geometry and a 12.2 μm Al-coated polyethylene terephthalate (PET, mylar©) range foil. Poly 4,4'-oxydiphenylene-pyromellitimide (Kapton®) and H-implanted Si targets were used as standards to determine the detector solid angle (both yielding values within 3% of each other).

4.3 Results

Figure 4.1 shows the compositional changes in the anodic Ti oxide as a function of anodization voltage, in terms of H^+ backscattering spectra of $Ti^{18}O_2$/Ti/Si(001) films before (0 V) and after anodization (2 and 5 V) in $D_2{}^{16}O$. In MEIS, the incident ions scattered from heavier elements will be detected at higher energy, so the elements in the target appear in order of increasing mass, with Ti being the heaviest. The H^+ energies corresponding to the high-energy edges of Ti, O, and C (but not Si) peaks are in excellent agreement with the binary collision model, which implies that all these elements can be found on the surface, while Si is completely buried by the film. A small amount of hydrocarbon contamination at the top surface is apparent from a minor C surface peak (confirmed by XPS).

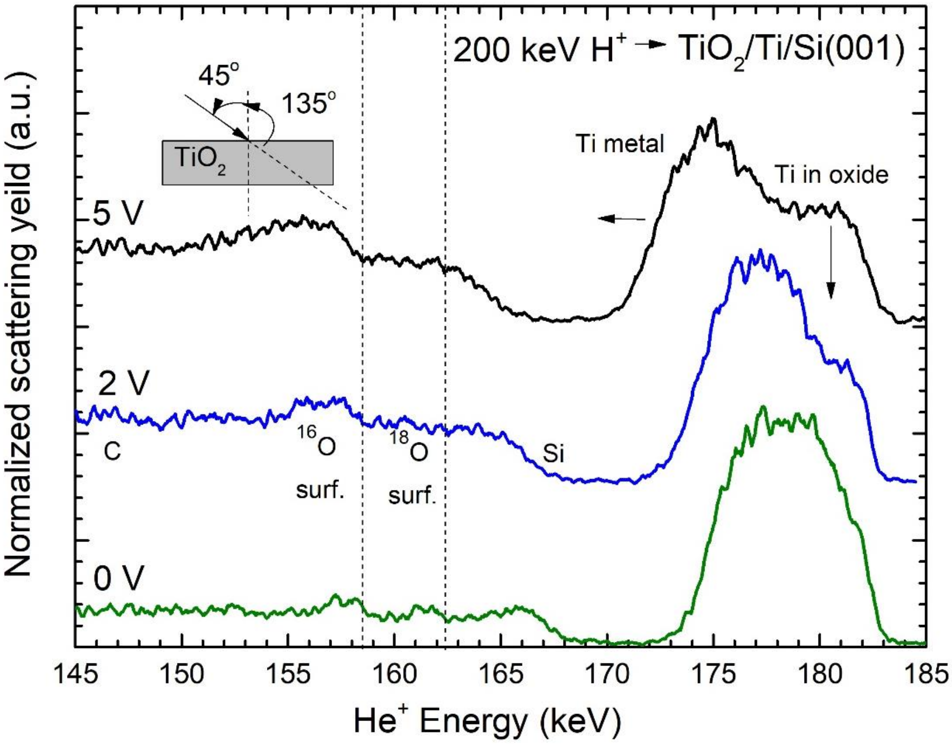

Figure 4.1: MEIS spectra for TiO_2/Ti/Si(001) reflecting compositional changes in films as a function of anodization voltage. Data was acquired using a beam of 200 keV H^+ with an incident angle of 45^0 and a scattering angle of 135^0.

In MEIS, the backscattering intensity is linearly proportional to elemental areal density. In Figure 4.1, the lower areal density of Ti in the oxide results in a decrease in peak intensity, relative to metallic Ti, to reflect the stoichiometry of Ti in the oxide. Additionally, incident H^+ lose energy inelastically, from electronic interactions, as they penetrate the films. The greater the oxide thickness, the more energy that they lose before backscattering off the Ti metal. So an increasing oxide thickness, as a function of anodization voltage, explains the movement of the metalic Ti peak to lower energies. From 0 V to 5 V, the Ti peak position is pushed to lower energies by ≈ 3.4 keV. As Ti metal is consumed, the features in the spectra that correspond to Ti metal, become increasingly thinner. Notably, we do not observe any changes in the total Ti areal density within our experimental uncertainty $(4.47 \pm 0.07) \times 10^{16}$ atoms/cm^2 (integrated over the TiO_2 and Ti layers), indicating that there is no dissolution of Ti into the electrolyte solution at any point during the anodization process.

The respective surface position of the ^{18}O and ^{16}O peaks are denoted by the vertical dashed lines in Figure 4.1. From 0 V to 2 V anodizations, the ^{18}O peak position shifts to lower energies by 1 keV and by another 2.6 keV from 2 V to 5 V anodizations, such that that it overlaps with the ^{16}O surface peak. Such energy loss means that the oxide layer containing ^{18}O, is covered by an increasingly thickening layer of ^{16}O oxide. This should be contrasted with a lack of change in the ^{16}O surface position relative to where is located at 0 V, suggesting that ^{16}O always represents the composition of the outermost oxide layer. From 0 V to 5 V anodizations, the width of ^{16}O peak monotonically increases in width, suggesting that most of the oxide growth is due to an increasing incorporation of ^{16}O. Not that due to the ^{16}O and ^{18}O peak overlap at higher oxidation voltages, more accurate ^{18}O depth profiling will be produced using nuclear reaction profiling (to be discussed later).

To restrain and justify the stiochiometry of the oxide used in the MEIS simulations, XPS was performed. The high-resolution XPS spectrum for the Ti 2p region is presented in Figure 4.2. The main doublet peak (459.0 eV and 464.5 eV [19]) is attributed to Ti^{4+}, indicating TiO_2 is the primary constituent of the oxide film (~ 85 % of the Ti is in the oxidation state Ti^{+4}). The peaks can be deconvoluted into a number of minor contributions, from trace amounts of other oxides, such as Ti_2O_3, for which the binding energy is ~ 456.8 eV and ~ 462.0 eV [20], for the $2p_{3/2}$ and $2p_{1/2}$ peaks respectively, and TiO for which the binding energy for the $2p_{3/2}$ peak is ~ 454.6 eV and the $2p_{1/2}$ peak is found at ~ 460.2 eV [20]. There is evidence of metallic Ti (Ti $2p_{3/2}$ peak at 454.0 eV [21]), indicating the deposited Ti is not fully oxidized. Wang et al. noted that 90% of the Ti oxide formed from their anodization, for the first 2.5 nm was TiO_2 (a thickness comparable to our own), with an increase in sub-oxides (TiO and Ti_2O_3) occurring at greater depths into the film below 2.5 nm [22]. Such sub-oxides can also be observed in the MEIS depth profiles (Figure 4.3).

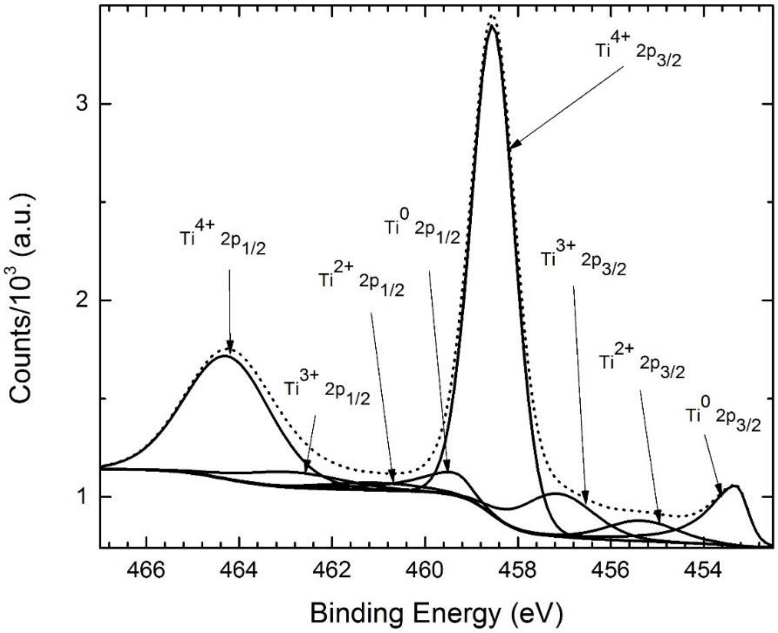

Figure 4.2: XPS data for the Ti 2p region, showing the oxidation states of Ti.

For quantitative information on film thickness and elemental areal density, the MEIS spectra were simulated using the O depth profiles, in Figure 4.3, which show the effect on the ^{18}O and ^{16}O depth profiles when $Ti^{18}O_2/Ti/Si(001)$ is anodized in $D_2{}^{16}O$, at 0 - 1.5 V (a,c) and 2 – 10 V (b,d), respectively.

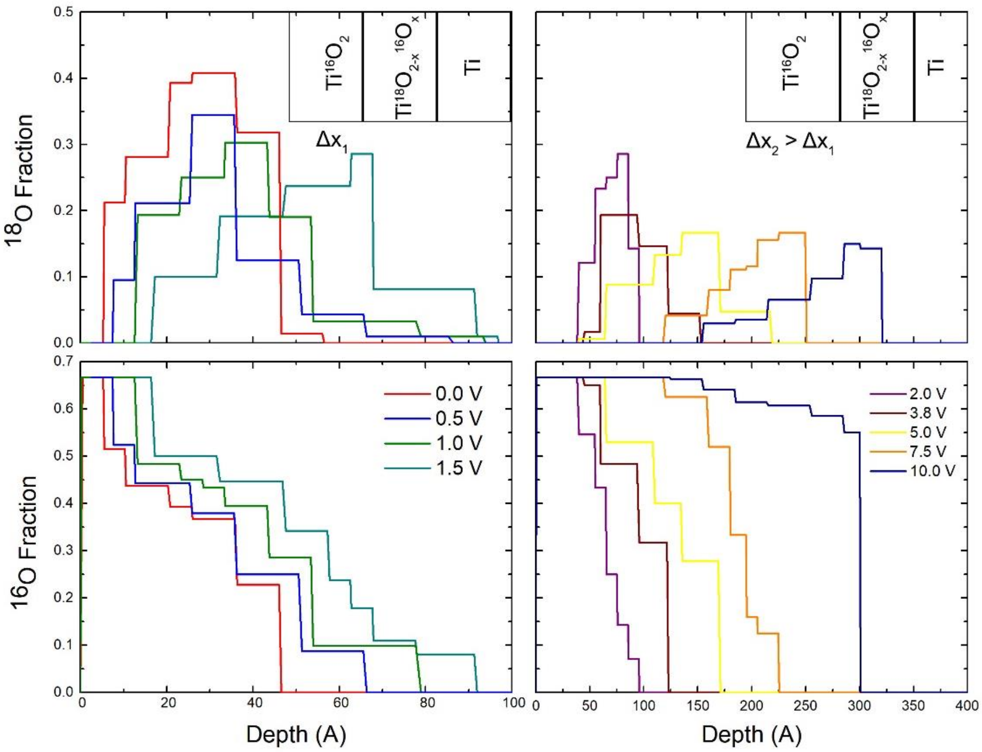

Figure 4.3: Evolution of the MEIS ^{18}O ((a) and (c)) and ^{16}O ((b) and (d)) depth profiles, after anodization in $D_2{}^{16}O$, for voltages 0 – 10 V. Depth profiles are derived from simulations of the MEIS spectra and show the fraction of the respective isotope in the oxide. The insets show the effect of anodization on the O profiles: a $Ti^{16}O_2$/ $Ti^{18}O_{2-x}{}^{16}O_x$ bi-layer structure is maintained over all voltages.

The total ^{18}O areal density remains constant across all potentials (Figure 4.4) within experimental uncertainty, with an average value of $(1.29 \pm 0.06)\times10^{16}$ at.cm^{-2} and none is lost to the liquid phase. Figure 4.3 also depicts the total ^{16}O region thickness increasing monotonically as a function of anodization voltage, while maintaining its position on the surface. Ultimately, a $Ti^{16}O_2$/ $Ti^{18}O_2$ bi-layer structure is maintained; the $Ti^{18}O_2$ always remains at the interface with unoxidized metal and the $Ti^{16}O_2$ oxide region, which is always adjacent to the oxide/electrolyte interface.

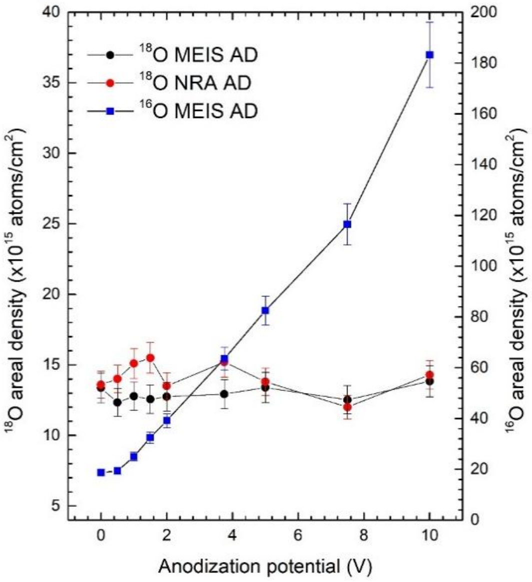

Figure 4.4: Variation in ^{16}O and ^{18}O areal density (AD) of the passive oxide as a function of anodization voltage. The areal density of ^{18}O from MEIS (black circles) is compared with the ^{18}O NRA (red circles) values.

Figure 4.5 depicts the linear relationship between formation potential and oxide thickness as derived from MEIS, using bulk densities. Given that the ^{18}O areal density remains constant, the linear increase in oxide thickness can only be explained by the increasing incorporation of ^{16}O which is evident from the MEIS spectra.

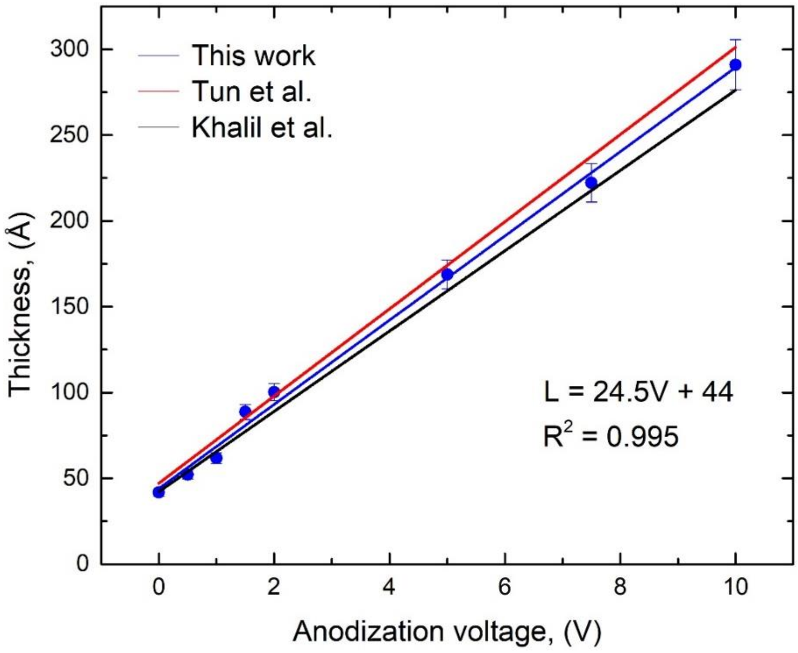

Figure 4.5: Growth of TiO_2 oxide as a function of anodization voltage. The blue line represents a linear least squares fit. The red line is from [23] and the black line from [24].

NRP was chosen as an alternative method of depth profiling ^{18}O. The ^{18}O areal densities measured with the $^{18}O(p,\alpha)^{15}N$ resonance are summarized in Figure 4.6. The same trends are observed as with MEIS, which can again be summarized by the anodic films maintaining a bi-layer structure, due to the transport of ^{18}O into Ti metal and oxide regions closer to the surface consisting entirely of $Ti^{16}O_2$. The resonance used is only sensitive to ^{18}O, so ^{16}O cannot be measured directly, but the existence of a $Ti^{16}O_2$ layer between the $Ti^{18}O_2$ and the film surface, is implied by there being no measured α intensity, when the 151 keV H^+ beam is incident on the surface. Increasing the incident beam energy such that the H^+ traveling through the near-surface oxide layer will lose energy inelastically, such that the required 151 keV is reached, upon the H^+ having reached the $Ti^{18}O_2$. This requires the multiplication of the energy loss specific to protons in TiO_2, known as its stopping power [25].

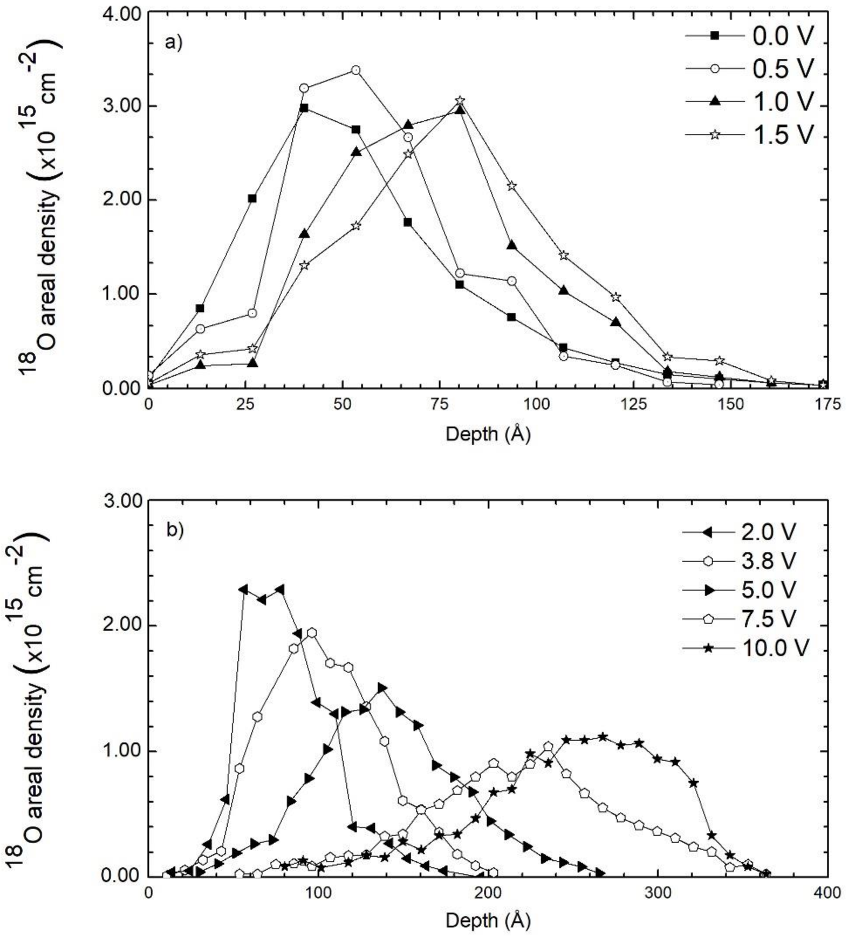

Figure 4.6: Nuclear reaction profiling data for the anodization voltages from (a) 0 - 1.5 V and (b) 2 – 10 V. Converting the energy scale to a depth scale is done by using the energy losses of H^+ in Ti oxide and converting counts into ^{18}O concentration through the use of a ^{18}O standard, depth profiles of ^{18}O can be determined.

Elastic recoil detection (ERD) spectra show no evidence of deuterium (D) incorporated in the TiO_2 layer. It should be noted that our ERD setup has a detection sensitivity of approximately 10 ppm (by number of atoms) [26] and therefore, it is possible that some undetected H or D remains in the film. XRD data showed the anodic oxide films that resulted from our processing conditions are highly amorphous, showing no sign of rutile or anatase (i.e. tetragonal phases).

4.4 Discussion

In their review of the properties of anodic Ti oxide, Vanhumbeeck and Poost, report that anodic TiO_2 films are usually reported to be initially amorphous and progressively crystalize into anatase structure [27] as they film thickness increases. However, the authors note that literature values for the voltage at which Ti crystallization occurs, are scattered over a "very wide range for different experimental conditions and even for apparently identical ones". They attribute this to a high sensitivity of the crystallization process to slight differences in Ti purity, crystallographic texture, surface conditions and to different sensitivities of the experimental techniques used to detect the onset of crystallization [9]. It is not surprising then, that studies can be found that lend support to the observations of this our XRD data showing the anodic oxide films that resulted from our processing conditions are highly amorphous, showing no sign of rutile or anatase (i.e. tetragonal phases). For example, Marsh et al. show using TEM that there is no evidence of crystallization below 10 V [28].

In Figure 4.3 and Figure 4.6, the MEIS and NRA ^{18}O profiles, appear to become increasingly wider for higher anodization voltages. For 0 V, the thickness of the ^{18}O region is ≈ 40 Å and has a maximum ^{18}O fraction of 0.4 at ≈ 30 Å, compared to the thickness of the 10 V sample's region, being ≈ 170 Å thick, with a maximum ^{18}O fraction of 0.15 at ≈ 295 Å. In the PDM, the Nernst-Plank equation describes the flux of vacancies under the influence of both migration in an electric field and diffusion. The broadening of the ^{18}O profiles may indicate the statistical effect of diffusion as a countervailing effect on migration which leads to oxygen profiles "spreading out".

Another significant effect, is that the interaction of the incident beam with the target media, is a stochastic process, and H^+ passing through a given thickness of TiO_2 will lead to the initially mono-energetic beam being “spread out”, in a Gaussian fashion (i.e. energy straggling). The thicker the $Ti^{16}O_2$ layer the H^+ must traverse before encountering $Ti^{18}O_2$ the higher statistical uncertainty in beam energy and therefore a greater amount of degradation in depth resolution, leading to a broadening effect of the depth profiles. For NRA and MEIS, the uncertainty in the ion beam incident energy is ± 0.2 keV. The product of the uncertainty in beam energy, with the energy loss of H^+ in this energy range (150-200 keV), translates into a depth uncertainty of about ± 10.7 Å. This may explain why for 0 – 1.5 V the NRA ^{18}O distributions appear wider than that predicted by the MEIS depth profiles and the slight differences in ^{18}O peak position and ^{18}O fraction between the two techniques. However, the peak ^{18}O positions are equal, given the uncertainties involved. For 2 – 10 V, the ^{18}O is distributed over wider ranges and the uncertainty in the depth scale is relatively less important in these samples given the larger depth they cover, although. Importantly, the integrated ^{18}O areal densities as measured by both techniques is equal within experimental uncertainties and constant over all anodization voltages (Figure 4.5).

There is agreement between the IBA techniques, in the broader trends related to the evolution of the oxide films. Both show that the ^{18}O layer is always adjacent to the unoxidized Ti metal. While the ^{16}O surface position remains unchanged, the width of this ^{16}O oxide layer grows monotonically as a function of voltage (Figure 4.4). According to MEIS, this $Ti^{16}O_2$ region increases from 10 Å at 0 V to 155 Å at 10 V. Overall, the oxidation state remains Ti^{4+} with a stoichiometry that could be described as $Ti^{16}O_{2-x}{}^{18}O_x$, where x will increase, with increasing depth into regions no longer containing ^{16}O isotope. Past this region of isotopic mixing or interface roughness region, there is a sub-oxide region that contains only ^{18}O which represents the furthest depth to which oxygen has been transported. In summary, the depth profiles indicate the existence of a bi-layer structure of the form: $Ti^{16}O_2/Ti^{18}O_2/Ti$.

According to the PDM, the ^{18}O that composed the original oxide will always be located adjacent to the Ti metal, because at the oxide/metal interface, an ^{18}O anion will react with a Ti ion from the metal substrate and create new oxide, while simultaneously creating an oxygen vacancy in the oxide's oxygen sublattice. Such a vacancy will be filled by ^{18}O anion adjacent to it, and subsequent fillings of the vacancy, will transport it to the oxide/electrolyte interface, where it will be consumed by ^{16}O anion from solution or an oxide region contain ^{16}O. Cation vacancies in the oxide's metal sublattice are created when Ti ions is ejected into the solution at the oxide/electrolyte interface, where it reacts with a ^{16}O ion from solution. The cation vacancies are transported to the metal/oxide interface by successive fillings and consumed when a Ti atom from the metal substrate fills it.

The observed evolution of the O profiles are not consistent with the HFM. The most simplified description of the HFM is of the original, ^{18}O containing oxide, simply acting as a passive medium that ions propagate through, transported down the potential gradient. Oxide growth according to the HFM happens at both the solution/oxide interface, due to Ti^+ transport, where it reacts with ^{16}O ions from solution, and oxide growth at the oxide/metal interface, due to ^{16}O anion transport where it reacts with metal in the metal substrate. The HFM predicts a "tri-layer" structure; $Ti^{16}O_2/Ti^{18}O/\ Ti^{16}O_2/Ti$, with three distinct phases. The only way which for the HFM predict the bi-layer structure is for the mobility of the oxygen ions to be zero ($t_O = 0$), with all oxide growth occurring due to Ti transport ($t_{Ti} = 1$). This is contrary to the observations of Khalil and Leach mentioned in the introduction, who concluded that $t_a = 0.65$ and $t_{Ti} = 0.35$ [24].

There have not been many studies that explore the depth profiling of O isotopes specifically to relate them back to the predictions of the PDM. However, Tun et al. studied the effect of anodization, in aqueous NaCl, of Ti electrodes (thin foils), with a pre-existing air-grown oxide, using *in-situ* neutron reflectometry (NR). It was shown that the resultant oxide could be divided into two distinct regions after anodization: an inner region with the same thickness and composition of the original air-grown oxide and an outer one containing significant amount of H (to which NR is very sensitive). This bi-layer structure lead the authors to suggest that the underlying growth mechanism that they preferred was the PDM [23].

Another important prediction of the PDM is that steady-state oxide thickness is a linear function of voltage under steady state conditions [29]:

$$L_{ss} = \frac{1-\alpha}{\varepsilon} V + B \tag{4.1}$$

where α is the polarizability of the solution/oxide interface, B is a constant that depends on pH and on rate constants for film formation and film dissolution, and ε is the mean electric field. The oxide thickness as a function of formation voltage is given in Figure 4.5. The slope of the line is often known as the "anodization ratio" which is given here as 24.5 ± 0.6 $ÅV^{-1}$. This is in agreement with 25.4 $ÅV^{-1}$ as determined by in-situ neutron reflectometry for Ti electrodes in aqueous NaCl solution. [23] and 23.4 $ÅV^{-1}$ determined by Khalil and Leach using α spectrometry [24].

4.5 Conclusions

High-resolution ion depth profiling with isotopic tracing was used to examine mechanism of titanium oxide growth. Ultra-thin Ti films were first exposed to $H_2{}^{18}O$ and then anodized in $D_2{}^{16}O$ resulting in a bi-layer structure with two distinct oxide regions, $Ti^{16}O_2/Ti^{18}O_{2-x}{}^{16}O_x/Ti/Si(001)$ for the entire range of anodization voltages (0 - 10 V), by medium energy ion scattering (MEIS) and nuclear reaction profiling (NRP). The outermost region, consisting of $Ti^{16}O_2$, is always adjacent to the oxide surface. While the $Ti^{18}O_2$ region grows directly into the Ti metal and contains all of the ^{18}O which composed the original passive oxide. The interpretation of these results requires the point defect model (PDM) as an explanation of the mechanism for oxide growth and is not consistent with the predictions of the HFM.

4.6 References

1. D.D. Macdonald, *Passivity–the key to our metals-based civilization.* Pure Appl. Chem., 1999. **71**: p. 951.
2. J. Lausma, et al., *Chemical composition and morphology of titanium surface oxides.* Mater Res. Soc. Symp. Proc. , 1986. **55**: p. 351.
3. E.P. Lautenschlager and P. Monaghan, *Titanium and titanium alloys as dental materials.* International Dental Journal, 1993. **43**: p. 245.
4. Matej Balazic, et al., *Review: titanium and titanium alloy applications in medicine.* International Journal of Nano and Biomaterials 2007. **1**: p. 1.
5. B. Kasemo and J. Lausma, *Biomaterials and implant materials: a surface science approach.* Int. J. Ora.l Maxillofac. Surg., 1988. **3**: p. 247.
6. X. Zhu, K. Kim, and Y. Jeong, *Anodic oxide "lms containing Ca and P of titanium biomaterial.* Biomaterials, 2000. **22**: p. 2199.
7. O.R. Camara, C.P. De Pauli, and M.C. Giordano, *Potentiodynamic behavior of mechanically polished titanium electrodes.* Electrochimica Acta, 1984. **29**: p. 1111.
8. T.M. Lee, E. Yang, and C.Y. Chang, *A comparison of the surface characteristics and ion release of Ti6Al4V and heat-treated Ti6Al4V.* J. Biomed. Mater Res., 2000. **50**: p. 499.
9. J.F. Vanhumbeeck and J. Proost, *Current understanding of Ti anodization: functional, morphological, chemical and mechainical aspects.* Corrosion Reciews, 2009. **27**: p. 204.
10. N. Cabrera and N.F. Mott, *Theory of the Oxidation of Metals.* Rep. Prog. Physics 1948. **12**: p. 120.
11. D.D. MacDonald, *The history of the Point Defect Model for the passive state: A breif review of film growth aspects.* Electrochimica Acta, 2011. **56**.
12. M.M. Lohrengel, *Thin anodic oxide layers on aluminium and other valve metals: high field regime* Materials Science and Engineering 1993. **11**: p. 243.
13. J. A. Davies, et al., *The Migration of Metal and Oxygen during Anodic Film Formation.* J. Electrochem. Soc., 1965. **112**: p. 675.
14. C.Y. Chao, L.F. Lin, and D.D. Macdonald, J. Electrochem. Soc., 1981. **128**: p. 1187.
15. D.D. Macdonald and M. Urquidi-Macdonald, *Theory of Steady-State Passive Films.* J. Electrochem. Soc., 1992. **139**: p. 3434.
16. N. Fairley, *CasaXPS*. 2013.
17. J. Kim, et al., *Depth profiling of ultrathin films using medium energy ion scattering.* Curr. Appl. Phys. , 2003. **3**: p. 75.

18. T. Nishimura, *MEISwin v. 1.0X* 2015.
19. A. R. Burke, et al., *Ignition mechanism of the titanium–boron pyrotechnic mixture.* Surface and Interface Analysis, 1988. **11**: p. 353.
20. D. Gonbeau, et al., *XPS study of thin films of titanium oxysulfides.* Surf. Sci., 1991. **254**: p. 81.
21. K.B. B. Siemensmeyer, W. Schultze, *XPS and Electrochemical Studies of Thin TiN Layers.* Ber. Bunsenges. Phys. Chem., 1991. **95**: p. 1461.
22. L. Wang, et al., *Local Fine Structural Insight into Mechanism of Electrochemical Passivation of Titanium.* Applied Materials and Interfaces, 2016. **8**: p. 18608.
23. Z. Tun, J. J. Noël, and D.W. Shoesmith, *Electrochemical Modification of the Passive Oxide Layer on a Ti Film Observed by In Situ Neutron Reflectometry.* Journal of The Electrochemical Society, 1999. **146**: p. 130.
24. N. Khalil and J.S.L. Leach, *He anodic oxidation of valve metals-i. determination of ionic transport numbers by a-spectrometry* Electrochimica Acta, 1986. **31**: p. 1279.
25. W.K. Chu, J.W. Mayer, and M.A. Nicolet, *Backscattering Spectrometry*. 1978: Academic Press Inc.
26. H.R. Verma, *Atomic and Nuclear Analytic Methods*. 2007: Springer Berlin Heidelburg.
27. J.F. Vanhumbeeck and J. Proost, *Current understanding of Ti anodization: functional, morphological, chemical and mechainical aspects.* Corrosion Reciews, 2009. **27**(3): p. 117.
28. J. Marsh and D. Gorse, *A photoelectrochemical and ac impedance study of anodic titanium oxide films.* Electrochimica Acta, 1998. **43**: p. 659.
29. D.D. MacDonald, *The history of the Point Defect Model for the passive state: A brief review of film growth aspects.* Electrochimica Acta, 2011. **56**

Chapter 5: *In situ* Rutherford backscattering spectrometry for electrochemical studies

5.1 Introduction

In many respects, our quality of life is dependent on advances in materials science and material performance is often adversely impacted by materials degradation. The costs of which are becoming increasingly expensive give how large many industries have become. The best example of materials degradation is corrosion, which effects nearly every sector of a modern economy, including the decreased functionality in the chemical processing industry, oil and gas transmission pipeline failures, and the increasing demand for safe and durable medical implants, etc. A recent study by the association of corrosion engineers (NACE 2016) estimates the annual global cost of corrosion consumes ~3.4% of a countries GDP (~$66B/year in Canada), ~35% of which would be saved by enacting proper corrosion control [1].

It is imperative to develop the best possible corrosion-resistant films to mitigate unwanted corrosion. Such corrosion resistance is predicated on a description of the fundamental mechanisms of oxidation at the level of individual atomic and molecular species and their transport mechanisms. To gain insight into such electrochemical processes on the atomic scale, it is necessary to create flexible, high-resolution, depth profiling techniques, which probe the fundamental constituents and describe their interactions with the greatest fidelity. Valve metals such as Ti are of special interest since, when exposed to oxygen rich environments, they spontaneously form oxides that are thermodynamically stable and highly insoluble, and hence provide excellent corrosion resistance in most corrosive media [2].

While some physical properties of the electrodes during oxidation can be inferred from electrochemical measurements themselves, many properties must be directly determined by *in situ* techniques, which probe the electrode under an applied electrostatic potentials. *In situ* experiments are challenging to design due to the liquid nature of the electrolyte. However, these *in situ* methods should (a) provide a range of surface compositional and structural information on a time scale that is commensurate with the electrochemical process, (b) must be compatible with geometric constraints of the process and the required temperatures and pressures. Ideally, they must also be non-destructive and have a high sensitivity. The developments of numerous *in situ* electrochemical diffraction and spectroscopic techniques [3-5] has expanded our understanding of the electrode-electrolyte interface. Techniques such as *in situ* X-ray diffraction (XRD) allow for the detection of crystalline phases [6], *in situ* Fourier-transform infrared spectroscopy (FTIR) [7] and *in situ* X-ray photoelectron spectroscopy (XPS) [8] can provide information on chemical bonding, and lastly *in situ* scanning tunneling microscopy (STM), can provide topographical information about electrodes surface [9].

As a complement to the abovementioned techniques, it is also important to determine depth distributions of key major and minor elements present in the electrode and at the electrode/electrolyte interface. Rutherford backscattering spectrometry (RBS) is a rapid, non-destructive technique that measures the energy and intensity of backscattered ions to convert this information into atomic areal density as functions of depth [10]. In RBS, a beam of mono-energetic ions is incident on a target sample, resulting in a small fraction (~ 0.01%) of those ions undergoing elastic collisions, due to repulsive Coulombic interactions with atomic nuclei. A fraction of these ions will backscatter in the direction of the detector, where the energy distribution of the backscattered ions is analyzed. For a given mass and energy of incident ion (M_1,E_0), the energy of each individual backscattered ion (E_1) is a function of the atomic mass of the target atom (M_2), the incident angle, and the detector geometry, relative to the incident angle (θ). From E_1 and conservation of energy and momentum, the mass of the target atom can be calculated, which is how RBS gains its elemental sensitivity. If an ion penetrates a depth (Δx) into a sample before backscattering, it will suffer inelastic energy loss, ΔE, due to electronic excitations. Similar processes occur along the ion's outward trajectory towards the detector. By converting the energy lost into a depth that an ion penetrated, we gain depth sensitivity. Given the well-defined energy loss, the mass sensitivity, and the linear proportionality between the backscattering intensity and the areal density of scattering centers in the target (accuracy up to 3-5%), RBS is useful for quantitative depth profiling, which yields elemental areal density as a function of depth [11]. RBS can be used to determine the average stoichiometry over a depth of several hundred nm, with a fair depth resolution (typically ~10 nm in the near surface region). This potentially allows for measurements of the areal density of elements in electrical double layers and near-surface layers of the electrodes used in anodization.

RBS requires pressures close to ultra-high vacuum (UHV), which may confound experimental interpretations, as transfer of the electrodes to UHV, from the ambient conditions, may result in compositional changes [12]. For example, the outermost layer may dehydrate, causing hydroxides to become oxyhydroxides and oxyhydroxides to become oxides [13]. For *in situ* RBS to be employed to study electrochemical interfaces under potentiostatic control, it must overcome the challenges of using a liquid electrolyte in UHV.

In situ RBS requires the use of an electrochemical cell that separates the liquid electrolyte from the UHV. This cell is placed in the UHV and incident ions penetrate through a thin Si or SiN window [14-17] to reach the metal electrode that has been deposited on the back of the window, and is in contact with the liquid electrolyte solution in the cell. By biasing the metal with respect to a reference electrode embedded in the cell, we make it serve as a working electrode to facilitate electrochemical reactions, such as anodization. During anodization, incident ions backscatter from the metal/oxide and oxide/electrolyte interfaces and pass back out through the window to reach the detector. Si and SiN windows are used due to their low-Z and well-established fabrication procedures using anisotropic chemical etching [18].

In situ RBS was originally demonstrated by Kotz et al. who used 2.5-3 MeV He^+ beams passing through ≈1.2 μm Si windows [15]. Kotz emphasized the need for low Z elemental windows to avoid overlap of the signal originating from the electrode/electrolyte interface and that originating from the Si window. In RBS, the probability of backscattering from an atom is known as the scattering cross section and is proportional to Z^2 of the target atom. If the elements of interest are of lower Z than Si (e.g. O), they will be obscured by the larger backscattering intensity of the substrate. Secondly, the authors [15] highlighted that due to the energy straggling incident ions will stochastically lose energy, resulting in a broadening of the monoenergetic beam and the consequent degradation in energy resolution. These challenges can be overcome by minimizing the low-Z window's thickness, or by using a single crystalline window through which the indecent ions can be channeled.

Other *in situ* RBS studies have been performed with different window thickness to study various electrochemical systems. Forster et al. studied deuterium ingress into ≈3.5 μm Zr films using nuclear reaction analysis (NRA) [19], and in another study used ≈1 μm thick Si windows to study electrochemical deposition of Pb, Ag, and Cu onto Si [16]. Morita et al. described an *in situ* RBS system for measuring the depth distribution of heavy nuclides desorption from SiO_2 at the surface of a 5.5 μm Si window used in their liquid cell [17]. Bouquillon et al. used *in situ* particle-induced X-ray emission (PIXE) with a 100 nm Si_3N_4 window and using a 3 MeV H^+ beam, in Pb-containing solutions, which were resolved to below 10 ppm [20]. Most recently, Hightower et al. did *in situ* electrochemical-RBS on 10 nm polycrystalline Au electrodes, using 2.3 MeV He^+ beams and a 150 nm thick Si_3N_4 window [21]. They reported the ability to measure the diffuse double layer, electrode surface and near surface regions, and upon negative potential they witnessed the formation of iodide layer and dissolution of the gold electrodes.

Most reported *in situ* backscattering designs incorporated Si windows with thicknesses between 1 and 3.5 µm. The thinnest window reported for *in situ* RBS, by Hightower et al., was 150 nm SiN. Given the complications outlined above related to the dimensions of the windows, it is imperative to minimize the thickness. The SiN windows used in this study are 100 nm thick to reduce the energy straggling and decrease its backscattering signal. Thinner SiN windows were not suitable for our studies due to poor mechanical strength and high failure rate. Additionally, most previous studies used much larger energies, between 2 and 3 MeV. This was necessary given the large thickness of the windows reported. The scattering cross section is proportional to E_0^{-2} and the 1 MeV and below energies used for *in situ* RBS, are advantageous to maximize the scattering cross sections and minimize the acquisition time for each consecutive RBS scan.

5.2 Experimental details

The design of the electrochemical cell for in situ RBS analysis is shown in Figure 5.1. Design drawings were created in Solid Works, and Western Physics and Astronomy Machineshop fabricated the cell. The area analyzed is limited by the dimensions of the He^+ beam, which is collimated by adjustable beam slits to 0.5×0.5 mm^2 or slightly smaller. The dimensions of the

SiN window were chosen to be the same size. The 0.5 × 0.5 mm^2, 100 nm thick SiN window, is centered on a 5 × 5 mm^2, 200 μm thick, Si wafer. The windows are commercially available from Norcada and manufactured using standard etching techniques. The SiN window must be thin enough to allow the He$^+$ to traverse it entirely with minimum energy straggling and thick enough to withstand the pressure difference between the electrolyte in the cell and the UHV. The window and surrounding components must be composed of low-Z elements to prevent their backscattering intensity from obscuring the signal from the elements in the films below them (i.e., the oxide, metal, and electrolyte).

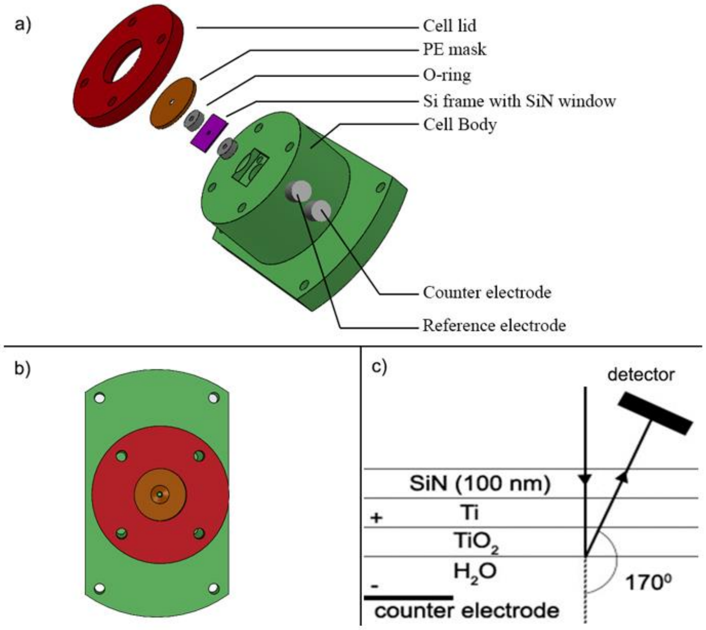

Figure 5.1: a) A 3D view of the unassembled electrochemical cell for *in situ* RBS. The Si frame with a 0.5 × 0.5 mm^2, 100 nm thick SiN window and a 60 nm thick layer of Ti deposited on it was centered inside the cell, b) the assembled view of the cell, from the top and c) the experimental geometry of the cell in the UHV system showing the direction of the incident ions (0^0), and the scattering angle ($\theta=170^0$).

The working electrode is a 40 – 60 nm Ti layer that is magnetron sputtered onto the SiN window and is easily replaced in each experiment. The cell body and lid were constructed from polytetrafluoroethylene (PTFE), because of its UHV compatibility and low-reactivity with potentially corrosive electrolyte. The liquid electrolyte solution is contained within the cell body and sealed by the first silicone O-ring. The Si wafer is placed between the first and second silicone O-rings to avoid clamping stress. The PTFE lid and polyethylene (PE) mask are screwed into the cell with sufficient pressure to seal the first O-ring without mechanically stressing or shattering the Si wafer. The PE mask was used as an aperture to further collimate the beam and prevent any contributions to the RBS spectra signal from the Si wafer. Electrochemical experiments typically employ three electrodes, with the Ti deposited on the window acting as the working electrode (WE), a Pt wire as the counter electrode (CE), and an AgCl-coated Ag wire as the reference electrode (RE). The RE and CE are embedded into the electrochemical cell body and sealed with Torrseal©.

To facilitate data interpretation for the functional cell, preliminary simulations of the expected RBS spectra of the assembled cell (SiN/Ti/H_2O) were conducted and are presented in Figure 5.2 (1 MeV He ions, an incident angle of 0^0, and detector $\theta = 170^0$). The presence of Cl and Na is due to their 0.3 mol/L concentration in the H_2O. Note that the cross section of H is too small for RBS to be sensitive to it. Before anodization (Figure 5.2a), 1 MeV He ions are sufficiently energetic to provide good separation between elements despite them having to pass through the entire 100 nm SiN window, to reach the Ti. There is a degree of overlap between the backscattering signal from N in the window and O in the electrolyte, but the ≈ 30 % larger cross section of O tends to dominate. In Figure 5.2b, 50 % of the Ti is oxidized and this is reflected in the movement of the low energy Ti edge position towards lower channels and a decrease in backscattering yield from Ti given its the lower stoichiometry in the oxide, since in RBS the intensity is directly proportional to the elemental areal density. The thickness of 60 nm of Ti was chosen as thicker Ti films would lead to more overlap between the Si signal in the window and the Ti signal from the oxide as it thickens and a thicker Ti layer leads to more energy straggling.

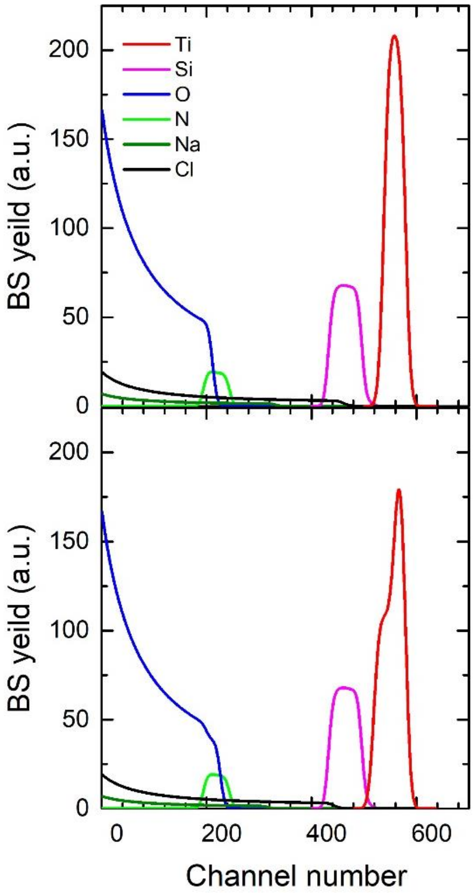

Figure 5.2: SIMNRA simulation of the expected RBS spectra associated with the assembled cell using 1 MeV He ions, incident angle of 0^0, and $\theta = 170^0$, a) before anodization and b) after 50 % of the Ti is oxidized.

The accelerator used to produce He^+ ions for RBS is the linear tandem accelerator at the Tandetron Lab at University of Western Ontario (1.7 MV High Voltage Engineering Europa). The backscattered He^+ energy distribution is measured with a surface barrier silicon detector (Ortec).

The detector is located at a scattering angle of $\theta = 170^\circ$ with respect to the direction of the incident beam, in "Cornell" geometry. The energy resolution of the detector is 12 keV with a detector aperture of 2.0 mm × 6.1 mm. Simulated RBS energy distributions where generated using SIMNRA 6.06 [22]. The ion dose (μC) is measured using a Faraday cup, which is moved periodically (1 s for every 4 s interval) to block the beam and probe the ion beam current. A high-precision 4-axis manipulator allows for x-y translations of the samples in the RBS chamber within ± 0.05 mm. Consecutive x-y RBS scans were used to align the beam normal to the SiN window surface. Potential differences were applied and currents measured with an AFCBP1 bipotentiostat (Pine Instrument Company).

5.3 Results

Figure 5.3a shows the evolution of the RBS spectra when the Ti was biased at +2 V with respect to the Ag/AgCl RE, using a 0.3 mol/L NaCl electrolyte. The bias was constantly applied while collecting RBS data. Individual RBS spectra were acquired using a 1 MeV He^+ beam, with a total dose of 0.25 μC per spectra. Given fluctuations in the beam current, the acquisition times varied between 5-6 min (300-360s) per spectrum. The vertical dashed lines represent the high energy edge position of the indicated element, which corresponds to the depth into the target that that element is initially found before bias is applied. For example, for Ti this would be the Ti/SiN interface, at channel 560. In RBS, the width of the spectral feature is linearly proportional to the physical thickness of the film and so the width of the Ti peak is consistent with deposited Ti film thickness.

Note that the O intensity from the electrolyte is lower than what is predicted by Figure 5.2. This may be due to the cell reservoir not being completely filled completely with the liquid electrolyte. When it is fixed upright to the sample holder, the beam might be incident on the some of the empty volume, which would lead to a decrease in O intensity. Alternatively, the incident beam may not be perfectly aligned with the Ti/SiN (and the electrolyte behind it), which would also lead to reductions in O intensity from the bulk. Evidence for the latter possibility will be presented in the discussion section.

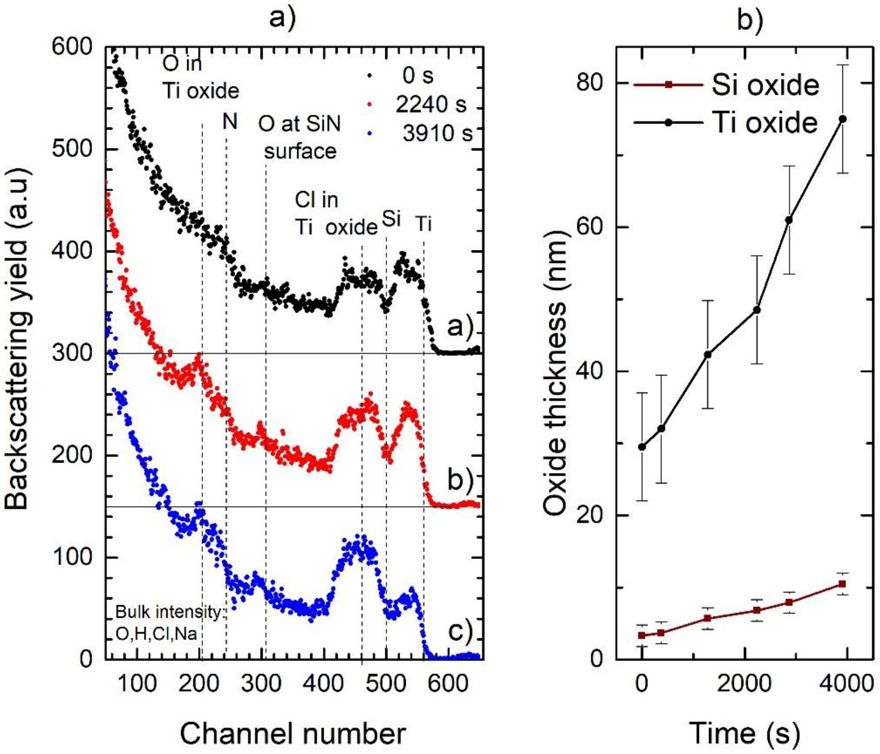

Figure 5.3: a) The time evolution of RBS spectra acquired with 1 MeV He^+, when Ti is biased a +2 V, for the times: a) 0 s (before bias), b) 2240 s, c) 3910 s. Horizontal lines represent the vertical offsets and dashed vertical lines represent the channel corresponding to the indicated

element’s initial edge position before voltage is applied, b) oxide thickness as a function of time for the Si oxide growing at the SiN surface and the Ti oxide growing on the Ti electrode.

Experimental RBS spectra are convolutions of individual elemental spectra. By fitting the spectra in Figure 5.3 using SIMNRA, the contributions from each individual element can be isolated. Breaking the target into a series of sublayers, whose composition and thickness can be controlled, allows one to simulate RBS spectra, until the simulated and experimental spectra match. In Figure 5.4, the depth profiles used to simulate the RBS spectra for the times a) 0 s, b) 2240 s, and c) 3911 s are shown and the resultant time evolution of the Cl, O and Ti elemental spectra are presented in Figure 5.5. In Figure 5.4, the break in the horizontal axis was included because this is the location of SiN, where the concentration of the indicated elements is zero. The O profile at the surface is part of a SiO_2 layer at the surface of the SiN and the O at greater depths represents the growing TiO_x layer.

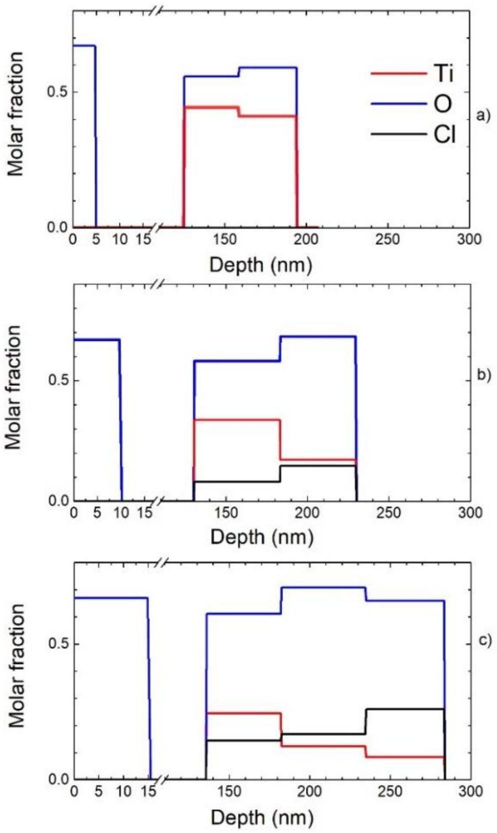

Figure 5.4: The depth profiles used to simulate the spectra in Figure 5.3: a) 0 s, b) 2240 s, c) 3911 s. The black line corresponds to Cl, the red to Ti, and the blue to O molar fraction. The depth axis has different scales before and after the break. The resultant individual elemental RBS spectra derived from these profiles are presented in Figure 5.5.

In Figures 5.3 – 5.5, the characteristic signs of Ti anodization (oxidation) can be observed in a sequence of RBS spectra. From 378 s to 2240 s, there is a reduction in Ti intensity around channel 520 and below. The RBS backscattering yield is linearly proportional to the number of scattering centers of a given element exposed to the beam, so the drop in Ti intensity corresponds to oxide growth, as the Ti areal density is lower in the oxide than in metallic Ti. Figure 5.5d shows that the total integrated Ti areal density remains relatively constant, indicating no significant Ti dissolution into the electrolyte solution (the lower Ti AD at longer time scales will be addressed later). There is a concomitant increase in O at channel 200, corresponding to the same Ti oxide growth at the metal/oxide interface.

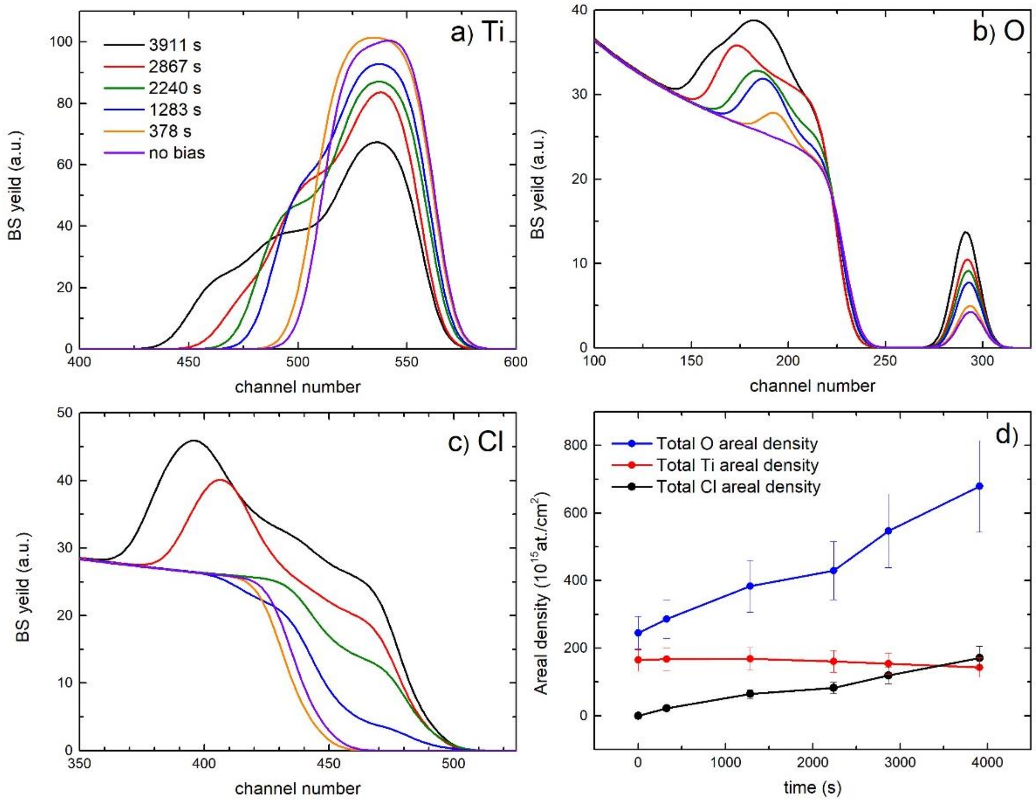

Figure 5.5: The time evolution of the spectra of individual elements a) Ti, b) O, and c) Cl, for the period 0 s - 3911 s, after simulating data with SIMNRA [22], d) shows the total areal density of each element as a function of time.

From 2240 s to 3911 s, the growth of the O feature appears to increase to both higher (~290) and lower channels (220 and below). It is possible this represents oxide growth, in two directions: from the metal/oxide interface into the metal and from the oxide/electrolyte interface outwards. Alternatively, this may represent growth at the metal/oxide interface alone. This is because, when Ti metal is converted into oxide, the volume of oxide is greater than the volume of metal consumed and such a volume expansion will result in movement of the oxide/electrolyte interface outwards into the space that was originally occupied by the solution, despite no growth having occurred at the oxide/solution interface. The Pilling-Bedworth ratio (PBR) is the ratio of the volume of the oxide created and the volume of metal consumed and for Ti is ~1.7, depending on allotrope. Both scenarios are consistent with the evolution of Ti, which is distributed over increasingly wider depths (towards lower channels relative to its positions at 330 s) as metallic Ti is consumed to form oxide.

With no bias applied, the passive oxide is free of chlorine but at 1283 s, the presence of Cl in the oxide adjacent to the Ti metal, can be clearly observed and it increases monotonically over time. At 3911 s the Cl is distributed throughout the entire Ti oxide film with the highest concentration in the region adjacent to the oxide/solution interface. Growth of the oxide layers both at $H_2O/TiO_2/Ti$ interfaces and SiN/SiO_2/vacuum regions will be discussed in detail in the discussion section below.

In order to see what changes might occur in the films upon their transfer from ambient conditions to vacuum, the *in situ* oxidized sample was removed from the cell and measured with RBS with TiO_2 layer facing the beam, using 2.5 MeV He^{++}. Higher energy was selected to separate Ti and Cl peaks. Figure 5.6a displays the *ex situ* RBS spectrum of an as-deposited 60 nm Ti film on 100 nm SiN and Figure 5.6b is the spectrum of the anodized Ti. Note that the orientation of the Ti/SiN layers with respect to the incident beam was reversed for these spectra compared to those shown in Figure 5.3 – 5.5. Figure 5.6 c) shows the same experimental data as in b) but plotted with the simulated spectrum used in fitting the *in situ* spectrum from 3911 s, using the same experimental parameters as in a) and b).

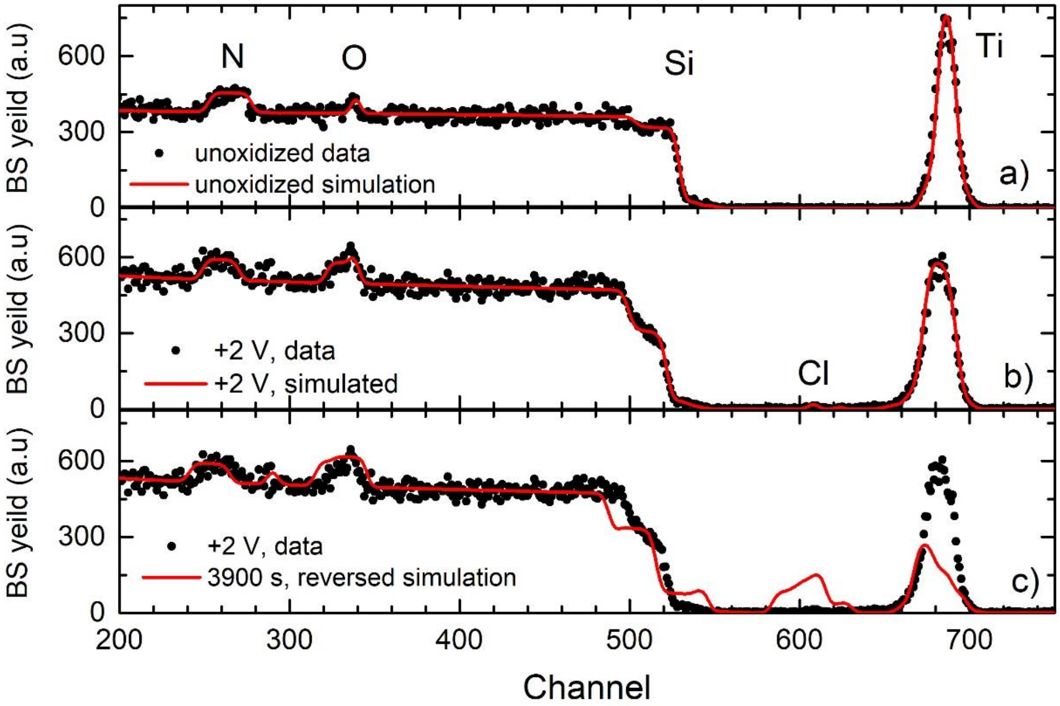

Figure 5.6: RBS spectra acquired with 2.5 MeV He^+ on a) unoxidized 60 nm Ti, b) the Ti oxide film that resulted from being anodized at +2 V, and c) the same experimental data as in b) but overlaid with the simulated *in situ* spectrum (with layers in reversed order) after 3911 s.

5.4 Discussion

Mechanism of Ti anodization

As mentioned above, it is not possible from the RBS data to determine if the oxide growth is happening at the oxide/metal interface alone, or both the oxide/metal and oxide/solution interfaces simultaneously. Additionally, even if we could determine which of these options was operative, we would still be unable to distinguish between the proposed growth mechanisms such as the high-field model (HFM) vs. the point defect model (PDM), as each of them describe oxide growth occurring at both interfaces simultaneously. However, the main conclusions of Chapter 4 is that the O elemental depth profiles, as measured using NRA and MEIS, of anodic Ti oxide films, created using the $^{16}O/^{18}O$ isotopic labeling given in that chapter, resulted in $Ti^{16}O_2/Ti^{18}O_2/Ti$ bi-layer structures, that were predictions of the point defect model (PDM). This allows us to interpret the changes in the *in situ* RBS spectra of the Ti films during anodization, as depicted in sequential RBS spectra (Figure 5.3 and 5.5), as consistent with the predictions of the PDM [13].

Recall that the PDM describes anodization in terms of the continual generation of cationic and anionic defects, their field driven flux (i.e. migration and diffusion) across the existing oxide, and subsequent consumption at the opposite interface. When O at the metal/oxide interface reacts with the Ti metal to form oxide, it creates a vacancy in the O sublattice that must be filled by an O atom immediately adjacent to it, which again results in the O vacancy propagating towards the oxide/electrolyte interface, where it is consumed by an anion from the solution. Likewise, Ti cations are transported from the metal/oxide interface to the oxide/electrolyte interface where they are ejected into the solution and react with anions in the electrolyte to form a precipitated oxide outer layer. The ionic flux results in oxide growth at both interfaces simultaneously and the position of these interface is constantly changing, relative to the laboratory frame of reference.

In Figure 5.5b, the O spectra grow towards both higher and lower channels suggesting oxide growth, relative to the initial oxide/electrolyte interface at 0 s, both into the metal and outwards into the solution. According to the PDM, the former growth is due to the anionic vacancy flux and the latter due to the cationic vacancy and interstitial flux. The changes in the Ti spectra in Figure 4a towards lower energies is consistent with Ti transport towards the oxide/electrolyte interface.

Figure 5.5c, shows that before a bias is applied, the initial passive oxide is free of Cl. There is only backscattering from the Cl in the electrolyte (Cl bulk signal begins at channel 440). At 387 s, despite oxide growth having occurred, the oxide film is still free of Cl. At 1283 s, the presence of Cl can be seen in the oxide and Cl molar fraction increases monotonically to 0.12 at 2240 s and reaches 0.14 at 3911 s in the oxide layer directly adjacent to Ti metal. At 3911 s, the outermost layer adjacent to the oxide that has a Ti molar fraction of 0.08 and Cl molar fraction of 0.26, suggesting not an oxide region, but (partly) an aqueous phase given the very low Ti areal density. The movement of the Cl edges to both higher and lower channels suggests that in addition to O anions, Cl may be mobile species as well and its transport would be described by its respective vacancy flux according to the PDM.

However, there is a competing explanation for Cl incorporation. Wood et al. developed a model describing the incorporation of anions from the electrolyte in a growing anodic oxide and their possible migration with the film [23]. The model was developed for anodic alumina films but its underlying assumptions are sufficiently general that it should apply to oxides of other metals, like Ti [24]. According to Wood et al. individual monolayers of oxide are added at a constant rate at the oxide/electrolyte interface. This oxide is formed by transport of Ti^{4+}ions to this interface and their field-assisted ejection into the electrolyte where they react with anions in solution. For each new monolayer that forms, it is assumed that all the adsorbed electrolyte anions in the double layer are consumed within the monolayer and replaced immediately by new anions absorbed on the newly created oxide's surface. Notably, the process can occur without breaking Ti-O (or Ti=O) bonds. Electrolyte species tend to be immobile or migrate at a constant rate in the region of the oxide film formed by precipitation (it is possible Cl^- are migrating inwards given the direction of the bias). Given specific anodizing conditions (pH, etc.), the rate of migration for an ionic spices tends to be constant and in general tends to migrate slower than oxygen anions (O^{-2}/ OH^-). Note that give the direction of the bias, we would not expect to see Na^+ in the oxide as we do with Cl^-.

Given the limitations of RBS's depth resolution, it is difficult to fully determine the structure of the electrode in greater detail. The Cl peak overlaps with the signal originating from the Si in the SiN window and this is made even worse at longer time intervals, as there is additional overlap with the signal from Ti, as it shifts to lower energies, during oxide growth. Ultimately, it is difficult to determine how the Cl high energy edge changes and the depiction of it moving towards higher channels, as in Figure 5c, might be inaccurate, and it might be immobile. This means it is not possible to determine if Cl participates in the vacancy mechanism that underlies the PDM, just as oxyanions do, or if it is being incorporated during multilayer formation (then migrating inwards interstitially).

The RBS spectrum of the unoxidized sample in Figure 5.6a was fit by an integrated Ti areal density of $(2.5 \pm 0.1)\times10^{17}$ atoms/cm^2, and that of the anodized sample in Figure 5.6b was fit by an integrated Ti areal density of $(2.7 \pm 0.1)\times10^{17}$ atoms/cm^2. They agree within 9%, which is lower than the uncertainty associated with the areal density (10%). However, the *in situ* Ti RBS spectra in Figure 5.4a were fit with $(1.7 \pm 0.1)\times10^{17}$ atoms/cm^2 at 378 s, which decreases to $(1.4 \pm 0.1)\times10^{17}$ atoms/cm^2 at 3911 s. As shown in Figure 5.6c, this is a significant reduction in Ti areal density relative to the *ex situ* RBS. Much of this difference might be due to an imperfect alignment of the 0.5×0.5 mm^2 SiN window with respect to the incident beam when the cell is assembled. If the beam is not properly aligned to the SiN window and the Ti deposited on it, the Ti intensity will be adversely effected. The spectra in Figure 5.5a and 5.5b were taken with a beam incident on Ti which had been deposited over the entire 5×5 mm^2 SiN surface and as such suffer no alignment problem.

Ion beam exposure effects

Prior to applying an electrochemical bias to the Ti, RBS was performed to determine if exposure of the ion beam alone lead to compositional changes. As can be seen in Figure 5.7a, apparent movement of the high energy Ti and Si edge positions to lower channel numbers (~10-15 channels) and slight reductions in Ti intensity (~20-25%) were observed. The magnitude of these effects was proportional to the total acquisition time. Notably, after the ion beam was removed from the surface for a sufficiently long time, the original spectrum (without shifts) can be reproduced, which is shown in Figure 5.7b.

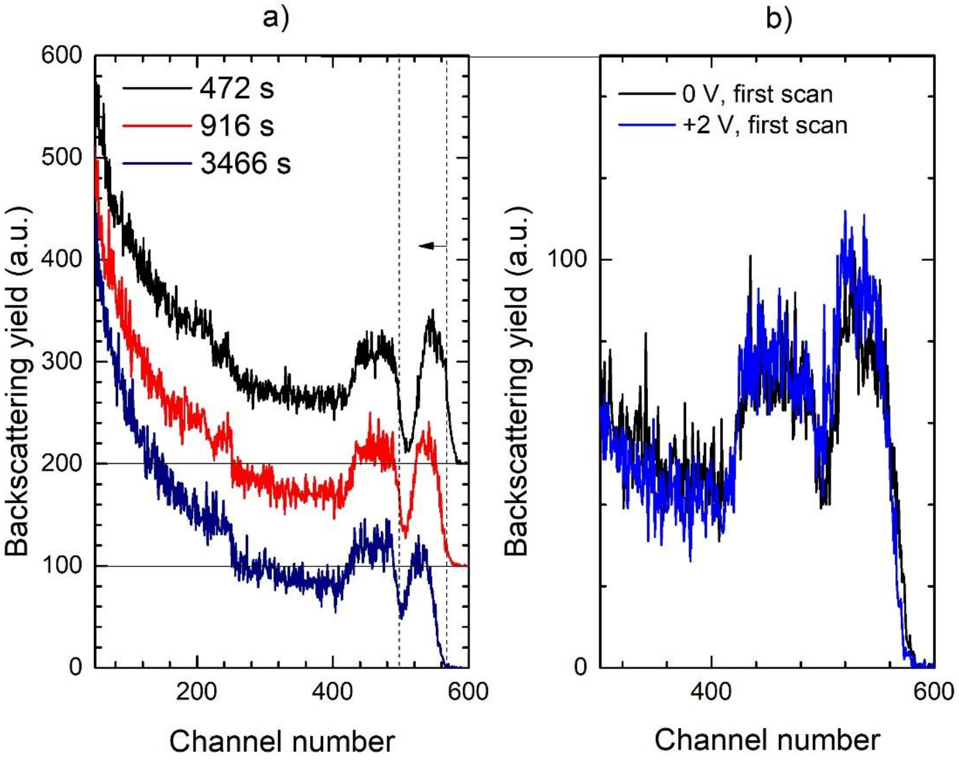

Figure 5.7: a) RBS spectra taken with no bias applied showing the effects of beam exposure for times 472 – 3466 s. The difference between the position of the Ti feature in the initial and file spectra is ~15 channel and ~20% reduction in intensity, b) The effects “resetting” after waiting a ~10 min between the finial RBS scan with no bias, and the 1st scan with bias.

A possible explanation to the observed phenomena is charge accumulation on the surface of the cell. Given the insulating components of the cell, if a sufficiently large number of positive charges accumulate and establish an electric field, this would repel incident ions and they would experience energy loss before backscattering, resulting in about an apparent shift in the kinetic energy. However, given the E^{-2} dependence of the differential scattering cross sections in RBS, a lower energy of incident ions might be expected to increase backscattering intensity. Nor would it explain why only Ti seems to be effected. Alternatively, the formation of a SiO_2 layer at the Ti/SiN interface or some restructuring of this interface, induced by beam exposure, would explain the movement of the Ti edge toward lower channels and the fact that it impacts only the Ti features. This is perhaps unlikely since the effect would have to be reversible.

Role of electrolyte anions (chlorine)

During anodization, there appears to be more Cl present in the oxide than was observed *ex situ* RBS. Even if the Cl content is overestimated, for reasons discussed above, exposure of oxide film to ambient environment and UHV results in significant Cl loss. Figure 5.6b only has a Cl molar fraction of 0.05 in the first 27.5 nm of the oxide. The loss of Cl may support the claim that the Cl is incorporated in the oxide without breaking Ti-O bonds as discussed above. The Ti-Cl bond dissociation energy is 507 kJ/mol and that for Ti-O is 673 kJ/mol, which explains why Ti-O would preferentially be formed in the first place. Even if Ti-Cl bonds are forming, it is favorable to convert Ti chloride to TiO_2 via hydrolysis:

$$TiCl_4 + 2H_2O \rightarrow TiO_2 + 4HCl \tag{5.1}$$

SiN oxidation

According to the RBS spectra in Figure 5.3, there is a spectral feature around channel 303 that grows monotonically over time and whose high energy edge position remains unchanged. From the depth profiles in Figure 5.4, this was simulated as O in SiO_2 at the SiN surface. The thickness of this layer increases from 5.0 nm with no bias to 15.5 nm at 3911 s using 80 % SiO_2 bulk density. From our additional ex situ RBS measurements of the anodized film (Figure 5.6c) the O peak corresponding to this 15.5 nm of SiO_2 can be observed and well accounted for by this surface oxide. Additionally, the stoichiometry and thickness of the SiN layer used to simulate the spectra in Figure 5.4 remained constant over time and thus shows no evidence of the transport of O through it towards the SiN surface, although it would not be obvious for very small O concentrations.

It has been reported that through anodization, SiN can be converted into SiO_2 via the reaction [25]:

$$6O^{2-} + Si_3N_4 \rightarrow 3SiO_2 + 2N_2 + 12e^- \tag{5.2}$$

If one assumes this reaction can be used to describe the SiO_2 layer growth at the surface, the O cations at the surface need to be at a lower potential than those deeper into the film. It is more feasible that O in this instance would likely need to impinge the surface of the SiN, from vacuum. The impingement rate for H_2O in the UHV can be calculated by:

$$Z = \frac{P}{\sqrt{2\pi k_B T m}} \tag{5.3}$$

where k_B is Boltzmann's constant and m is the mass of the molecular species in the vacuum. For H_2O at 300 K and pressure of 1.33×10^{-4} Pa (10^{-6} torr) and assuming a sticking coefficient of $\alpha = 0.1$, the rate at which water molecules adhere to our surface is 4.8×10^{13} $cm^{-2}s^{-2}$. A 29 nm thick

SiO_2 layer has 2.0×10^{17} O atoms which given the calculated sticking rate would require 4.2×10^{3} s to accumulate. The elapsed time was ~ 90 % of that required time. However the sticking coefficient is probably overestimated. It is also possible that the local pressure could be much higher in the presence of a microscopic leak around the location of the window.

Figure 5.8 is a schematic representation of the proposed transport of Ti, O, and Cl during anodization. The Ti oxide growth happens at two locations simultaneously due to the cationic and anionic vacancy flux, with Δx_1 growth due to O transport into the metal and Δx_2 the result of Ti transport and ejection into the electrolyte (in general $\Delta x_2 \neq \Delta x_1$). During the creation of Δx_2, Cl will be incorporated into the oxide and migrate inward until it can be found throughout a depth of Δx_3. The growth of the SiO_2 at the SiN surface is probably due to an analogous process as Δx_1, where O at the oxide/SiN interface reacts with SiN to from SiO_2 via Reaction 1.

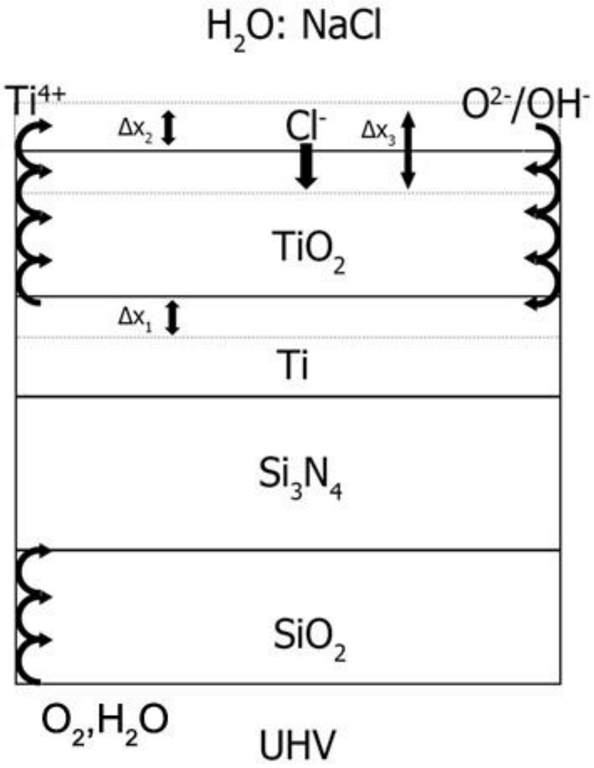

Figure 5.8: Schematic showing the proposed Ti, Cl, and O transport during anodization.

Considerations of cell design

The key feature to improve the existing cell design would be to minimize the SiN window thickness. The 100 nm thickness of SiN was chosen as a compromise between preventing large amounts of energy straggling and related degradations in depth resolution, and being thick enough to prevent rupturing in vacuum. If this technique is to be brought to maturity, it would be worth testing, in a systematic fashion, SiN windows of decreasing thickness, to see what the physical limit is in terms of maximizing the window area and minimizing the window thickness. With a smaller thickness of SiN than what is used in the current investigation (50 nm vs 100 nm for example), one will get better separation of the Ti and Si features, as the Ti features shift towards higher energies due to less inelastic energy loss, as the ions penetrate through the window. It would also be conducive to resolving the Si and Cl as separate features as wells. One of the main interpretative challenges to analyzing the data presented in this study, was the overlap between Si, Cl, and Ti (on longer timescales).

Alternatively, it may be possible to use a thin crystalline Si window that the incident ions could be channeled though, leading to reductions in backscattering intensity from the window. If properly done, this would prevent large overlap between the backscattering intensity from the window and from the Ti metal deposited on it.

More speculative solutions might be to consider creating lower-Z windows such as those composed of graphene. Graphene has excellent mechanical properties and so very thin windows would still be capable of withstanding the pressure difference required. If graphene proves intractable, it might be possible to use ultra-thin films of diamond-like carbon (DLC), deposited on Si to act as windows. A window composed of elements of lower-Z than Si is advantageous, since in RBS, the scattering cross section has a parabolic dependence on Z, and the backscattering intensity from such windows would be smaller. Additionally, the kinematic factor is lower as well, which shifts the spectral features to lower energies, away from the Cl and Ti features. However, the right experimental parameters need to be taken into account to avoid overlap of the backscattering signal from C, with low-Z elements relevant to the electrochemical reactions, namely O.

Chapter 6 provides some arguments about how similar electrochemical cell designs can be utilized for *in situ* medium energy ion scattering (MEIS), to harness the superior depth resolution of the technique to study the electrodes and the electrode/electrolyte interfaces and their evolution. Given the stopping cross sections of protons at these energies (50-200 keV) is maximized, the viability of this approach will largely depend on minimizing the window thickness.

Besides considerations related to the dimensions of the window, another improvement to the current design would be, rather than sealing the Si frame (with the centrally located SiN window) between two O-rings, a better design would be to epoxy or affix the Si frame to a "holder", which could be screwed directly into the cell body. This would accommodate a single larger (close to the diameter of the cell), O-ring to improve the seal and completely prevents clamping stress on the Si frame. Excessive clamping stress can cause the wafer to shatter or lead to ruptured windows. The Si wafers could be removed from the holder after the experiment and a new one affixed in place.

Improvements could be made by designing permanent feedthroughs for the Pt RE and AgCl/Ag RE so they could easily be replaced. The current design involved sealing the electrodes with vacuum epoxy, which makes them difficult to replace without damaging them, especially given how thin the wires or how fragile the AgCl films are. Worse, the KCl electrolyte solution used to store the AgCl/Ag RE corrodes the epoxy that seals it and can lead to leaks. It would be advantageous to have a RE that could be removed and stored in the electrolyte separately.

5.5 Conclusion

An electrochemical cell has been designed, tested and constructed using a 100 nm SiN window and a deposited 60 nm-thick Ti electrode layer. Upon biasing the Ti with respect to the Ag/AgCl RE at +2 V in a 0.3 mol/L NaCl solution, characteristic features of anodization are observed in a series of RBS spectra taken over time. The time evolution of the Ti and O depth profiles appears consistent with the PDM, while Cl incorporation most likely happens during the formation of oxide multilayers that result from precipitation at the oxide/electrolyte interface. There are compositional differences in between the films observed by *in situ* and *ex situ* measurements. The Cl concentration in the films observed by *in situ* measurements much higher than that was seen in *ex situ* RBS measurements following anodization, implying Cl loss when exposed to UHV. Reductions in expected Ti intensity were observed and explained in terms of poor alignment of the cell with respect to the ion beam and possible charge accumulation.

5.6 References

1. E. Bowman, *International measures of prevention, application, and economics of corrosion technologies study*. 2016, NACE International
2. J. Lausma, et al., *Chemical composition and morphology of titanium surface oxides.* Mater Res. Soc. Symp. Proc. , 1986. **55**: p. 351.
3. J.H. White, et al., *surface extended x-ray absorption fine-structure of underpotentially deposited silver on Au (111) electrodes.* J. Phys. Chem., 1988. **92**(15): p. 4432.
4. V.R. Stamenkovic, et al., *Surface chemistry on bimetallic alloy surfaces: Adsorption of anions and oxidation of CO on* $Pt_3Sn(111)$*.* Journal of the American Chemical Society, 2003. **125**(9): p. 2736.
5. X.F. Lin, B. Ren, and Z.Q. Tian, *Electrochemical and surface-enhanced Raman spectroscopic studies on the adsorption and electrooxidation of C-1 molecules on a roughened Rh electrode.* Journal of Physical Chemistry B, 2004. **108**(3): p. 981.

6. J. Wang, et al., *In situ x-ray-diffraction and -reflectivity studies of the Au(111)/electrolyte interface: Reconstruction and anion adsorption.* Physical Review B, 1992. **46**: p. 10321.
7. G. Lefèvre, *In situ Fourier-transform infrared spectroscopy studies of inorganic ions adsorption on metal oxides and hydroxides.* Advances in Colloid and Interface Science, 2004. **107**: p. 109.
8. T. Fujii, et al., *In situ XPS analysis of various iron oxide films grown by NO2 assisted molecular-beam epitaxy.* Physical Review B, 1999. **59**: p. 3195.
9. K. Itaya, *In situ scanning tunneling microscopy in electrolyte solutions.* Progress in Surface Science, 1998. **58**: p. 121.
10. W.K. Chu, J.W. Mayer, and M.A. Nicolet, *Backscattering Spectrometry*. 1978: Academic Press, Inc.
11. C. Jeynes, et al., *Accurate RBS Measurements of the Indium Content of InGaAs Thin Films.* Surface and Interface Analysis, 1997. **25**: p. 254.
12. E. Yeager, *Non-traditional approaches to the study of solid-electrolyte interfaces: Problem overview.* Surf. Sci., 1980. **101**: p. 1.
13. D.D. MacDonald, *The history of the Point Defect Model for the passive state: A breif review of film growth aspects.* Electrochimica Acta, 2011. **56**: p. 1761.
14. A. Hightower, B. Koel, and T. Felter, *A study of iodine adlayers on polycrystalline gold electrodes by in situ electrochemical Rutherford backscattering (ECRBS).* Electrochim. Acta, 2009. **54**: p. 1777.
15. R. Kotz, et al., *in situ Rutherford backscattering spectroscopy for electrochemical interphase analysis.* Electrochim. Acta, 1986. **31**: p. 169.
16. J.S. Forster, et al., *Ion backscattering studies of the liquid-solid interface.* Nuc. Inst. & Meth. Phys. B 1987. **28**: p. 385.
17. K. Morita, et al., *An in situ RBS system for measuring nuclides adsorbed at the liquid-solid interface.* Radiation Physics and Chemistry 1997. **49**: p. 603.
18. K.E. Bean, *Anisotropic etching of silicon.* IEEE Transactions on Electron Devices, 1978. **25**: p. 1185.
19. J.S. Forster, et al., *in situ NRA studies of hydrogen ingress into Zr-2.5 wt.% Nb at the liquid-solid interface.* Nuc. Inst. & Meth. Phys. B, 1991. **56**: p. 821.
20. A. Bouquillon, et al., *In situ dynamic analysis of solids or aqueous solutions undergoing chemical reactions by RBS or PIXE with external beams.* Nuc. Inst. & Meth. Phys. B, 2002. **188**: p. 156.
21. A. Hightower, B. Koel, and T. Felter, *A study of iodine adlayers on polycrystalline gold electrodes by in situ electrochemical Rutherford backscattering (ECRBS).* Electrochimica Acta, 2009. **54**(6): p. 1777.
22. M. Mayer, *SIMNRA User's Guide, www.simnra.com*. 1997.
23. G. C. Wood, et al., *A Model for the Incorporation of Electrolyte Species into Anodic Alumina.* J. Electrochem. Soc., 1996. **143**: p. 74.
24. J.F. Vanhumbeeck and J. Proost, *Current understanding of Ti anodization: functional, morphological, chemical and mechainical aspects*. Corrosion Reciews, 2009. **27**: p. 204.
25. L. Zhang, *Kinetics of passive film growth and the segregation of alloying elements in passive systems*. 1995, The Pennsylvania State University.

Chapter 6: Conclusions and future work

The properties of surface layers, interfaces, and ultra-thin films are markedly different than the properties of the bulk material. The creation of these structures is performed with deposition and materials modification techniques that have a wide adoption and so their precise characterization is often necessary. The techniques of ion beam analysis (IBA) allow for a quick and non-destructive way to determine film thickness and elemental composition as a function of depth. In this work, medium energy ion scattering (MEIS), has been employed to quantify the energy loss experienced by incident ions as they penetrate elemental and compound targets. MEIS, nuclear reaction profiling (NRP), and Rutherford backscattering spectrometry (RBS) have been used, to preform both *ex situ* and *in situ* measurements, to elucidate the mechanisms of anodic titanium oxide growth.

The ion beam analysis techniques MEIS and NRP utilize protons in the medium energy range (50-200 keV). Accurate estimates of the energy loss of protons, are a necessary precondition for precise quantitative depth information. The stopping cross sections (SCS) of protons in compounds in this energy range often show deviations from the commonly accepted additive “Bragg’s rule” calculations and often there exists no experimental SCS for many thin-film compounds.

In Chapter 3 of this thesis, the SCS of protons in the medium energy range were measured accurately using an iterative numerical calculation (Appendix A), for several ultra-thin films. The SCS of protons for elemental Ti and Si films appear to be accurate for the energy range 50–170 keV within experimental uncertainties, when compared to SRIM and PSTAR semi-empirical fits, as well as existing experimental data. This provides strong validation that the method for measuring the SCS from MEIS spectra is accurate.

Experimentally determined SCS of protons in TiO_2 were systematically lower (≈14%) when compared to SRIM predictions at stopping power maximum and shifted slightly towards higher energies: 18.4 eV $cm^2/10^{15}$ atoms at 99.6 keV. Rearranging Bragg's rule to get:

$$\varepsilon_O = \frac{3}{2}\left(\varepsilon_{TiO2} - \frac{1}{3}\ \varepsilon_{Ti}\right) \tag{6.1}$$

We experimentally obtained SCS of O that better predict the value of the stopping maximum and energy at which it occurs, when used in Bragg's rule calculations of protons in $SrTiO_3$ when compared to previously existing experimental data by Dedyulin et al. [1]. The results lend strong support to the idea that physical effects are responsible for deviations from Bragg's rule in compounds such as TiO_2 and $SrTiO_3$. This occurs when the SCS of O measured when O is in a gas phase and not in the condensed phase of the current context. Our experimental SCS of Ti, Si, and TiO_2 have been incorporated into the Nuclear Data Section of the IAEA's "Stopping Power of Matter for Ions" database [2].

Generally speaking, accurate estimates of O SCS are of vital interest in the characterization of a large number of metal oxide thin film systems and this approach can be used to study other metals and their associated oxides. TiO_2 alone, has been shown to be extremely useful in many contexts: TiO_2 nanoparticles have been used as photo-catalysis [3], 2D TiO_2 nanostructures for chemical sensing [4], TiO_2 bio-compatibility for medical and dental implants [5], etc. Metal oxides are also used in metal-oxide-semiconductor field-effect transistors (MOSFET) [6]. If ion beam analysis is to be successfully study these metal oxide systems, accurate estimates of energy loss are necessary. Especially, as mentioned Chapter 1, there are very few experimental data sets for many common compounds especially around stopping power maxima. It would be of interest to utilize similar relationships to Equation 6.1 and determine the set of metal oxides who's SCS can be fit with the same O SCS values. The objective of such studies is to find differences in the O SCSs for different metal oxides and attempt to explain such differences in terms of changes in electron density.

The approach used in this thesis are sufficiently general and can be applied to other compounds, not just metals and their oxides, but also nitrides, and other binary compounds. TiN contains N, which would be a gas when experimentally determining elemental SCS, and so its use in Bragg's rule calculation might lead to deviations at stopping power maximum as well. To determine if this is the case, the procedure explained in Chapter 3 could be applied to determine the SCS of TiN films. The SCS of N in a condensed phase could be derived by again inverting the Bragg's rule calculation and taking the difference between the SCS of TiN and elemental Ti, which we have already been shown to be accurate. Figure 6.1 shows the SCS of TiN for the medium energy range and contrast the single set of available data to SRIM-13 predictions.

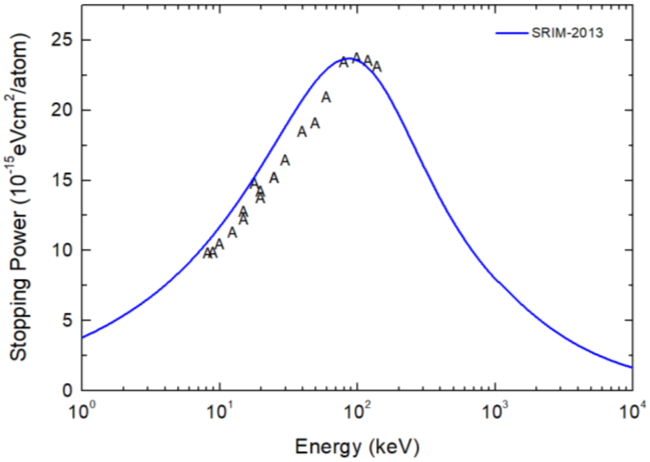

Figure 6.1: The SCS of protons in thin films of TiN. The available literature compared to SRIM predictions, A [7].

There is strong evidence to suggest that any future measurements of SCS using MEIS should be accompanied by electronic density of states calculations (DOS). Recently Roth et al. investigated how SCS of protons in metal oxides (ZnO, VO_2, HfO_2, and Ta_2O_5) where influenced by electronic features such as the band gap, E_g, or valance electron density, in the low-velocity energy range (500 eV – 10 keV) measured using time-of-flight low energy ion scattering (TOF-LEIS) [8]. Notably, the SCS were found to be independent of E_g, and the authors found a dependence on the atomic fraction of O. By calculating the SCS per O atom, the energy loss of the oxides all showed the same energy dependence. It would be useful to perform a similar study with protons in such metal oxide systems, in the medium energy range, and determine if a similar dependence on the O 2*p* states is observed and at which energies it breaks down.

Accurate SCS of protons can be utilized by MEIS and NRA to quantitatively depth profile thin anodic Ti oxide films. Chapter 1 of this thesis introduced the concept of anodization and describes two competing theories that purport to describe the kinetics of anodic oxide growth, on a molecular level: the PDM and the HFM. An isotopic labeling procedure was introduced that would result in the two competing theories making unique oxygen depth profile predictions, that would result from anodization.

In Chapter 4 the experimental *ex situ* MEIS and NRP depth profiling of the ultra-thin anodic oxide films is presented. We found that the anodization of Ti resulted in a bi-layer structure with two distinct oxide regions; $Ti^{16}O_2/Ti^{18}O_2/Ti/Si(001)$. The outermost region, consisting of $Ti^{16}O_2$, is always adjacent to the oxide surface. While the $Ti^{18}O_2$ region grows directly into the Ti metal and contains all of the ^{18}O which composed the original passive oxide. The interpretation of these results requires the PDM as an explanation of the mechanism for oxide growth. The PDM makes the prediction of a bi-layer structure as a result of the continuous creation of anion vacancies at the oxide/metal interface and their transported to and consumption at the solution/oxide interface. With the analogous process in the opposite direction for cationic species, where Ti cations are ejected into electrolyte to form a precipitated oxide layer. From this perspective, the $Ti^{16}O_2$ forms from Ti precipitation in the electrolyte, which contains only ^{16}O anions during anodization. The $Ti^{18}O_2$ region always represents the corrosion front and forms at the oxide/metal interface, as ^{18}O anions react with Ti in the metal substrate, creating anion vacancies in the O oxide sublattice. Such vacancies are filled by ^{18}O atoms directly adjacent and the vacancy is transported towards the oxide/electrolyte interface where it will consumed by a ^{16}O anion from the solution.

Even recent reviews of the current understanding of Ti anodization [9] have suggested that there is no general agreement as to whether the PDM or HFM should be the preferred description of the anodization process. However, our direct quantification of the electrode composition, using NRA and MEIS, is unequivocal. The $Ti^{16}O_2/Ti^{18}O_2/Ti/Si(001)$ structure is not consistent with the predictions of the HFM for reasons discussed in that chapter. There have been few studies that depth profile electrodes and specifically relate them back to the predictions of the PDM vs HFM. However, in the one pre-existing study (using neutron reflectometry) to do so, found the PDM to be the preferred explanation for *in situ* Ti anodization [10].

Fundamental descriptions of anodization can be extended to other important elements such as Al, Ta, Ti, Nb, Zr, Hf and W. Other metals such as V, Mn, Fe, Ni, Co, Bi or Sb can be anodized under more specific conditions. Thus, the same isotopic labeling and high resolution depth profiling procedure can be readily preformed on these systems. The results of which would provide more evidence to support either the predictions of the PDM or the HFM.

The *ex situ* high-resolution depth profiling of anodic Ti oxide described in this thesis, proved to be useful in providing insight into the transport of Ti and O species through Ti electrodes during anodization. However, these IBA techniques require a UHV and the anodes that are transferred from ambient conditions to UHV, may result in drastic compositional changes [11]. For example, the outer-layer can dehydrate and causing hydroxides to become oxyhydroxides and oxyhydroxides to become oxides. It is necessary to create *in situ* techniques to avoid irrevocably changing the outer-layer composition

In Chapter 5, the design and construction of an electrochemical cell for *in situ* RBS was discussed. The working electrode is 60 nm of Ti sputtered onto a100 nm SiN window. Upon biasing the Ti with respect to the Ag/AgCl RE at +2 V in a 0.3 mol/L NaCl solution, the characteristic features of anodization (oxidation) are observed in a series of RBS spectra taken over time. From the *in situ* RBS results alone, the volume expansion associated with Ti oxidation made it difficult to determine if growth is happening at the metal/oxide interface alone or both the metal/oxide and oxide/electrolyte interfaces simultaneously. However from the *ex situ* IBA results in Chapter 4, we concluded that the PDM was the preferred description for Ti anodization and the time evolution of the Ti and O depth profiles appears consistent with the PDM, while Cl incorporation most likely happens during the formation of oxide multilayers that result from precipitation at the oxide/electrolyte interface. Compositional differences between *in situ* and *ex situ* measurements were emphasized. The Cl concentration in the films observed by *in situ* measurements are much higher than that seen in *ex situ* RBS measurements following anodization, implying Cl loss when transferred from ambient conditions to UHV.

The *in situ* RBS as described here was useful for insight into the general mass transport though electrodes during anodization. However, the electrochemical cell could be utilized without modification or with minimal modifications, to study a broad range of electrochemical phenomena: oxidation, electrode dissolution, electrodeposition, etc. In the domain of electrochemistry much of the pre-existing literature focuses on electrical measurements (current, capacitance, etc.) and then makes inferences about electrode structure. Rarely is this accompanied by direct measurements of electrode structure and its time evolution. This is especially true if one wants to evaluate these quantitates without exposure of electrodes to UHV which complicates the interpretations of many existing studies that have relied on AES, SIMS, XPS, and even IBA.

We have discussed with some members of Professor A. Sun's group, in the department of Mechanical and Materials Engineering, at Western University, about a possible system of interest, which utilizes the cell as it is currently designed, is shown in Figure 6.2 that will be used to study the formation of interfaces in Li battery materials. The system uses the same 100 nm SiN windows described in Chapter 5, upon which 60 nm of Cu is deposited to prevent Li from reacting with the window, followed by 500 nm of Li that acts as a working electrode. Next there is a liquid electrolyte, containing P, F, C, and Li and a counter electrode composed of Li, P, F, C, and O. By proceeding through cycles of charging and discharging of the battery, it is hoped that with the cell, the structures and Li tendrils that form at the interface can be observed that are responsible for creating short circuits and sometimes making such batteries unsafe.

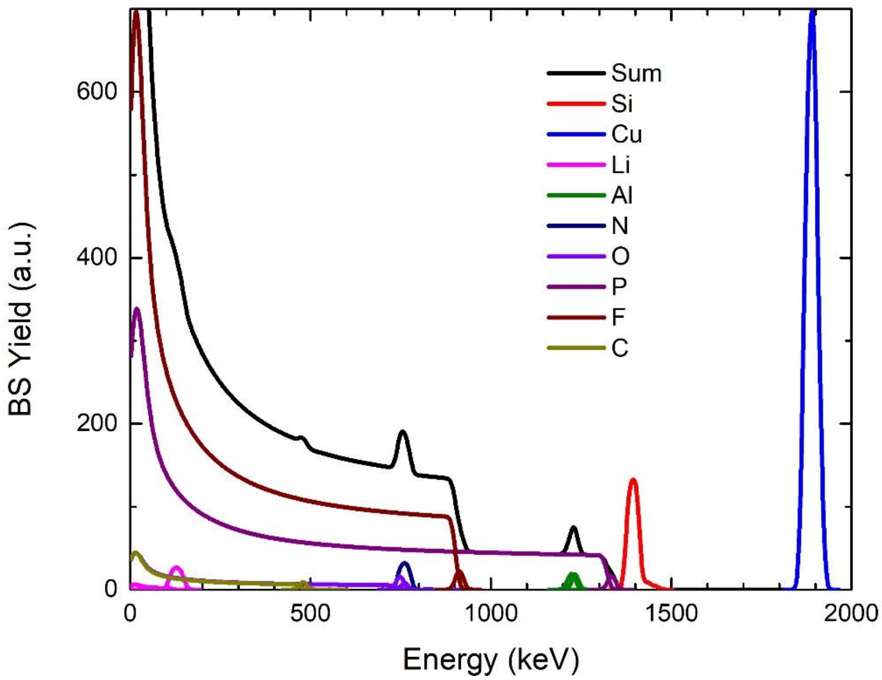

Figure 6.2: Simulation of RBS spectrum SiN/Cu/Li/Al_2O_3/electrolyte multilayer structure related to Li ion battery cathode using 2.5 MeV He ions.

However, the modest depth resolution of RBS (~10 nm) is an inherent limitation to the technique, which means the insight into individual monolayers at the electrode's surface, the absorbed species into these monolayers, and the composition of the Stern layer is not currently accessible. MEIS has a superior depth resolution (~0.5 nm) and an electrochemical cell designed for the purposes of *in situ* MEIS would ultimately be more successful in elucidating electrode/electrolyte interfaces and their evolution.

Recalling the kinematic factors described in Chapter 2, the usual way to get more separation between elements in RBS is to increase the incident ion energy. However, MEIS requires specific energies (50-200 keV), at which the stopping cross sections of protons are maximized. This means, for *in situ* MEIS it is especially crucial to minimize the window thickness and deposited metal thickness that the incident ions will have to travel through before reaching the electrode/electrolyte interface. Increasingly the thickness of these layers leads to energy straggling, which in turn degrades depth resolution. The effect of straggling can be seen in the difference between FWHM of the peak associated with the Ti metal in simulations of the SiN thickness.Using 200 keV H^+ the difference between the peak width between 25 nm thick windows and a 100 nm thick windows, is ΔE ~1.6 keV. According to SRIM the energy loss for H^+ at 200 keV is 14.1 eV/Å which means that 1.6 keV translates to an uncertainty of 11.3 nm. Ultimately, the high energy resolution of MEIS will be lost for thickens of SiN above 25 nm.

To overcome these limitations, for future *in situ* MEIS and RBS studies, it may be possible to use a single Si crystal rather than a SiN. The advantage of this would be realized if the incident beam is channeled to align with a major crystallographic direction of Si. This is shown in the context of MEIS in Figure 6.3 which results in a significant reduction in intensity associated with the Si window. One of the experimental challenges reported in Chapter 5 was the fact that RBS signal associated with Cl at the oxide surface overlapped with that of Si from the SiN window, while O peak overlaps with N in SiN window. We can overcome these challenges using single crystal Si windows.

6.1 References

1. S.N. Dedyulin, *Accurate 50-200 keV proton stopping cross sections in solids*. 2013, The University of Western Ontario.
2. C. Montanari. *Sopping Power of Matter for Ions*. 2018; Available from: https://www-nds.iaea.org/stopping/stopping_hydr.html.
3. B. Bajorowicz, et al., *Application of metal oxide-based photocatalysis*, in *Metal Oxide-Based Photocatalysis*. 2018, Elsevier.

4. E. Comini, *One- and two-dimensional metal oxide nanostructures for chemical sensing*, in *Semiconductor Gas Sensors*, R. Jaaniso and O.K. Tan, Editors. 2013, Woodhead Publishing. p. 299.

5. J.E. Cañas-Carrell, et al., *Metal oxide nanomaterials: health and environmental effects*, in *Health and Environmental Safety of Nanomaterials*, J. Njuguna, K. Pielichowski, and H. Zhu, Editors. 2014, Woodhead Publishing. p. 200.

6. R. M. Warner and B.L. Grung, *MOSFET Theory and Design*. 1999: Oxford University Press.

7. M.A. Sortica, et al., *Electronic energy-loss mechanisms for H, He, and Ne in TiN.* Physical Review A, 2017. **96**(3): p. 02703.

8. D. Roth, et al., *Electronic Stopping of Slow Protons in Oxides: Scaling Properties.* Physical Review Letters, 2017. **119**: p. 163401.

9. J.F. Vanhumbeeck and J. Proost, *Current understanding of Ti anodization: functional, morphological, chemical and mechainical aspects.* Corrosion Reciews, 2009. **27**: p. 204.

10. Z. Tun, J. J. Noël, and D.W. Shoesmith, *Electrochemical Modification of the Passive Oxide Layer on a Ti Film Observed by In Situ Neutron Reflectometry.* Journal of The Electrochemical Society, 1999. **146**: p. 130.

11. D.D. MacDonald, *The history of the Point Defect Model for the passive state: A breif review of film growth aspects.* Electrochimica Acta, 2011. **56**: p. 1761.

Appendix A1: Supplemental material for the growth models of anodization

This appendix contains further mathematical elaboration of the two models of anodization. The HFM's exponentially dependent current density (A1.10) is derived and equations for the potential drop through the oxide film's interfaces (Equations A1.11 & A1.12) and the steady state film thicknesses (A1.15) are given in the context of the PDM.

A1.1 The HFM

The derivation of the HFM presented here follows closely to Logrengel's approach in his review of the HFM [1], who presents a synthesis of Günthershultze and Betz, Verwey, and Cabrera and Mott. Logrengel gives an account of oxide growth in an oxygen rich electrolyte based on the movements of ions via a thermally activated, field-supported, hopping mechanism. The explanation is based on consideration of two consecutive planes of atoms lying on the x-axis that are normal to the metal/oxide interface, located at x and $x+a$. Although our material might not necessarily be crystalline, according to Vanhumbeek and Proost, the "conclusions remain valid in the case of amorphous films as well" [2]. The atomic planes at x and $x+a$ contain an areal density of n_x and n_{x+a} of charge carriers respectively. In figure A1.1, the position of two plans is shown alongside the height of the activation barrier.

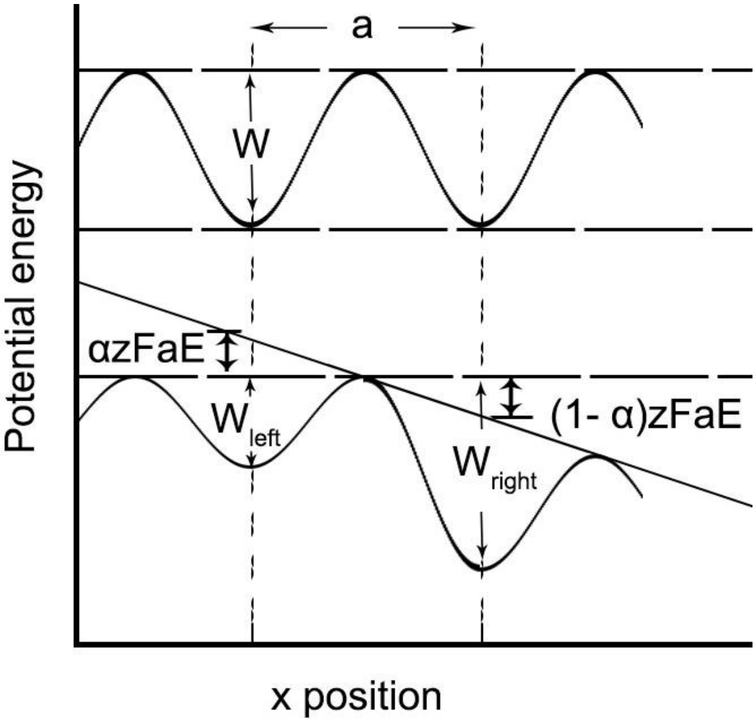

Figure A1.1: A schematic of the potential energy barrier that underlies the HFM. The potential energy, *W*, that must be overcome in the first instance before the application of the electric field. After the electric field is applied, the activation barrier is asymmetric between W_{left} and W_{right}. Thus, the flux of charge carriers in the direction of the electric field will be far greater than in the other direction. Adapted from [2]

Before electric field is applied, the probability for one mole of charge carriers jumping from *x* to *x+a* is:

$$p = ve^{\frac{-W}{RT}} \tag{A1.1}$$

where *v* is the “attempt frequency”. When an electric field is not applied, the activation barrier is symmetric and the rate (molar flux) at which charge carriers move between *x* and *x+a* is:

$$\frac{dn}{dt} = n_x ve^{-W/RT} - n_{x+1} ve^{-W/RT} \tag{A1.2}$$

If an electric field is applied, the activation barrier is lower for the jump in the direction of the field and simultaneously decreased in the opposite direction and this asymmetry is depicted in Figure A1.1. The rate at which charge carriers now move in the presence of the electric field between *x* and $x{+}a$ is:

$$\frac{dn}{dt} = n_x v e^{-(W-\alpha azFE)/RT} - n_{x+1} v e^{-(W+\alpha azFE)/RT} \tag{A1.3}$$

where α describes the symmetry of the activation barrier.

Assuming a linear concentration gradient,

$$c_{x+a} = c_x + a\frac{dc}{dx} \tag{A1.4}$$

we can express the Equation A1.3 in terms of concertation:

$$\frac{dn}{dt} = ave^{\left(-\frac{W}{RT}\right)}\left[c_x e^{\alpha azFE/RT} - (c_x + a\frac{dc}{dx})e^{-(1-\alpha)azFE/RT}\right] \tag{A1.5}$$

Assuming the strength of the electric field renders diffusion negligible in comparison to migration, so $dc/dx \approx 0$. A second assumption is that migration in the direction opposite to the field is negligible given the differences between activation barriers in each direction. Equation A1.5 becomes:

$$\frac{dn}{dt} = avc_x e^{(-W/RT)} e^{\alpha azFE/RT} \tag{A1.6}$$

The current density can be related to the flux of charge carriers:

$$i = zF\frac{dn}{dt} \tag{A1.7}$$

Defining two additional terms:

$$i_0 = zFavc_x e^{(-W/RT)} \tag{A1.8}$$

$$\beta = \frac{\alpha azF}{RT} \tag{A1.9}$$

Results in the current density being written as:

$$i = i_0 e^{\beta E} \tag{A1.10}$$

A1.2 The PDM

A1.2.1 Potential drop at interfaces

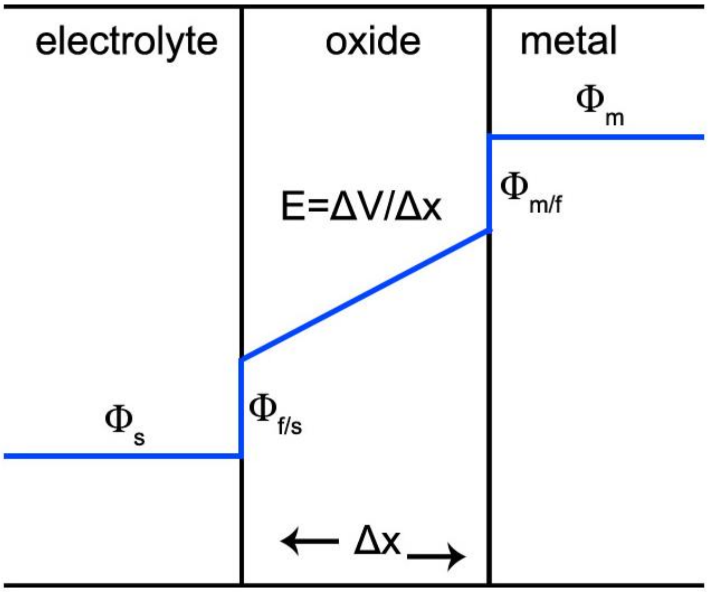

Figure A1.2: A schematic showing the drop in potential across the metal/oxide, $\Phi_{m/f}$, and oxide/electrolyte, $\Phi_{f/s}$, interfaces. The electric field through the film is constant with respect to the spatial dimension *x*.

The drop in potential difference across the barrier layer/electrolyte interface, as depicted in Figure A1.2, is a linear function of pH and applied voltage:

$$\Phi_{\frac{f}{s}} = \alpha V + \beta pH + \Phi_{\frac{f}{s}}^{0} \tag{A1.11}$$

where V is the applied voltage, β is the pH dependence on the potential drop, α is the polarizability of the interface, and $\Phi_{f/s}^{0}$ is the value of $\Phi_{f/s}$ when $V = 0$ and $pH = 0$.

Similarly, the potential drop across the metal/barrier layer interface is given as:

$$\Phi_{\frac{m}{f}} = (1-\alpha)V + \beta pH - EL - \Phi_{\frac{f}{s}}^{0} \tag{A1.12}$$

where E is the electric field strength in the oxide layer.

A1.2.1 Steady state current & thicknesses

Steady states current densities and barrier thicknesses are achieved when the rate of film formation and rate of film dissolution are equated. According to the PDM passive films are non-equilibrium structures brought about by the competing rate of formation and rate of destruction [3] [4]. If the rate of dissolution dominates, the surface becomes depassivated. The barrier layer is expressed in terms of the difference between the rate of growth and dissolution [5]:

$$\frac{dL}{dt} = \frac{dL_{bl}^{+}}{dt} - \frac{dL_{bl}^{-}}{dt} = \frac{2}{\chi}\Omega k_3 - \Omega k_7\left(\frac{C}{C^0}\right)^n \tag{A1.13}$$

where Ω is the volume per mole of cations, χ is the oxide stoichiometry of the oxide in terms of $MO_{\chi/2}$, C is the concentration of hydrogen ion in the solution, C^0 the concentration of hydrogen ions in the standard state ($C^0 = 1$ M), and k_3 and k_7 are the rate constants of reactions (3) and (7) in the PDM. Setting the rates of film growth equal to the rate of dissolution For steady-state (i.e. $dL/dt=0$), the steady-state film thickness can be given as [6]:

$$L_{SS,bl} = \frac{1}{E}\left[1 - \alpha - \frac{\alpha\alpha_7}{\alpha_3}\left(\frac{\delta}{\chi} - 1\right)\right] V_{bl/s} + \frac{1}{E}\left\{\frac{2.303n}{\alpha_3\chi\gamma} - \beta\left[\frac{\alpha_7}{\alpha_3}\left(\frac{\delta}{\chi} - 1\right) + 1\right]\right\} pH + \frac{1}{\alpha_3\chi K} ln\left(\frac{k_3^0}{k_7^0}\right) \quad \text{(A1.14)}$$

where χ and δ are the oxidations states of the metal cation in the electrolyte and barrier layer respectively and $V_{bl/s} = V\text{-}IR_{ol}$. If no change in the oxidation occurs when cation is ejected from the barrier layer and $\chi = \delta$, the equation becomes:

$$L_{SS} = \frac{1}{E}(1 - \alpha)V + \frac{1}{E}\left\{\frac{2.303n}{\alpha_3\chi\gamma} - \beta\right\} pH + \frac{1}{\alpha_3\chi K} ln\left(\frac{k_3^0}{k_7^0}\right) \quad \text{(A1.15)}$$

where $[1-\alpha]/E$ is known as the anodization constant and has a value of 2-3 nm/V for most metals and alloys [6]. For most systems $0.2 < \alpha < 0.3$ [7], the electric field strength will be confined to 1×10^6 V/cm < E < 5×10^6 V/cm. According to Equation 1.6, a central prediction of the PDM is that the steady-state film thickness varies linearly with voltage and pH [7].

A1.3 References

1. M.M. Lohrengel, *Thin anodic oxide layers on aluminium and other valve metals: high field regime* Materials Science and Engineering 1993. **11**.
2. J.F. Vanhumbeeck and J. Proost, *Current understanding of Ti anodization: functional, morphological, chemical and mechainical aspects.* Corrosion Reciews, 2009. **27**: p. 204.
3. D.D. Macdonald, *Passivity: enabler of our metals based civilisation.* Corrosion Engineering, Science and Technology 2014. **49**: p. 143.
4. D.D. Macdonald, *Passivity: enabler of our metals based civilisation.* Corrosion Engineering, Science and Technology, 2014. **49**.
5. D. D. Macdonald and G.R. Engelhardt, *The Point Defect Model for Bi-Layer Passive Films* ECS Transactions, 2010. **28**: p. 123.
6. D.D. MacDonald, *The history of the Point Defect Model for the passive state: A breif review of film growth aspects.* Electrochimica Acta, 2011. **56**: p. 1761.
7. D.D. Macdonald, *Some Personal Adventures in Passivity—a Review of the Point Defect Model for Film Growth.* Russian Journal of Electrochemistry, 2012. **48**: p. 235.

Appendix A2: Iterative numerical program to calculate stopping cross sections

The following explanation describes how to use a generic numerical approach to find the energy of an ion as it penetrates an arbitrary target, before and after scattering, and follows closely to what is provided in Chu et al. [1]. The target is first divided into slabs of equal width Δx. One can assume a constant ε through an individual sublayer if Δx is very thin, i.e. dE/dx is constant through each sublayer (the surface energy approximation). As shown in Figure A2.1, one can start from the surface of the very first sublayer where the ions have energy equal to the incident beam, E_0. At the surface of the second layer the energy, E_1, is lower due to energy loss through the first layer. The energy is:

$$E_1 = E_0 - \frac{dE}{dx}\left(\frac{\Delta x}{cos\theta_1}\right) = E_0 - \varepsilon(E_0)\left(\frac{N\Delta x}{cos\theta_1}\right) \tag{A2.1}$$

Where $\varepsilon(E_0)$ is the stopping power evaluated at E_0 and $\Delta x/cos\theta_1$ is the path length that the ion will travel. From Equation A2.1, one can then compute the energy at the surface of the third slab, E_2, and then use that to find E_3, and so on, in an iterative process until one computes the energy of the $n+1$ slab:

$$E_{n+1} = E_n - \varepsilon(E_n)\left(\frac{N\Delta x}{cos\theta_1}\right) \tag{A2.2}$$

The energy at the surface of the $n+1$ sublayer is determined by using the energy at the surface of the *nth* sublayer and the stopping cross section at that surface energy $\varepsilon(E_n)$ before the ion has traversed this sublayer, given its dependence on energy.

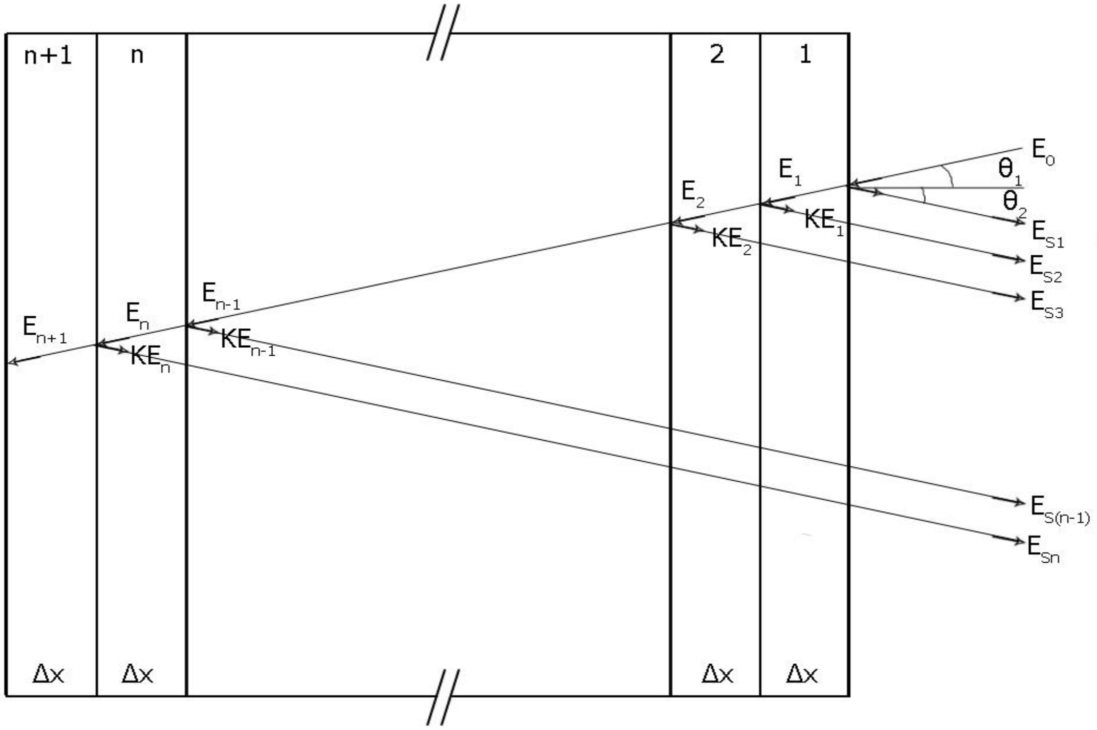

Figure A2.1: Schematic representation for numerical calculations of the energy loss process in IBA. The target is divided into $n+1$ sublayers of equal width Δx. If the ion traverses to the *nth* sublayer, the energy before backscattering is E_n as calculated above and after backscattering is KE_n. The ion must now travel back through the same series of sublayers while losing energy passing through each, before reaching the detector with energy E_{Sn}. Adapted from [1].

Upon scattering, an ion's current energy will be reduced by a factor of K based on Equation 2.1, i.e. the kinematic factor, and the ion will travel on an outgoing path towards the detector. As illustrated in Figure A2.1, the scattered ions will again lose energy along the outgoing path they take proportional to the stopping cross section at their current energy, and the path length $\Delta x/\cos\theta_2$. The finial energies after leaving the target completely, here called E_{S1}, E_{S2},.., E_{Sn}. For E_{S2} :

$$E_{S2} = KE_1 - \varepsilon(KE_1)\left(\frac{N\Delta x}{cos\theta_2}\right) \tag{A2.3}$$

As seen in the above figure, the second ion scattered will have traveled through sublayer 1 and 2 both on an inward and outward path. Thus, E_{S3} will be:

$$E_{S3} = KE_2 - \varepsilon(KE_2)\left(\frac{N\Delta x}{cos\theta_2}\right) - \varepsilon\left(KE_2 - \varepsilon(KE_2)\left(\frac{N\Delta x}{cos\theta_2}\right)\right)\left(\frac{N\Delta x}{cos\theta_2}\right) \tag{A2.4}$$

Which can be iterated to find E_{Sn}, the energy of ions scattered from the nth slab.

Knowing what the energy at each interface is, allows one to calculate the energy loss through each individual slab. From Equation A2.2, on the inward trajectory, the energy loss for the *nth* slap can be calculated:

$$\Delta E_n = E_n - E_{n-1} = \varepsilon(E_{n-1})\left(\frac{N\Delta x}{cos\theta_1}\right) \tag{A2.5}$$

where the stopping cross section used in Equation A2.5 was estimated using Andersen and Ziegler values [2].

The integrated energy loss,ΔE_C^{in}, for the inward trajectory is the sum of all such energy loss for *n* slabs:

$$\Delta E_C^{in} = \sum_{i=1}^{n} \Delta E_i \tag{A2.6}$$

A similar procedure is used to integrate the total energy losses in the outward trajectory after backscattering, to get ΔE_C^{out} based on Equation A2.3.

The ε_{new} in the inward and outward trajectories are given as corrections of the Andersen and Ziegler, ε_{old}, values:

$$\varepsilon^{in}{}_{new}(E^{in}) = \varepsilon_{old}(E^{in})\frac{\Delta E_m}{\Delta E_c{}^{in}} \tag{A2.7}$$

$$\varepsilon^{out}{}_{new}(E^{out}) = \varepsilon_{old}(E^{out})\frac{\Delta E_m}{\Delta E_c{}^{out}} \tag{A2.8}$$

where ΔE_m is the measured energy loss and Chapter 3 describes how it was measured using MEIS spectra and $\Delta E_c$is the calculate energy loss. The processes is iterated until the measured and calculated energy losses are equal within experimental uncertainty.

A2.2 Python Code

```
#program allows you to calculate stopping powers if the files with target compositions and the energy losses are provided
import numpy as np
import os

def Kfactor (M1, M2, angle):
    "function calculates kinematic factor"
    return np.power((M1/(M1 + M2)), 2)*np.power((np.cos(np.radians(angle)) + np.sqrt(np.power((M2/M1), 2) - np.power(np.sin(np.radians(angle)), 2))), 2)

def Stopping_Power_kkk(x, s, a0, a1, a2, a3, b):
    "functional form for KKKNS stoping powers"
    slow = np.power(0.001*x, s)*np.log(np.exp(1) + b*0.001*x)#energy is in the units MeV/amu
    shigh = a0 + a1*np.power(0.001*x, 0.25) + a2*np.power(0.001*x, 0.5) + a3*np.power(0.001*x, (1+s))
    return slow/shigh

def Stopping_Power_az(x, a1, a2, a3, a4, a5):
    "functional form for Andersen and Ziegler stopping powers"
    slow = a1*np.power(x, a2)
    shigh = (a3/x)*np.log(1+a4/x+a5*x)
    return slow*shigh/(slow + shigh)

def StoppingLayer5(Energy, Correction, Layer):
    "function calculates the stopping power at given Energy for the Layer using Corrected Andersen and Ziegler values (REFERENCE) or KKKNS stopping powers (Nucl. Instr. Methods Phys. Res. B 136-138 (1998)159-165)"
    Sum = 0
    for index in range(int(Layer[3])):
        Element = int(Layer[2*index+4] - 1) #to skip fitting option, thickness and number of layers/elements
        Concentration = Layer[2*i+5]
        if Element == 13:#if Si, then use KKKNS stopping powers
            Sum += Correction[Element]*Concentration*Stopping_Power_kkk(Energy, 0.37, 4.16e-002, -1.47e-001, 1.80e-001, 2.79e-001, 15.7)
        else:#for other elements use Andersen and Ziegler
```

```
        Sum += Correction[Element]*Concentration*Stopping_Power_az(Energy, Stop5Coeff[Element][0],Stop5Coeff[Element][1], Stop5Coeff[Element][2], Stop5Coeff[Element][3],Stop5Coeff[Element][4])
    return Sum

Stop5Coeff_str = [line.strip().split() for line in open("Andersen_Ziegler_5_H.dat")]# AZ coefficients a1-a5 from the file
Stop5Coeff = np.array([[float(another) for another in item] for item in Stop5Coeff_str])
PeriodicTable_str = [line.strip().split() for line in open("PeriodicTable.dat")]# atomic weights of elements
PeriodicTable = np.array([float(item[2]) for item in PeriodicTable_str])
os.chdir(os.pardir)
os.chdir("Data")
TargetFile = open(raw_input("Please, enter the name of the target file: "))
Target = []#to store target layers
ToFit = []#to store elements for which one fits the stopping powers
for line in TargetFile:
    item = line.strip().split()
    if item[0] == '0':#layer's stopping power is fixed
        Target.append([float(another) for another in item])
    elif item[0] == '1':#layer's stopping power needs to be fitted
        Target.append([float(another) for another in item])
        LayerOfInterest = Target[-1]# to store the layer for which one fits the stopping powers
        ToFit = [int(item[2*i + 4]) for i in range(int(item[3]))]
    elif item[0] == '-1':#substrate layer
        Substrate = int(item[4]) - 1
EnergyLoss_str = [line.strip().split() for line in open(raw_input("Please, enter the name of energy loss file: "))]
EnergyLoss_exp = np.array([[float(another) for another in item] for item in EnergyLoss_str])#Experimental energy loss
CorrectionCoeff = np.ones((len(EnergyLoss_exp), len(Stop5Coeff)))#all the correction coefficients are initially set to 1
os.chdir(os.pardir)
os.chdir("Output")
OutputFile = open(raw_input("Please, enter the name of the output file: "), 'w')

Energy_calc = []
for i in range(len(EnergyLoss_exp)):#for every energy loss value measured
    Energy_calc.append ([])
    EnergyLoss_calc = 0#calculated energy loss, so that not to call it in while loop before defining the elements Energy_calc
    flag = 0#flag signals if the previous iteration was unsuccessful
    K = Kfactor(PeriodicTable[0], PeriodicTable[Substrate], EnergyLoss_exp[i][3])
    while np.absolute(EnergyLoss_calc - (K*EnergyLoss_exp[i][0] - EnergyLoss_exp[i][4])) > 0.03: #exp - calc
        if flag == 1:#iteration was unsuccessfull - rewrite the calculated values with the next iteration
            Energy_calc.pop()
            Energy_calc.append([])
        Energy_calc[i].append(EnergyLoss_exp[i][0])#first value is equal to the initial energy of the ion
        for j in range(len(Target)):#energy lost on the way in for every layer in the target
```

```
        SublayerThicknessIn = (Target[j][1]/Target[j][2])/(np.cos(np.radians(EnergyLoss_exp[i][1]))*np.cos(np.radians(EnergyLoss_exp[i][2])))
        for k in range(1, int(Target[j][2]+1)):#for every sublayer in the target layer
          Energy_calc[i].append(Energy_calc[i][-1]0.001*StoppingLayer5(Energy_calc[i][-1], CorrectionCoeff[i], Target[j])*SublayerThicknessIn)
    Energy_calc[i].append(K*Energy_calc[i][-1])#energy lost in the backscattering event
    for j in range(len(Target)): #energy lost on the way back
        SublayerThicknessOut = (Target[j][1]/Target[j][2])/(np.cos(np.radians(180EnergyLoss_exp[i][1] - EnergyLoss_exp[i][3]))*np.cos(np.radians(EnergyLoss_exp[i] [2])))
        for k in range(1, int(Target[j][2]+1)):
          Energy_calc[i].append(Energy_calc[i][-1]0.001*StoppingLayer5(Energy_calc[i][-1], CorrectionCoeff[i], Target[j])*SublayerThicknessOut)
    EnergyLoss_calc = K*Energy_calc[i][0] - Energy_calc[i][-1]#calculated energy loss
    for item in ToFit:#changing the correction coefficient for a given element
        CorrectionCoeff[i][item-1] = CorrectionCoeff[i][item1]*(K*EnergyLoss_exp[i][0] - EnergyLoss_exp[i][4])/EnergyLoss_calc
    flag = 1
  else:#storing the E, K*E and the corresponding stoppping powers with correction
    OutputFile.write ("%0.2f %0.2f\n" % (EnergyLoss_exp[i, 0], StoppingLayer5(EnergyLoss_exp[i, 0], CorrectionCoeff[i], LayerOfInterest)))
    OutputFile.write ("%0.2f %0.2f\n" % (K*EnergyLoss_exp[i, 0], StoppingLayer5(K*EnergyLoss_exp[i, 0], CorrectionCoeff[i], LayerOfInterest)))
OutputFile.close()
```

A2.3 References

1. W.K. Chu, J.W. Mayer, and M.A. Nicolet, *Backscattering Spectrometry*. 1978: Academic Press, Inc.
2. H.H. Andersen, J.F.Z., *Hydrogen: Stopping Powers and Ranges in all Elements*. 1977: Pergamon Press, Inc.

Mitchell Brocklebank

Education

Ph.D. Physics –Western University, London, Canada – (2015-present)

- Submitted Thesis: "High Resolution Ion Beam Investigations of the Mechanisms of Titanium Anodization"

M.Sc. Physics – Western University, London, Canada – (2013-transfer to Ph.D.)

B.Sc. Honors Specialization in Physics – University of Western Ontario, London, Canada (2007–2011)

- *Senior Thesis: Ionoluminescence of silicon quantum dots*

Research and academics Interests

- Condensed Matter Physics
- Ion-Beam Analysis (IBA)
- Medium Energy Ion Scattering (MEIS)
- Nuclear Reaction Analysis (NRA)
- Elastic Recoil Detection (ERD)
- Rutherford Backscattering Spectroscopy (RBS)
- X-ray Photoelectron Spectroscopy (XPS)
- Molecular Beam Epitaxy (MBE)
- *In situ* electrochemistry
- Metals anodization

Scholarships and Awards

- Ontario Graduate Scholarship (OGS): May 2017 – April 2018: Provincial, $15,000
- Ontario Graduate Scholarship (OGS): May 2016 – April 2017: Provincial, $15,000
- Teaching Assistant Award for Administration: 2016-2017 Academic year, Physics and Astronomy Dept., Western University.

Journal publications

- **Mitchell Brocklebank**, James J. Noel, Lyudmila V. Goncharova "*In situ* Rutherford backscattering spectrometry for electrochemical studies", to be submitted.
- **Mitchell Brocklebank**, James J. Noel, Lyudmila V. Goncharova "Probing anodic TiO2 growth mechanisms: using medium energy ion scattering and nuclear reaction profiling", to be submitted.
- **Mitchell Brocklebank**, Sergey N. Dedyulin, Lyudmila V. Goncharova "Stopping cross sections of protons in Ti, TiO_2 and Si using medium energy ion scattering", *European Physical Journal D* (EPJD), September 2016, DOI: 10.1140/epjd/e2016-70277-3

Conference articles

- David Barchet, Heidi Potts, **Mitchell Brocklebank**, Zahidur R. Chowdhury, Lyudmila Goncharova and Nazir P. Kherani. "Low-Temperature Ozone-Ambient Grown Native Oxide Passivation of Crystalline Silicon" IEEE PVSC 2015

Conference presentations

- **Brocklebank, M.**, Noel, J.J., Goncharova L.V. (2018), IBA characterization of anodized Ti films: *in situ* and *ex situ*. Poster presentation, *High Resolution Depth Profiling 9*, Uppsala, Sweden, June 25.
- **Brocklebank, M.,** Goncharova L.V., Barchet D. and Kherani N.P. (2017), Silicon nitride interface and photovoltaic device performance: ion beam analysis. Oral presentation, *Canadian Semiconductor Science and Technology Conference,* Waterloo, Ontario, August 24.
- **Brocklebank, M.**, Noel, J.J., Goncharova L.V. (2017) High Resolution Depth Profiling for passive anodized TiO_2 ultra-thin films. Oral presentation, *Canadian Association of Physicists Congress*, Kingston, Ontario, May 29.
- **Brocklebank M.*** , Noël J.J., Goncharova L.V. (2016) Passive TiO_2 growth studies using Medium Energy Ion Scattering and Nuclear Reaction Profiling**.** Oral presentation, *High Resolution Depth Profiling 8*, London, Ontario, August 7.
- **Brocklebank, M.,** Goncharova L.V., Barchet D., and Kherani N.P. (2015) Ion Beam Analysis for Devices Related Stacks. Poster presentation, *Canadian Semiconductor Science and Technology Conference,* Sherbrooke, Quebec, August 16.
- **Brocklebank**, **M.,** Noel, J.J., Goncharova L.V. (2015) High Resolution Depth Profiling for the Study of Titanium Oxidation. Poster presentation, *International Conference on Ion Beam Analysis*, Opatija, Croatia, June 14.
- Dedyulin, S.N., **Brocklebank**, **M.,** Goncharova L.V. (2015). Stopping Cross Sections of Protons in Ti, TiO_2, and Si Using Medium Energy Ion Scattering. Poster presentation, *International Conference on Ion Beam Analysis*, Opatija, Croatia, June 14.
- **Brocklebank**, **M.,** Noel, J.J., Goncharova L.V. (2014) High Resolution Depth Profiling for Titanium Oxidation Studies. *Nano Ontario Conference*, Windsor, Canada, Nov. 6.
- **Brocklebank, M.**, Noel, J.J., Goncharova L.V. (2014) High Resolution Depth Profiling of Ti Oxidation. Oral presentation at *Canadian Association of Physicists Congress*, Sudbury, Canada, June 16.
- **Brocklebank, M.**, Noel, J.J., Goncharova L.V. (2014) High-Resolution Depth Profiling for Titanium Oxidation Studies. Poster presented at *Center for Advanced Materials & Biomaterials Research Day,* London, Canada Nov. 1.
- **Brocklebank, M.**, Noel, J.J., Goncharova L.V. (2014) High-Resolution Depth Profiling for Titanium Oxidation Studies Poster presented at *Sustainability and the Environment Research Showcase*, London, Canada, March 6.
- **Brockleabank, M.** (2011) Ionoluminescence of Silicon Quantum Dots. Presented at *Undergraduate Physics Thesis Presentations,* London, Canada, April.

Professional and academic experience

Teaching experience

Math and Physics Tutor - Freelance - May 2013 - present

- Undergrad and high school physics and math

*Teaching Assistant – Dept. of Physics and Astronomy, Western University – S*ept. 2013 - April 2018

- Course TA: optics, materials science, modern physics, etc.
- Tutorial instructor: 2nd year modern-physics, 1st year physics
- Lab Instructor: 2nd year lab, 2st year lab

Head Teaching Assistant –Dept. of Physics and Astronomy, Western University– January 2016 – May 2017

- Head TA: Organize the efforts of other course TAs
- Tutorials: allocate students and TAs to tutorial sections
- Exams: allocated students and TAs to exam rooms, prepare and print exams, etc.
- Marking: Organizing exam marking sessions, scantrons, etc

Guest lecturer – Dept. of Physics and Astronomy, Western University - March 2017

- Invited give lectures for absent professor for weeks, for two 1st year, undergraduate physics classes
- Electromagnetic induction
- Inductor circuits
- Oscillatory motion

Research experience

Graduate student internship - Applied Materials Inc, Gloucester MA USA - May 2016 – August 2016

- Varian Semiconductor Equipment/Applied Materials Inc: Research and development
- Characterise silicon wafers after plasma immersion ion implantation
- Develop ellipsometric models
- Analyse backscattering data

Service experience

Student government: departmental councillor- Dept. of Physics and Astronomy, Western University - May 2015 – September 2018

- The Physics and Astronomy Graduate Council at University of Western Ontario
- Arrange events for the graduate students, both social and career developmental
- Main source for graduate student advocacy in the department

Liard Lecture organizing committee member– Dept. of Physics and Astronomy, Western University - March 2017 – April 2018

- Selection of and liaison with invited speakers
- Venue sourcing and booking

Councillor in graduate student government- University of Western Ontario - August 2015 – April 2018

- Society of Graduate Students (SOGS) at University of Western Ontario
- Councillors meet together with an executive board to determine policy on a regular basis

Established and organized "Phyzza", a departmental journal club "- Dept. of Physics and Astronomy, Western University - March 2016 – May 2017

- Organise speakers for weekly journal club for grad-students, researchers and faculty
- Present diverse topics about physics, i.e. journals, articles, etc.

Member of Physics and Astronomy Student Association – University of Western Ontario - 2007-2011